ELECTRON BEAM IMAGING AND SPECTROSCOPY OF PLASMONIC NANOANTENNA RESONANCES

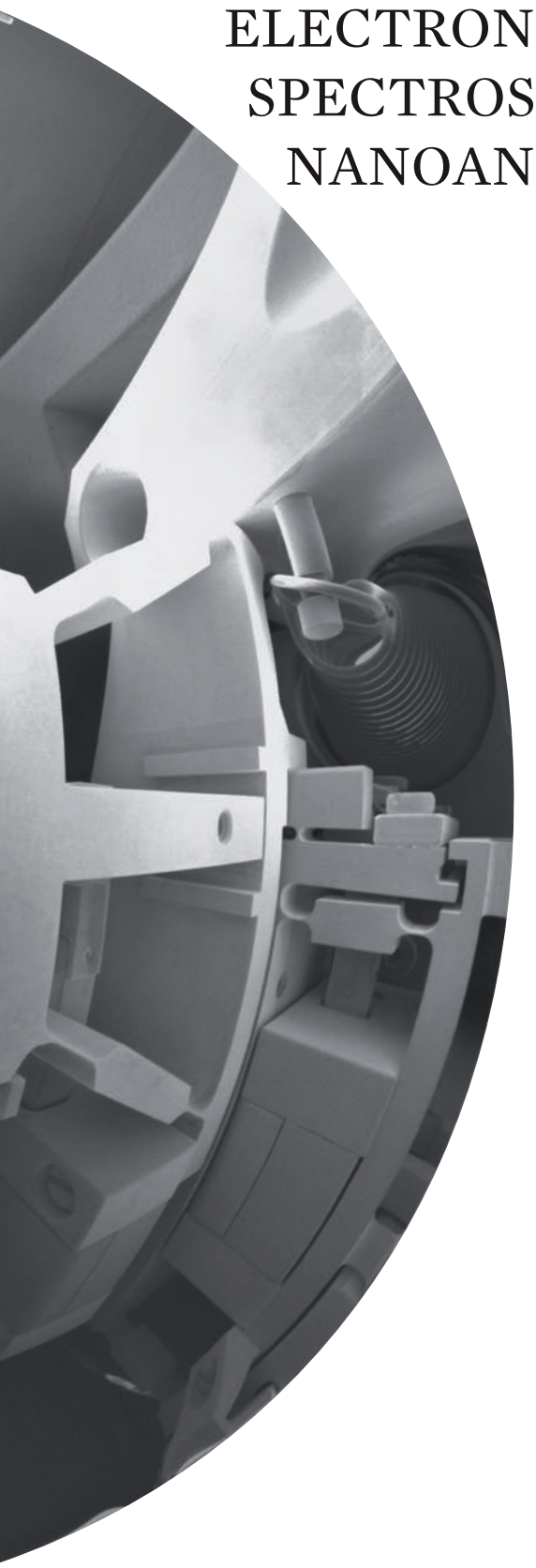

Ernst Jan R. Vesseur

ELECTRON BEAM IMAGING AND SPECTROSCOPY OF PLASMONIC NANOANTENNA RESONANCES

Cover image: self-portrait of the electron microscope. The parabolic mirror used for light collection and the mirror manipulation stage are clearly visible. The image was obtained using the microscope itself, by making an image of a charged glass surface at which the electron beam (coming from the small round hole in the mirror) reflects.

Ph.D. Thesis Utrecht University, July 2011
Electron beam imaging and spectroscopy of plasmonic nanoantenna resonances
Ernst Jan Ruben Vesseur

ISBN 978-90-77209-51-6

A digital version of this thesis can be downloaded from http://www.amolf.nl.

ELECTRON BEAM IMAGING AND SPECTROSCOPY OF PLASMONIC NANOANTENNA RESONANCES

Beeldvorming en spectroscopie van plasmonische nanoantenneresonanties met een elektronenbundel

(met een samenvatting in het Nederlands)

Proefschrift

ter verkrijging van de graad van doctor aan de Universiteit Utrecht
op gezag van de rector magnificus, prof. dr. G. J. van der Zwaan,
ingevolge het besluit van het college voor promoties
in het openbaar te verdedigen
op woensdag 6 juli 2011 des middags te 2.30 uur

door

Ernst Jan Ruben Vesseur

geboren op 11 december 1981 te Rotterdam

Promotor: Prof. dr. A. Polman

This work is part of the research program Microscopy and modification of nanostructures with focused electron and ion beams (MMN) of the Stichting voor Fundamenteel Onderzoek der Materie (FOM), which is financially supported by the Nederlandse organisatie voor Wetenschappelijk Onderzoek (NWO). The MMN program is co-financed by FEI Company.

Contents

1 Introduction **9**
- 1.1 Light at the nanoscale 9
- 1.2 Fabrication at the nanoscale 12
- 1.3 Imaging and spectroscopy at the nanoscale 14
- 1.4 Contents of this thesis 20

2 Observation of plasmon modes in Au nanowires using CL spectroscopy **23**
- 2.1 Introduction 23
- 2.2 Methods 25
- 2.3 Results 25
- 2.4 Conclusions 28

3 Plasmon resonances in a FIB-fabricated single-crystal Au ridge **29**
- 3.1 Introduction 29
- 3.2 Methods 30
- 3.3 Results 31
- 3.4 Conclusions 34

4 Modal decomposition of surface plasmon whispering gallery resonators **35**
- 4.1 Introduction 35
- 4.2 Methods 36
- 4.3 Results 37
- 4.4 Conclusions 42

5 Broadband Purcell enhancement in plasmonic ring cavities **45**
- 5.1 Introduction 46
- 5.2 Methods 47
- 5.3 Results 48
- 5.4 Conclusions 56

6 Plasmonic whispering gallery cavities as optical nanoantennas **57**
6.1 Introduction 57
6.2 Mode selectivity and Fano line shapes in far-field optical excitation 59
6.3 Spectral reshaping of fluorescence by coupling to antenna resonances 62
6.4 Spatially resolved excitation and angle-resolved emission 66
6.5 Photoelectron emission due to antenna resonances 72
6.6 Conclusions 74

7 A metal-insulator-metal waveguide at cutoff as effective $n = 0$ material **75**
7.1 Introduction 76
7.2 Results 77
7.3 Conclusions 83
7.4 Methods 83

8 Applications **85**
8.1 Introduction 85
8.2 A localized surface plasmon sensor 86
8.3 A surface plasmon laser 88
8.4 Light detection as a monitor for focused-ion-beam milling 89
8.5 Template stripping off focused-ion-beam-structured Si templates 92
8.6 Single-photon source 93

References **97**

Summary **109**

Samenvatting **113**

List of publications **117**

Dankwoord **119**

About the author **121**

1

Introduction

1.1 Light at the nanoscale

Light is ubiquitous and plays a very important role in our daily lives. The light we receive from the sun or light that we produce using artificial sources is invaluable for the perception of our surroundings. Light refracts as it enters the lens in our eye, forming an image on the retina. Using lenses and mirrors in microscopes, telescopes and other optical equipment, humans have managed to improve the control of light. The manipulation of light by a medium is governed by the refractive index. For this reason, in order to further increase the control of light, it is important to control the refractive index, or more precisely, the dispersion, which is the relation between the temporal and spatial frequency of light. Conventional optical materials have a refractive index that is roughly independent of frequency over the visible wavelengths.

A special form of light, a so-called surface plasmon polariton (SPP) [1], is light that is bound to the surface of a metal. SPPs are fluctuations in the density of the electron plasma with electromagnetic fields that are strongly confined to the metal-dielectric interface. The dispersion relation of SPPs (black curve in Fig. 1.1) shows a nonlinear dependency between the spatial and temporal frequency. For low frequencies, SPPs behave much like ordinary light, showing a linear dispersion. However, for higher frequencies, the dispersion bends, meaning that SPPs have k-vectors that are much larger, or wavelengths that are much shorter, than those of ordinary light.

The strong confinement of SPPs and the strong dispersion concurrent with very short wavelengths give SPPs the potential to control light at very short length scales, much shorter than what is possible with conventional optics [2–4]. By using SPPs

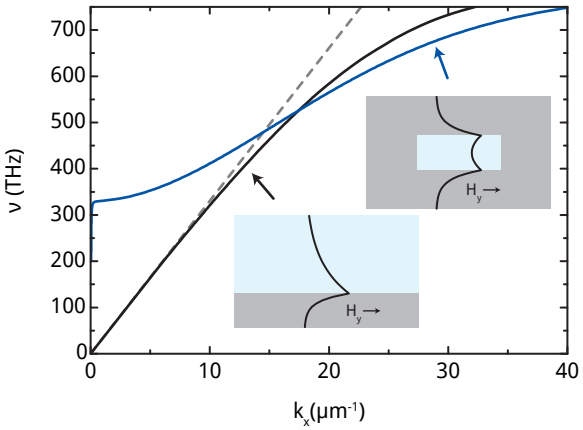

Figure 1.1: Dispersion relation of SPPs for frequencies below the surface plasmon resonance. Dashed line: light line in glass. Black curve: SPP on a Ag-glass interface. Blue curve: TM SPP in a Ag-glass-Ag waveguide with a 200 × 85 nm core.

it becomes possible to confine light to a nanoscale volume, which is important to bridge the gap in length scales between optical fibers (μm scale) and integrated circuits (10s of nm scale) and to enable applications in light sources [5], sensors [6], solar cells [7], and in many other areas.

The concentration of light by SPPs at a metal surface can be further increased when SPPs are laterally confined in a surface plasmon waveguide based on structuring of the metal surface [8, 9]. Waveguides allow us to tune the dispersion of SPPs over a wide range of energies and k-vectors. Recent advances in nanolithography techniques have enabled waveguides based on wedges [10–12], grooves [13–19], stripes [20–22], wires [23–26], dielectric claddings [27, 28], slots [29, 30], coaxial arrangements [31, 32], periodic corrugations [33, 34], particle chains [35, 36] and multilayer stacks [37, 38]. The blue curve in Fig. 1.1 shows the dispersion of such a multilayer geometry consisting of a SiO_2 core surrounded by a Ag cladding. This geometry supports a plasmon mode that is confined to the 200 × 85 nm waveguide, with fields that decay evanescently in the metal cladding. The dispersion relation has several features that set it apart both from light in vacuum and a planar SPP. At high frequencies, the k-vector for the waveguided plasmon is very high, due to the interaction between plasmons on the top and on the bottom metal interfaces. At lower frequencies, the dispersion of the plasmon waveguide levels off, crossing the dispersion of planar SPPs, the light line and even the y-axis. The propagation of visible light in this geometry thus shows behavior corresponding with very small wavelengths up to very long wavelengths all in a single waveguide (discussed in more detail in chapter 7). Exploiting the tunability of the dispersion, other SPP waveguides were found with mode indices ranging from record-high values [38] all

the way to a negative index [39–45] depending on the waveguide geometry. The tunable dispersion can also be exploited for plasmon focusing using a tapered geometry [26, 46–53].

SPPs can be successfully confined to three dimensions in a waveguide of finite length that operates as a plasmon resonator. The termination of the waveguide leads to standing plasmon waves due to reflection at the waveguide ends. Such plasmon resonators were demonstrated based on strips [54, 55], wires [56–58], multilayer stacks [38, 59], voids [60–62], particle arrays [63–65] and other geometries. Resonances in these geometries can be excited by incident light that is captured with an effective cross section that is larger (up to 10×) than the geometrical cross section. In this process, plasmon resonators couple light from the far field to a very small volume. For this reason they are often referred to as optical nanoantennas [66]. Using this coupling, optical nanoantennas can be used to efficiently excite an optical emitter or to enhance nonlinear effects [51, 67–70]. Optical nanoantennas not only operate in receiving but also in transmitting mode, in which antennas transform a near-field excitation into a far field angular emission pattern. The shape of this pattern is determined by the field distribution in the nanostructure and can be tuned to, for example, a high degree of directionality [71–73]. The strong near-field coupling of a nanoantenna resonance to an optical emitter such as a dye or quantum dot can be used to enhance the spontaneous emission rate [46, 74–85]. Exploitation of the strong coupling between light and matter in plasmonic nanoantennas has lead to applications in sensing [86], detectors [87–89], solar cells [90–92], microscopy [93–95] and photothermal cancer treatment[96].

In the exciting field of plasmonics, in which the first applications have now appeared but many more are expected to follow, there are several open questions. Plasmonic devices can often be optically addressed from the far field using a microscope. However, due to the intrinsically small length scales it remains difficult to probe the near field and answer the question: where is the light? And: how well is the plasmon confined? What is its dispersion? To answer these questions, we need characterization techniques at high spatial resolution.

When optimizing devices, more questions arise: how can we further control the confinement? How do we control the dispersion? How does a surface plasmon interact with emitters? Answering these questions relies on a thorough understanding of the behavior of light at the nanoscale. We also require accurate fabrication techniques to make structures with feature sizes much smaller than the wavelength of light.

The next sections describe the techniques used for accurate fabrication as well as the experimental techniques employed to resolve and control the field of surface plasmons in resonant nanoantennas.

1.2 Fabrication at the nanoscale: focused-ion-beam milling

Materials can be structured in one dimension by making thin films with techniques such as thermal evaporation, e-beam assisted evaporation or sputtering. Structuring a thin film in the other two dimensions is possible with techniques such as electron beam lithography or nanoimprint lithography, offering a resolution down to the nanometer range. These techniques use a mask as an intermediate step. The mask allows for selective etching or selective deposition of materials using evaporation and subsequent lift-off. Structures can be fabricated with features down to the 10 nm range. Metals deposited using this technique are always polycrystalline; they possess a crystal-grain-induced roughness with a magnitude and length scale determined by the evaporation technique. As an example, Fig. 1.2(a) shows a scanning electron micrograph image of a 1-µm-long, 100-nm-wide Au nanowire on a Si substrate fabricated using electron beam lithography, thermal evaporation of Au, and liftoff.

Although these masked techniques provide valuable samples in many cases, a technique that allows for processing single-crystal metals with consequently a smaller roughness, operated in a single step is often preferred. Focused-ion-beam milling is such a technique.

Focused-ion-beam (FIB) milling is a maskless, one-step process for sculpting

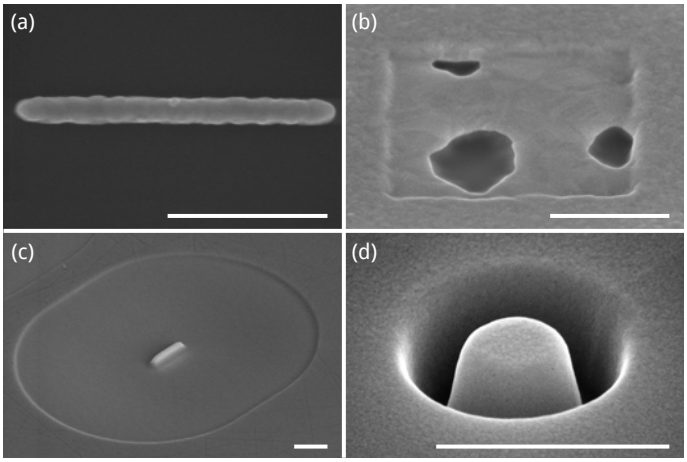

Figure 1.2: SEM images of polycrystalline and monocrystalline Au nanostructures. **(a)** Polycrystalline nanorod fabricated by electron beam lithography, evaporation and lift-off. **(b)** FIB-fabricated square in a 50-nm-thick evaporated Au film on glass, showing roughness and partial removal of the Au layer due to varying crystal orientations. **(c)** FIB-fabricated ridge on a polished single-crystal Au (111) pellet. **(d)** FIB-fabricated ring in a template-stripped Au surface. Scale bars: 500 nm

materials on the nanometer scale. FIB is an ideal tool in scientific research because it allows for rapid fabrication of new prototypes. In a FIB system, a tightly focused 30 keV Ga^+ ion beam is directed to a sample surface. Due to atomic collisions with the incoming ions, atoms are sputtered away from the surface and by scanning the beam a pattern is milled into the substrate. FIB systems typically operate with currents ranging from a few pA to several nA, which give rise to milling rates of 10^{-4} to $1\,\mu m^3\,s^{-1}$ strongly dependent on the material at the sample surface. The milling rate increases for shallower angles between the ion beam and the surface. The milling rate of a particular crystal is also dependent on lattice orientation.

FIB is often used to create cross sections of multilayer structures, a method that is also used in this work. However, the most important application of FIB here is the structuring of metal surfaces. Figure 1.2(b) shows a square area milled in a 50-nm-thick polycrystalline Au film using a 28 pA ion beam current for 5 s. The figure shows that FIB allows for sculpting of the metal surface at a very small length scale. As a result of the lattice-orientation-dependent milling rate, the ion beam mills fully through the layer in some sections, while in other regions it does not, which is an undesired effect. As is also apparent from the figure, the Au surface roughness on the bottom of the square is greater than on the unirradiated surface.

Throughout this thesis, we use single crystal substrates for FIB fabrication of well-controlled, smooth plasmon resonator structures that do not suffer from grain-induced roughness. As an example, Fig. 1.2(c) shows a FIB-fabricated ridge on a single-crystal Au substrate made by milling away the Au around the ridge to a depth of 100 nm. A 10 pA beam current was used. The substrate is a 1-cm-diameter cylindrical Czochralski-grown Au pellet that is polished on the (111) plane to ~1 nm roughness. The figure shows a smooth surface without grain-induced defects. The FIB milling shapes the ridge in a well-controlled fashion only possible on monocrystalline materials.

As a result of Ga^+-irradiation of the surface, the underlying layers can be altered, for example by implantation of ions or a change in the crystal structure. It is known that this leads to undesired optical effects in dielectrics such as quartz [97], Si_3N_4 [98] or silicon [99]. However, there are no reports suggesting that the optical properties of metals are affected by FIB milling. Indeed, theoretical modeling of plasmonic resonators using tabulated materials constants provides an excellent comparison with experiments on FIB-milled metal structures as will be shown in this thesis (chapters 3 and 4).

A focused ion beam also allows for deposition of materials. Precursor gasses flown into the chamber of a FIB system decompose under ion-irradiation, leading to material deposition on the surface at the position of the ion beam. For example, using a Pt-containing precursor, protection layers are routinely deposited before FIB milling exposes the cross section of a multilayer stack.

The spatial resolution of FIB milling depends on the application. Cross sections can be made with high quality (cross section roughness < 5 nm), positioned with nm-accuracy only limited by drift. FIB milling on surfaces typically gives features down to ~30 nm in size. Here, the resolution is strongly dependent on the beam

current. Also, redeposition of sputtered material determines the final structure. Redeposition occurs close to the beam impact position, predominantly on structures in direct line-of-sight of the milled surface. Redeposition can be used to create narrow channels with widths below 20 nm [100] in metal layers. The channels become narrow due to redeposition of material from one sidewall onto the other sidewall. Redeposition can also lead to tapering of ion milled grooves as will be shown in chapter 4.

When FIB fabrication steps are combined with evaporation, sputtering, or other deposition techniques, complex three-dimensional structures become possible. Examples are the plasmon waveguides presented in chapter 7.

A Czochralski-grown single-crystal is expensive; in some cases it is desirable to work with low-cost substrates. Plasmonic structures are small, and therefore the substrate does not need to be monocrystalline over the entire surface. In many cases, crystal domains of 10 µm diameter are sufficient. Template stripping [101–104] is a technique that provides such a surface, with large (30 µm) crystal grains and a roughness within one grain that is small. Freshly cleaved mica sheets are atomically flat over large (mm) distances and are used as substrates for the template stripping procedure. Using thermal evaporation, a 3 µm thick Au layer is grown onto the mica. Subsequently, the sample is annealed at 500° C. This temperature is limited by the delamination of mica layers, which occurs at higher temperatures. Due to the anneal, the crystal domains initially present after evaporation merge and form large single-crystalline domains. While the top surface is relatively rough, the bottom Au layer is atomically flat. Using an epoxy resin, a Si wafer is then glued to the Au surface. Silicon is practical because it is conductive and available as thin, flat wafers, but other materials can potentially also be used. After curing, the Au is bonded to the epoxy with higher affinity than it is attached to the mica substrate, and the Au layer can therefore be stripped off from its template. The stripping reveals a smooth Au surface. This substrate can now be used for FIB milling in the same way as the Czochralski-grown substrate. Figure 1.2(d) shows a FIB-fabricated plasmon resonator fabricated in a template-stripped Au surface, demonstrating the high quality surface that this technique provides.

1.3 Imaging and spectroscopy at the nanoscale: optical excitation by an electron beam

The resolving power of an optical microscope is limited by diffraction, allowing it to distinguish objects separated by not less than about half an optical wavelength. The study of optical properties at higher resolution is possible with techniques such as near-field scanning optical microscopy (NSOM), which provides access to features smaller than the wavelength of light using a scanning tip [105]. NSOM is widely used to detect the flow of light through nanophotonic structures. However, the spatial resolution in practical applications is usually not higher than 100 nm. Furthermore, interaction of the tip with the light in the structure often affects the

experiment in an undesired way [106].

A scanning electron microscope (SEM) using a tightly focused electron beam has a resolution down to the 1 nm range. The use of SEM is widespread for characterization of small structures. A process so far unexplored for characterization of nanophotonic structures is the detection of light in the SEM. This mode of operation, cathodoluminescence imaging spectroscopy, allows us to perform optical experiments on plasmonic structures using the spatial resolution of the electron beam. In this way, the resolution can be enhanced up to 100-fold, compared to optical techniques.

An SEM employs an electron beam with an energy of 1 to 40 keV and a beam current of up to tens of nA. Electrons impinging on the sample surface generate secondary electrons, which are emitted from the surface. The detection of these secondary electrons (SE) as well as backscattered primary electrons forms the operating principle of the microscope, due to their material-dependent emission rate. There is a multitude of other processes that occur when electrons bombard a sample, some of which are associated with optical excitations [107]. The process of light emission as a result of electron beam irradiation is called cathodoluminescence (CL), a term originating from early cathode ray tube experiments. Both coherent and incoherent processes give rise to CL emission. Incoherent emission occurs when electron-hole pairs or other electrical excitations caused by the incoming beam radiatively decay. These excitations potentially give rise to the emission of thousands of photons per electron. This incoherent CL, which is material-specific, was used to generate different colors in the phosphors of cathode ray tube television screens. It is also widely used in mineralogy for the characterization of materials.

Coherent emission of CL occurs through three channels. First, when the electron velocity exceeds the velocity of light in the medium, Cherenkov radiation is produced. This is not a relevant process in an SEM due to the relatively low energies used. Second, the transition of an electron across an interface between materi-

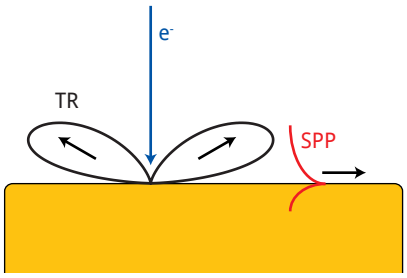

Figure 1.3: Generation of transition radiation and SPPs by an impinging electron beam.

als with different dielectric constants gives rise to so-called transition radiation (TR) [108]. The TR occurs in angular lobes similar to that of a point dipole at the surface. Third, an electron impinging on photonic nanostructures gives rise to the generation of light according to the modes of the structure. When an electron impinges on a metal surface it excites SPPs. SPP waves are bound to the surface, and far-field emission occurs when SPPs are coupled out, for example by surface roughness or by nanostructures that are engineered to provide this coupling.

For 30 keV electrons, the typical excitation probability of TR and SPPs at optical frequencies is 10^{-3} per electron, which is 6 orders of magnitude less than the typical emission probabilities in incoherent processes. Coherent CL is nevertheless very important, because the excitation probability of TR and SPPs is governed by the local density of optical states (LDOS) [109]. A tightly focused electron beam can therefore be used as a probe of photonic properties at a subwavelength scale.

It was realized in the late 1950s that electrons can be used to excite surface plasmon polaritons and that a measurement of the energy loss of electrons incident on a thin metal film provides proof of this excitation [110]. The first observation of CL from metal structures was reported on metal films patterned with a grating, required to provide a means of outcoupling of the SPPs [111, 112].

Advances in electron microscopy enabled the use of an electron beam focused to a small spot (1–10 nm) to study the properties of SPPs at very small length scales. Recent experiments demonstrated a direct measurement of the propagation length of plasmons [113, 114] by scanning an electron beam over a metal surface in the vicinity of a grating. CL was used at even smaller length scale in a study of the plasmon resonance of a silver particle [115]. By scanning a tightly focused beam over the particle, the resonant surface plasmon field was probed, for the first time exploiting the deep subwavelength resolution of electron beam excitation. This work inspired many experiments that use the nanoscale size of the electron beam to resolve localized plasmon resonances in a wide range of resonator structures [12, 19, 58, 116–120].

In imaging CL spectroscopy, the incident electron and its image charge in the substrate form a point dipole that then effectively couples to the modes of the plasmonic structure, probing the local optical density of states. As the electron beam can be accurately placed (using the secondary electron image that is collected in parallel), it provides a unique tool to perform optical experiments at the nanoscale. So far, the potential for this technique in nano-optics has been only exploited to a very limited extent.

In this thesis we investigate cathodoluminescence imaging spectroscopy on plasmonic nanostructures. The setup is based on an FEI XL30 electron microscope and detects the light that is emitted near the impact position of the electron beam. Figure 1.4(a) shows a schematic of the microscope chamber and the detection system. Inside the vacuum chamber of the microscope, the electron beam emerges from the pole piece, the final part of the electron beam column. The electron beam typically has an energy of 30 keV and a current of several nA. The sample under study is positioned below the pole piece at a working distance of 13.5 mm.

This working distance allows for light collection using an 11-mm-high off-axis parabolic mirror positioned between the pole piece and the sample; the electron beam is allowed to pass through the mirror by a 600 µm diameter hole. The mirror is made of 6061 aluminum and is diamond-turned with a ~300 nm precision to a paraboloid with parameter $a = 1/10\,\mathrm{mm}^{-1}$. The angular range covered by the mirror is 1.46π sr. The focus of the paraboloid is at a distance of 0.5 mm from the lower side of the mirror. Light that is generated in the focus is collimated by the mirror into a beam that leaves the SEM vacuum chamber through a quartz window. The beam falls onto a flip mirror (see Fig. 1.4(a)) that allows the collection setup to operate either in spectroscopic mode or angle-resolved mode.

In spectroscopic mode, the CL is focused by an achromat lens onto an optical fiber. The fiber is fed into a 30 cm spectrometer, using the fiber core diameter as the effective slit width. The spectrometer uses a 150 lines/mm grating blazed at 800 nm. In most cases, the moderate spectral resolution offered by a 600 µm core diameter fiber (~12 nm) is sufficient while at the same time the relatively large diameter allows for accurate alignment. The spectrometer is equipped with a liquid-nitrogen-cooled CCD array detector that acquires the emitted cathodoluminescence from the sample with typical exposure times for each pixel ranging from 0.1 to 10 s. The overall detection efficiency of the setup in spectroscopy mode is in the range 5–10%. A software program is used to synchronize a scan of the electron beam with the acquisition of CL spectra on the CCD. Spectral data is corrected for system response using a measured transition radiation spectrum from a Au surface normalized to the theoretical spectrum. In this way a two-dimensional image of absolute CL emission spectra can be made, at a resolution determined by the electron beam spot size (typically 10 nm). Images as large at 1000 × 1000 pixels can be routinely acquired. The collection efficiency of the system developed for this thesis is approximately 50× better that that of commercial CL systems, due to a 4-axis piezoelectric mirror alignment system that allows for precise placement of the mirror focus at

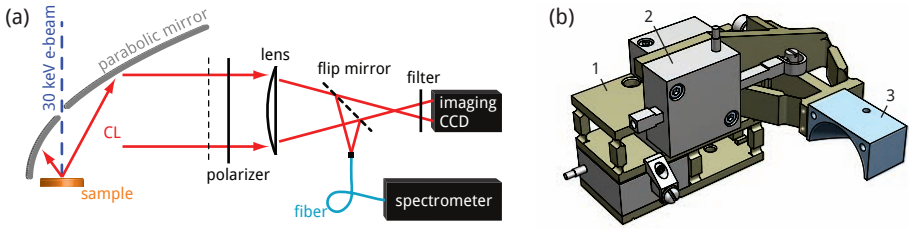

Figure 1.4: (a) Schematic of the cathodoluminescence imaging spectroscopy setup (not to scale). Cathodoluminescence emission from a sample, caused by an impinging 30 keV electron beam, is collected by a parabolic mirror placed above the sample. The light is guided towards a detection system that includes a camera to directly monitor the beam and a spectrometer equipped with a CCD array detector. **(b)** Mirror manipulation stage using a Ti leaf spring system (1), piezo motors (2) and an aluminum mirror (3).

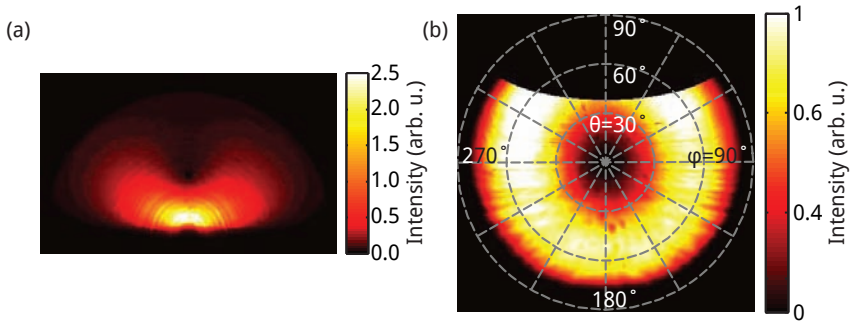

Figure 1.5: Angle-resolved CL emission recorded on a 1024 × 1024 pixel CCD array detector. **(a)** Image showing the light emerging from the parabolic mirror. The emission originates from a 30 keV electron beam incident on an unstructured Au surface, giving rise to transition radiation. **(b)** Angular distribution of the transition radiation, obtained by transformation of the CCD image in (a). Polar (θ) and azimuthal (φ) angles are indicated.

the electron beam position (Fig. 1.4(b)).

A second, and entirely new, feature of the cathodoluminescence imaging system is the angle-resolved mode. By switching the flip mirror in Fig. 1.4(a) the beam emerging from the SEM chamber is now detected on a thermoelectrically-cooled, 1024 × 1024 pixel CCD array detector. A filter is used to select a spectral bandwidth. Figure 1.5(a) shows the transition radiation emitted by an unstructured Au surface irradiated with 30 keV electrons emerging from the parabolic mirror recorded on the CCD through a filter transmitting at 800 ± 20 nm. In this image, every pixel corresponds to a unique emission angle from the sample. Taking into account the ray optics of the parabolic mirror, the image is transformed to a plot of the polar (θ) and azimuthal (φ) emission angles, using the proper Jacobian for this geometry (Fig. 1.5(b)). The figure shows a symmetric angular distribution as is expected for transition radiation and testifies of the good alignment of the system.

The achromat lens used to focus the light into the fiber in spectroscopy mode is also used in angle-resolved mode (see Fig. 1.4(a)). The lens images a plane to the right of the parabolic mirror (indicated by a dashed line) onto the CCD. The lens allows for demagnification of the image and also reduces the sensitivity of the angular detection to imperfections in the mirror.

Efficient detection in spectroscopic mode and accurate angular detection in angle-resolved mode critically depend on the alignment of the mirror, the sample and the electron beam. Figure 1.6 shows the beam profile at 30 cm from the parabolic mirror with a light source that is either aligned with the mirror focus or misaligned by 10 µm perpendicular to the optical axis. The images were obtained using a ray tracing calculation of an isotropic emitter, ignoring diffraction. The figures show that a small misalignment leads to large distortions in the image,

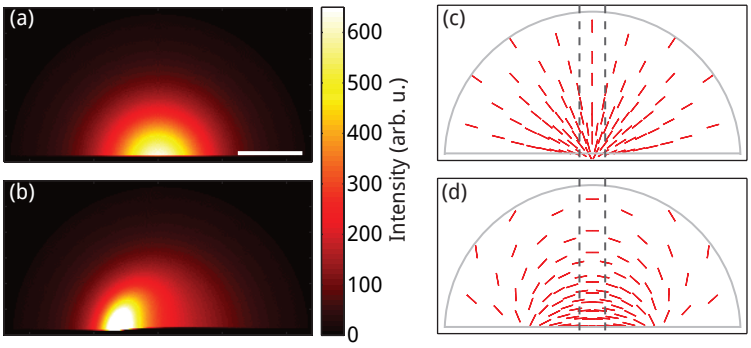

Figure 1.6: The beam leaving the parabolic mirror. **(a)** Calculated beam profile at 50 cm from the mirror for perfect alignment of an isotropic emitter in the focus of the parabolic mirror. **(b)** Situation as in (a), for a light source that is displaced by 10 µm perpendicular to the optical axis. **(c)** Polarization at different positions in the beam for a dipole emitter in the focus of the parabolic mirror aligned with the axis of the paraboloid (dipole perpendicular to the plane of the figure). Dashed lines indicate the area selected by a slit in polarized-spectroscopy mode. **(d)** Same as in **(c)**, for a dipole emitter with horizontal orientation perpendicular to the optical axis (dipole pointing from left to right in the figure). Scale bar: 5 mm

potentially reducing the CL detection efficiency or the accuracy of angle-resolved measurements.

The alignment of the mirror thus has to be within µm precision. For this purpose, the setup is equipped with a stage that controls the mirror position using a Ti leaf spring system and piezo motors (see Fig. 1.4(b)) that allow the mirror to be translated in two orthogonal directions in the horizontal plane and rotated over two orthogonal axes. Alignment in the vertical direction is done by controlling the height of the sample stage of the microscope. During the alignment procedure, a strongly luminescent YAG:Ce phosphor or a Au surface is used to generate cathodoluminescence. The achromat lens is removed and the CCD used for angle-resolved measurements images the beam emanating from the SEM chamber. While monitoring this CCD view, calculated images such as in Fig. 1.6(b) provide an aid in reaching perfect alignment.

In addition to spectrally and angularly resolving the CL emission, the setup also allows for detection of the polarization of the emitted light. To do so, rotation of the polarization by the parabolic mirror has to be taken into account. Reflection of CL at the mirror surface occurs under different angles depending on the emission direction. As a result, the polarization after reflection by the mirror does not have a one-to-one relationship with the polarization before reflection. We illustrate this by considering the emission from a dipole source that is aligned with the axis of the paraboloid. When observed from the top, the light emitted from this dipole has a polarization that is independent of the emission direction. However, as Fig. 1.6(c) shows, after reflection by the parabolic mirror the polarization strongly depends

on the position in the beam. Figure 1.6(d) plots the polarization direction in the reflected beam for a horizontal dipole emitter perpendicular to the optical axis, showing a similar effect.

In angle-resolved mode, the polarization state in the beam can be determined for every pixel in the image by positioning a polarizing plate in the setup (see Fig. 1.4(a)) and by collecting several images for different polarizer orientations. However, in spectroscopy mode, all light is focused into one fiber and the signals from different emission directions are mixed. Therefore, using only the polarizer does not select one polarization. This problem can be solved by using a slit in conjunction with the polarizer. The slit selects the central part of the beam, indicated by the dashed lines in Fig. 1.6(c) and (d). For this part of the beam, the effect of the parabolic mirror is identical, independent of emission angle. The polarizer can now be turned to a desired orientation and a single polarization is selected. This method allows for polarized detection of CL in spectroscopy mode.

1.4 Contents of this thesis

In this thesis, each of the chapters 2–7 presents an advance in the understanding of resonant modes in plasmonic nanoantennas, enabled by advances in the focused-ion-beam technique and the angle- and polarization-resolved cathodoluminescence imaging spectroscopy technique developed in this thesis.

Chapter 2 contains the first report of standing plasmon waves on Au nanorods observed by CL imaging spectroscopy. It is shown that polycrystalline nanorods behave as waveguides for plasmons, confining them to the nanowire through reflection at the end facets. As a result of crystal grain-induced irregularities, the CL emission also shows features that are not related to standing waves.

In **chapter 3**, fabrication using FIB milling on a single-crystal Au surface yields a plasmon cavity without irregularities. The CL emission can be fully explained by a superposition of 5 resonances, each with a distinct spatial and spectral profile. Calculations using the boundary element method confirm that a propagating plasmon mode is bound to the top of the ridge.

Accurate milling using FIB in a single-crystal substrate is further exploited in **chapter 4** in order to fabricate plasmonic whispering gallery cavities with tunable plasmon resonances. An excellent agreement between experiment and a theoretical analysis of the resonance orders is obtained.

Calculations in **chapter 5** show that based on the plasmonic whispering gallery cavity presented in chapter 4, plasmon cavities with a very small mode volume can be constructed. These cavities possess a moderate quality factor Q, providing a broadband coupling to emitters. Due to the nanoscale mode volume spontaneous emission can be greatly enhanced in these cavities.

Chapter 6 builds further onto the ring cavity results, showing that they are versatile optical antennas. The near- and far-field properties of the ring antennas are analyzed using optical scattering spectroscopy, angle-resolved CL, fluorescence

spectroscopy and photoelectron-emission microscopy, showing great tunability of transmission and reception of these antennas through control over the local mode symmetries.

In **chapter 7**, CL is used to probe a plasmon mode inaccessible to other techniques that is buried in a metal-insulator-metal waveguide. By engineering the waveguide geometry, a dispersion relation is found that gives at the same time rise to subwavelength confinement, enhanced density of states and an effective index of refraction of 0.

Finally, **chapter 8** describes five possible applications that are inspired by the experimental work presented in chapters 2–7: a nanoscale plasmon laser, a sensitive plasmon sensor, a template-stripping technique to fabricate single-crystal plasmon structures, in in-situ monitor technique during FIB, and a new single photon source.

2

Direct observation of plasmonic modes in Au nanowires using high-resolution cathodoluminescence spectroscopy

We use cathodoluminescence imaging spectroscopy to excite and investigate plasmonic eigenmodes of Au nanowires with lengths of 500–1200 nm and ~100 nm width. We observe emission patterns along the Au nanowire axis that are symmetric and strongly wavelength dependent. Different patterns correspond to different resonant modes of the nanowire. From the observed patterns, we derive the spatial and spectral properties of the wire eigenmodes and determine the dispersion relation for plasmonic Au nanowire modes.

2.1 Introduction

The ever-increasing speed and decreasing size of electronic circuits will meet fundamental limits in the near future. Integration of electronics with optics is promising because optical components can provide a very high bandwidth. However, a simple downscaling of conventional optics to nanometer scale is not possible due to the diffraction limit, hindering true nanoscale applications. Surface plasmon polaritons (SPPs) are electromagnetic waves that are strongly coupled to electron plasma oscillations at a metal-dielectric interface. They are characterized by a dispersion below the light line, enabling reduced wavelengths at optical frequencies [1, 3]. Moreover, they are strongly bound to the metal surface, leading to high

lateral confinement. SPPs propagating along metal nanowires therefore allow photonic manipulation below the diffraction limit.

At small length scales, metal nanowires with finite length behave as plasmonic cavities with resonant eigenmodes [24]. Properties of metal nanowire plasmon resonances have been investigated by extinction measurements on large ensembles [24, 121]. To study the nature of the resonances in greater detail, individual wires have been investigated using near-field scanning optical microscopy (NSOM) [56, 122]. With NSOM however, one is still limited in resolution by the size of the tip (> 50 nm). Furthermore, the tip proximity can have a very strong influence on the optical behavior of the sample [106, 123].

Here we study photonic properties of metal nanowires at high resolution using electron radiation. The electron beam generates a broad spectrum of SPPs, which can subsequently generate radiation that can be detected [113–115]. In this chapter, we use CL imaging spectroscopy for direct observation of plasmonic nanowire modes and determine both spectral and spatial properties of plasmonic eigenmodes. Based on the data, we determine the dispersion relation of SPPs on the Au nanowires.

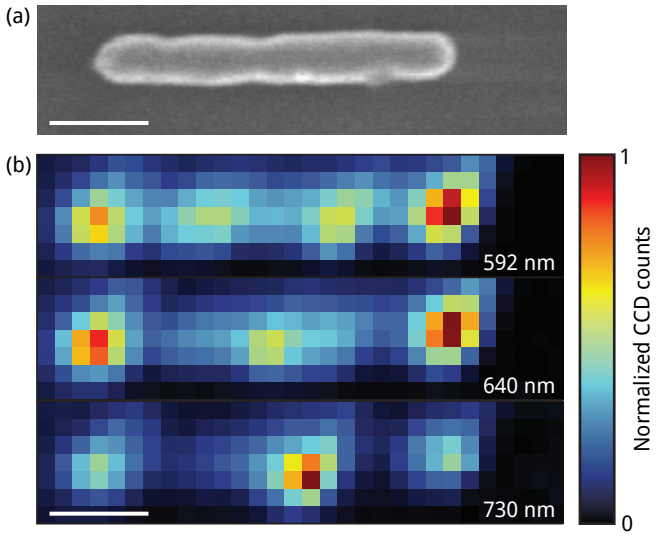

Figure 2.1: **(a)** Scanning electron micrograph of a 725-nm-long Au nanowire on a Si substrate, fabricated using e-beam lithography. **(b)** Cathodoluminescence images of the Au nanowire, at wavelengths of 592, 640 and 730 nm. The light emission pattern is strongly wavelength dependent, indicating excitation of different plasmonic modes. Scale bars: 200 nm

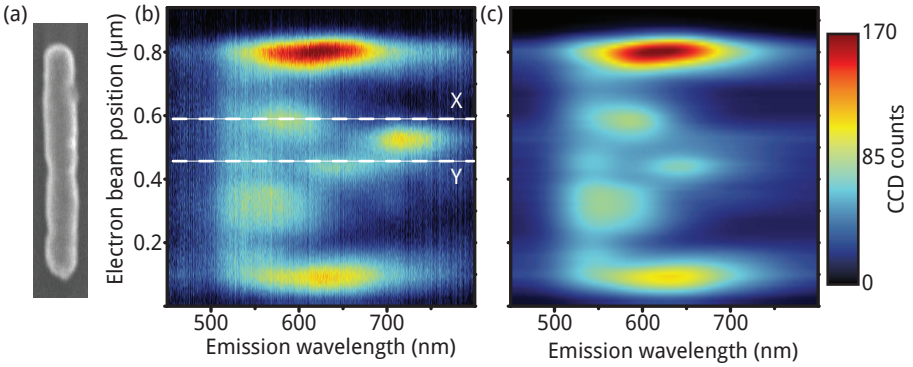

Figure 2.2: **(a)** SEM image of the Au nanowire. **(b)** Cathodoluminescence spectral line scan along the axis of a 725-nm-long and ~100-nm-wide Au nanowire on Si. For every beam position (vertical axis), a spectrum is plotted (horizontal axis). The lines X and Y indicate the position at which the spectra that are plotted in Fig. 2.3 are taken. **(c)** Reconstruction of the line scan image from the fit results, showing that the four resonant mode spectra that have been used, represent all resonances of the wire. The artifact in (b) around 730 nm was removed before fitting, because it does not correspond to a geometric resonance.

2.2 Methods

Au nanowires were fabricated on a doped silicon substrate using electron beam lithography and lift-off. Fig. 2.1(a) shows a scanning electron micrograph of a nanowire specimen. The nanowire width is ~100 nm and the length is 725 nm. Additional nanowires were fabricated with lengths in the 500–1200 nm range. The nanowires were separated by 5 µm, so that no interaction between wires is expected. The silicon provides a highly conductive substrate avoiding charging during electron beam irradiation, but does give a weak CL background signal that is subtracted from the data.

CL spectroscopy was performed in a scanning electron microscope (SEM) extended with a Gatan ParaCL cathodoluminescence system. The electron beam (30 kV, waist < 5 nm) is sent through a hole in a parabolic mirror that is mounted above the substrate. The mirror collects light that is emitted from the sample within a large opening angle (1.4π sr), and collimates it into a spectrometer that is equipped with a CCD detector with a 1340 × 100 pixel array, recording spectra in the 390–950 nm wavelength range.

2.3 Results

Fig. 2.1(b) shows the result of spectral collection during an electron beam scan of a 725-nm-long Au nanowire. The electron beam was scanned in seven rows and 30

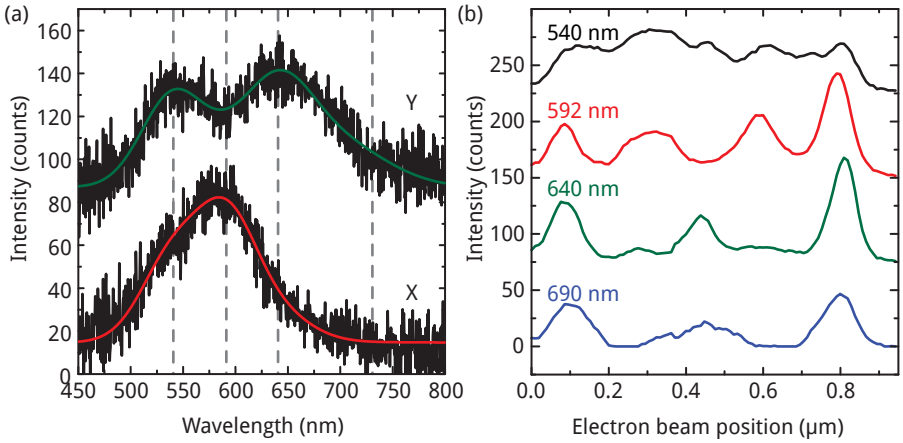

Figure 2.3: (a) CL spectra taken at two different positions along a 725-nm-long Au nanowire (black curves). X and Y correspond to positions as indicated in Fig. 2.2(b). Also plotted in the figure are fits (green and red curves) to these data by a set of four Gaussian resonances at center wavelength of 540, 592, 640 and 690 nm, respectively, indicated in the figure by vertical dotted lines. **(b)** Fitted intensity of each resonance plotted as a function of electron beam position. The 640 nm and 690 nm modes show three maxima, the 592 nm mode shows four maxima, and five maxima are vaguely observed for the 540 nm mode.

columns and for every pixel a spectrum was collected. The figure shows emission in three wavelength windows from this scan, around 592, 640, and 730 nm. For 592 nm we observe a pattern of four maxima, while for 640 and 730 nm, three maxima are observed. These images demonstrate that the electron beam can excite multiple resonances on the wire, that each have a specific spatial profile.

For a more detailed investigation of the data in Fig. 2.1, the electron beam was scanned along the wire axis, and for every beam position spaced by 14 nm, a spectrum was collected (see Fig. 2.1(a) for an SEM image). The result of this scan is shown in Fig. 2.2(b). The spectral axis is plotted horizontally and beam position is plotted vertically. The color scale indicates the recorded intensity. Before further analysis, we removed from the dataset the peak around wavelength 730 nm and position 0.53 μm using a two-dimensional Gaussian fit.*

Fig. 2.3(a) shows the CL spectra for two positions on the wire, which are indicated by X and Y in Fig. 2.2(b). Gaussian fits are performed on these data and show for spectrum X predominant contributions of the resonances peaking at 540 nm and 592 nm, while spectrum Y is made up mostly by the 540 nm and 640 nm resonance. The fitted spectral widths are in the range 40–70 nm, corresponding to a

*We assume that this spot originates from a resonance that is related to an irregularity on the wire, rather than a geometric plasmon resonance. Indeed, this irregularity is observed in the SEM image (see Fig. 2.1(a)).

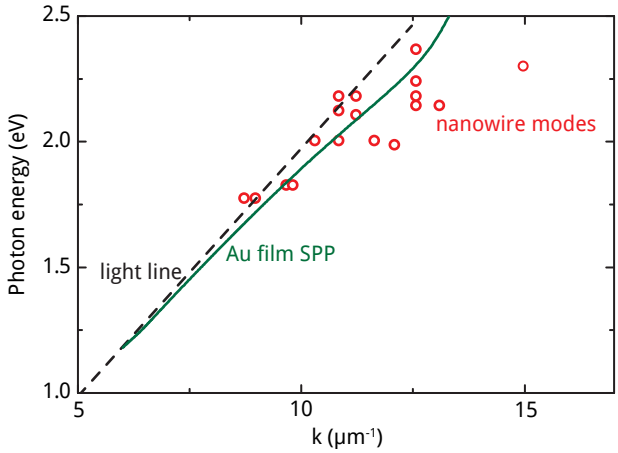

Figure 2.4: Experimentally determined dispersion of surface plasmon modes on Au nanowires with different lengths (circles). Dotted line: light line in vacuum. Solid line: dispersion relation of an SPP on an infinite Au film.

characteristic cavity Q of ~10.

Fig. 2.3(b) plots relative contributions of each resonance at each position on the nanowire. Three clear maxima are observed along the wire for the 640 nm and 690 nm resonances; four maxima are observed for the 592 nm resonance, and, less pronounced, five resonances are observed for the shortest-wavelength resonance at 540 nm. To verify the quality of the analysis, the line scan data in Fig. 2.2(b) were reconstructed by convoluting the four resonance spectra with the spatial profiles. This reconstruction is drawn in Fig. 2.2(c) and shows that the four resonances provide a good representation of the data.

For a further analysis, we treated the nanowire resonances as organ-pipe-like modes, i.e., interfering SPPs travelling in opposite directions that reflect at the wire ends. Furthermore, we assume that the CL emission spectrum from the sample is directly related to the intensity of different eigenmodes at the spot of the electron beam [115, 124, 125].

In this picture, the distance between two intensity maxima in the profiles of Fig. 2.3(b) corresponds to $\lambda_p/2$, where λ_p is the SPP wavelength. For a wave in a dispersive medium, with complex index of refraction, there is a nontrivial phase shift upon reflection from the wire end that can be wavelength-dependent. For this reason, we only determine λ_p from peaks within the wire, to avoid the effect of this phase shift.

From the data in Fig. 2.3(b), and additional measurements on Au nanowires with different lengths in the 700–1200 nm range, several values for λ_p were determined for the corresponding resonance wavelength.

Combining the resonance energy with the corresponding SPP wavelength (λ_p)

yields a data point of the dispersion relation of SPPs on a Au nanowire. Dispersion data for all measurements are plotted in Fig. 2.4. The SPP dispersion for a planar Au film as well as the vacuum light line has also been plotted. As can be seen in Fig. 2.4, the wire modes are close to the dispersion relation for SPPs on a Au-vacuum interface.

Finally, we note that the spatial profiles in Fig. 2.3(b) for 640 and 690 nm are quite similar. This is possibly due to the fact that the wires were not embedded in a homogeneous medium, but were fabricated on top of a silicon substrate, which may cause splitting of wire resonances. More work is required to investigate this further.

2.4 Conclusions

In conclusion, we have used cathodoluminescence imaging spectroscopy to observe the plasmonic behavior of gold nanowires. We show that Au nanowires behave as plasmon resonators, with eigenmodes with distinct spatial profiles. The simultaneous measurement of spectral and spatial characteristics of the modes allowed us to determine the dispersion of SPPs on Au nanowires.

3

Plasmon resonances in a focused-ion-beam-fabricated single-crystal Au ridge

We use focused-ion-beam milling of a single-crystal Au surface to fabricate a 590-nm-long linear ridge that acts as a surface plasmon nanoresonator. Cathodoluminescence imaging spectroscopy is then used to excite and image surface plasmons on the ridge. Principal component analysis reveals distinct plasmonic modes, which proves confinement of surface-plasmon oscillations to the ridge. Boundary-element-method calculations confirm that a linear ridge is able to support highly-localized surface-plasmon modes (mode diameter < 100 *nm). The results demonstrate that focused-ion-beam milling can be used in rapid prototyping of nanoscale single-crystal plasmonic components.*

3.1 Introduction

Surface plasmon polaritons (SPPs) are electromagnetic waves confined to a metal-dielectric interface. As shown in recent experiments, SPPs can be manipulated using waveguides [3, 21] and resonators [38, 56]. Surface plasmon polaritons hold promise for application in sensing, photovoltaics, telecommunications, and opto-electronic circuit integration, due to their ability to concentrate and guide electromagnetic energy at the nanoscale.

Fabrication of components that guide and confine SPPs involves structuring of metals, typically using methods such as electron beam lithography, nano-imprint lithography, self-assembly or templating techniques. These methods offer high spatial resolution, but require complex multi-step processing. Moreover, the metal films, most often obtained by thermal evaporation, typically have a polycrystalline structure. Grain boundaries and surface roughness in polycrystalline films are known to cause undesired scattering of SPPs.

A single-step method to structure metals for plasmonic applications, that is gaining widespread acceptance, is focused-ion-beam (FIB) milling [126, 127]. In a typical FIB system, Ga^+ ions are extracted from a liquid-metal ion source, accelerated to 30 keV, and focused by an electrostatic lens system to a spot size with diameter as small as 5 to 10 nm.

In this chapter we show how FIB milling of a single-crystal Au substrate can be used for highly-reproducible, maskless fabrication of a smooth plasmonic resonator, with minimum lateral dimensions of 50 nm, and surface roughness on the scale of only a few nm. We use cathodoluminescence (CL) imaging spectroscopy to generate SPPs [107, 110] and image resonant modes within the metal nanostructures. The data demonstrate that FIB is an ideal tool for fabrication of nanoscale plasmonic components, in particular when single-crystal metal substrates are employed. Our conclusions are supported by boundary-element-method (BEM) calculations of the local fields at the metal nanostructures [128, 129].

3.2 Methods

Nano-plasmonic device fabrication consisted of focused-ion-beam milling a polished (111) single-crystal Au substrate, grown using the Czochralski process. A 10 pA, 30 keV Ga beam from an FEI Nova 600 dual-beam workstation was rastered in 40 passes over a 4 × 5 µm area, using a 1000 pixel × 1250 pixel grid using a variable dwell time per pixel. Subtractive milling left behind a linear ridge, approximately 590 nm long, 95 nm high and 80 nm wide. Fabrication of such a ridge takes roughly one minute and is very reproducible. Resulting ridge roughness is on the order of a few nm.

Figure 3.1 shows scanning-electron-microscope (SEM) images of the ridge, taken at large azimuthal angle with respect to the normal. Views of the structure at two different polar angles are presented, respectively several degrees off (a), and along (b) the ridge axis. The images reveal rounded features at the top of the ridge and at the base. We attribute this rounding to redeposition of Au during milling as well as the finite diameter of the ion beam (~10 nm). The features visible in the milled area around the ridge are attributed to roughness that was initially present on the substrate, and enhanced under ion milling. We have investigated the crystalline structure of the ridge by scanning ion microscopy, employing focused-ion-beam-imaging from secondary electrons. The absence of contrast within the ridge excludes that a polycrystalline structure was formed.

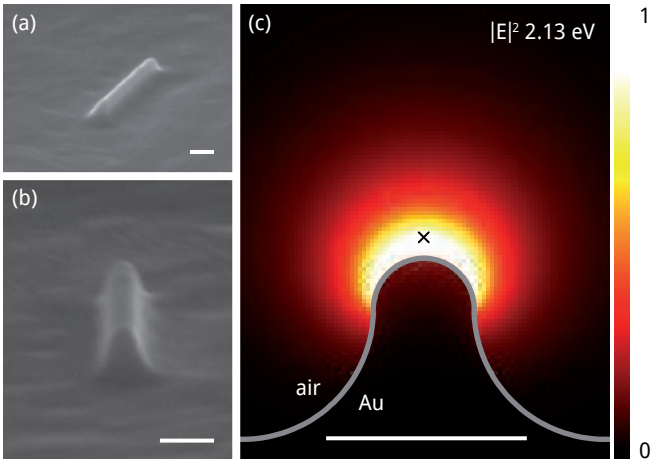

Figure 3.1: **(a)** Scanning electron micrograph of a 590-nm-long linear ridge fabricated in a single-crystal Au substrate using focused-ion-beam milling. The ridge is approximately 95 nm high and 80 nm wide. **(b)** The same ridge from a different angle. **(c)** Boundary-element-method calculation of the field intensity $|E|^2$ near an infinitely long bell-shaped Au ridge. This calculation, performed at a photon energy 2.13 eV and $k_{\|} = 1.14\,\omega/c$, shows that propagating surface plasmons at this energy are well confined to the top of the ridge and do not couple to the planar-surface plasmons, for which $k_{\|} = 1.07\,\omega/c$. Scale bars: 100 nm

CL measurements were done using a FEI XL30 SEM equipped with a parabolic mirror that collects (with a solid angle of 1.4π sr) light generated when the electron beam impinges on the sample. The mirror directs the CL emission into a spectrometer that is equipped with a CCD array detector. Spectral data are corrected for system response. The electron beam is scanned across the sample and for every position of the electron beam a spectrum is collected.

3.3 Results

Figure. 3.2(a) shows a CL image of the ridge, acquired at a center wavelength of 585 nm and a spectral bandwidth of 10 nm. The emission from the ridge is strongly dependent on position: clear maxima are observed at the ends and center of the ridge. Figure 3.2(b) shows spectral line traces (wavelength range: 350–850 nm), along the major axis of the ridge (see dashed line in Fig. 3.2(a)) obtained by integration over 3 pixels (total distance: 21 nm) in the lateral direction of the ridge; the ridge position is indicated at the right-hand side of the figure. The data clearly show that a broad spectrum is emitted when the electron beam dwells on the ends of the ridge, while the emission from the center of the ridge is more sharply wavelength

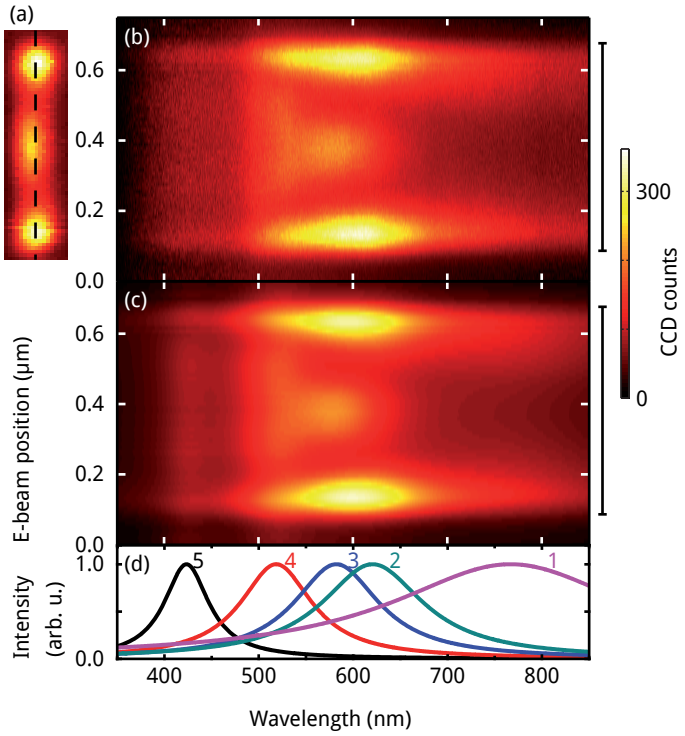

Figure 3.2: **(a)** Light emission from the ridge at 585 nm wavelength upon irradiation with a 30 kV electron beam, as function of electron beam position. **(b)** Cathodoluminescence emission from a single-crystal Au ridge as function of electron beam position and wavelength, measured along the major axis of the ridge (see dashed line in (a)). The ridge position is indicated by the bar to the right of the plot. A broad spectrum is emitted when the electron beam dwells on the ridge ends, while the signal from the ridge center is more sharply wavelength dependent. **(c)** Reconstruction of the data from a fit using a modeling factor-analysis method with a Lorentzian shape imposed on five independent spectra, labeled 1 to 5 and plotted in **(d)**. The calculated data set in (c) closely matches the experimental data in (b)

dependent. As we will show next, these features are related to resonant geometrical modes of the linear ridge nanoresonator.

As previously shown [58, 115, 117, 130], spatial CL images are a direct probe of resonant modes of plasmonic nanostructures. The measured CL spectrum at any position is assumed to be a linear superposition of multiple principal-mode spectra. We extract the principal modes from the data in Fig. 3.2(b) using a factor analysis method [131, 132], that involves solving an eigenvalue problem: a two-dimensional data matrix $D_{(x,\lambda)}$ is defined, with one spectral and one spatial dimension, corresponding to the dimensions of Fig. 3.2(b), respectively, as a product

of two matrices $D_{(x,\lambda)} = R_{(x,n)}C_{(n,\lambda)}$, one having n spatial profiles as columns and the other having the corresponding n spectra as rows. We find that five principal components, found using a scree plot of the logarithms of the eigenvalues versus component number, form a good representation of the data, so that matrices R and C with $n = 5$ can be used to construct the full data set.

We then impose on the mode spectra a Lorentzian shape, parametrized by a peak wavelength and a characteristic width for every spectrum; an initial matrix C is composed of five spectra. The profile matrix R can then be computed by the pseudoinverse [132] of C: $R = DC^{+}$, for which a data set $\hat{D} = RC$ is then calculated. The parameters for the spectra matrix C are then optimized using a least-squares method by minimizing the difference between the original data set D and the generated $\hat{D}$. Figure 3.2(c) shows the obtained $\hat{D}$. The result is in excellent agreement with the data, reproducing the spectral shape and intensity at all positions on the ridge. The resulting five spectra from C are plotted in Fig. 3.2(d). The peak wavelengths in Fig. 3.2(d) range from 425–797 nm. The cavity Q factor, obtained from the width of spectrum 3 is $Q = 5.3$.

Fig. 3.3 displays the spatial profiles of the five spectra along the ridge, as given by R. Spatial profiles for spectra 3 and 4 are characteristic of resonant modes, with one and two antinodes on the ridge, respectively. The spatial profiles for spectra 1 and 2, at longer wavelengths, show antinodes on the ridge ends. The spatial profile for spectrum 5 shows a relatively constant intensity along the ridge; it may be associated to a higher order mode of which the spatial profile cannot be resolved, or transition radiation [133] that does not have spatial dependence. Note that spectra

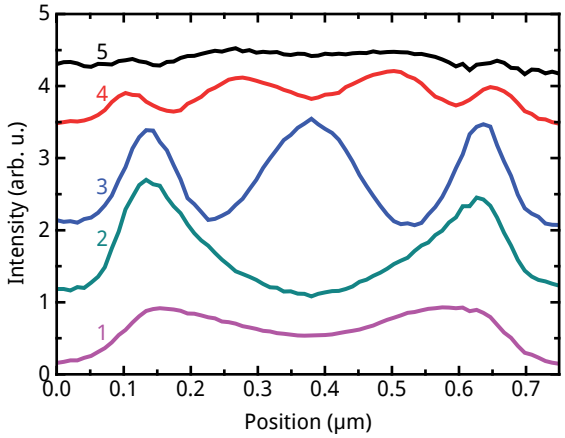

Figure 3.3: Line profiles obtained by a fit of the data in Fig. 3.2(b) using the modeling factor-analysis method of Fig. 3.2. Each consecutive profile is shifted by 1 intensity unit for clarity. Numbers labeling each profile correspond to respective spectra of Fig. 3.2(d). Profile 3 and 4 show resonant modes of the ridge with one and two antinodes on the ridge, respectively.

2 and 3, which are close together spectrally, have very distinct spatial profiles.

This analysis demonstrates the existence of geometrical plasmon modes along the single-crystal Au ridge that are preferentially excited at antinodes in the modal electric field intensity. A boundary element method (BEM) was used to calculate plasmon modes of a geometry similar to that of the experimental structure. Starting from a shape profile as input, the electric field is expressed in terms of charge and current distribution on the ridge, which are calculated self-consistently to fulfill the field boundary conditions. We choose a bell-shaped linear ridge of infinite length characterized by two different radii of curvature, as shown by the grey curve in Fig. 3.1(c). The shape is similar to that of the ridge imaged in Fig. 3.1(b). We first calculated the photonic local density of states (LDOS) in the dielectric just above the top of the ridge (indicated in Fig. 3.1(c) by the black cross). This was done for a range of energies, separating the LDOS into contributions arising from different spatial frequencies $k_\parallel$ along the ridge.

For example, at an energy of 2.13 eV (corresponding to a free space wavelength of 582 nm, and peak 3 in Fig. 3.2(d)), we find an LDOS maximum for $k_\parallel = 1.14\ \omega/c$. This is significantly larger than the corresponding value $k_\parallel = 1.07\ \omega/c$ calculated for SPPs on a planar Au surface (using identical optical constants), consistent with strong mode confinement to the ridge. We investigate the lateral field distribution of the ridge mode by calculating the near field around the ridge excited with a dipole placed above the ridge (also at the position of the cross in Fig. 3.1(c)). By subtracting the dipole field, we calculate the induced field in the plane normal to the major axis.

Figure 3.1(c) shows the calculated values of $|E|^2$ around the ridge. Indeed, the figure shows that the intensity is very much confined to the top of the ridge, with a typical lateral confinement in x and y direction well below 100 nm. From the BEM calculation the plasmon propagation length along an infinitely long ridge is 4 µm ($Q = 43$). This implies that the measured value $Q = 5.3$, is due to the combined effect of ohmic losses (possibly enhanced by the presence of implanted Ga from the FIB process) and radiation losses from the ridge ends.

3.4 Conclusions

In summary, we have shown that using focused-ion-beam milling, a smooth linear ridge that supports surface plasmon resonances can be fabricated on a single-crystal Au substrate. Spatially-resolved cathodoluminescence spectroscopy shows that surface plasmons generated on this ridge are well confined to the ridge and form distinct geometrical modes. The data are confirmed by boundary-element-method calculations of the plasmon field distribution on the ridge, which show that a propagating surface plasmon is confined to the top of the ridge, with a mode diameter <100 nm. These results show that FIB milling of a single-crystal noble metal surface can be used in rapid prototyping of nanoscale surface plasmon components.

4

Modal decomposition of surface plasmon whispering gallery resonators

We resolve the resonant whispering-gallery modes of plasmonic subwavelength ring cavities defined by circular grooves patterned into a gold surface. An interesting interplay is observed between subwavelength confinement and guiding along the groove. Full spatial and spectroscopic information is directly obtained using cathodoluminescence, including details of the nanoscale intensity distribution (spatial resolution 11 ± 8 *nm). Excellent agreement between measurements and rigorous electromagnetic theory is obtained, thus allowing us to assess the symmetry, ordering, degree of confinement, and near-field enhancement of the modes with unprecedented detail.*

4.1 Introduction

Surface plasmons (SPs) are hybrid electromagnetic and conduction electron excitations [1] that allow matching the micrometer-sized wavelength of light at optical frequencies with nanoscopic dimensions of patterned metallic structures. In particular, the interplay between localized and propagating surface plasmons has been intensely investigated with a view to integrated plasmonic devices like plasmon waveguides [13, 15, 134] and plasmon lasers [135]. However, exploiting the field concentration that is offered by such nanostructures requires a probe of the

plasmonic modes at nanometer scale resolution. Near-field scanning optical microscopy (NSOM) provides a resolution down to ~50 nm, although a coated tip can interact with the local modes thus producing distorted information. In contrast, fast electrons constitute a non-invasive probe of metal structures with the potential for true nanometer spatial resolution to retrieve spectral information through induced light emission (cathodoluminescence, CL) [115] or via the analysis of electron energy loss in the case of thin samples [124]. The field of a moving electron [136] diverges close to its trajectory. The interaction of the electron with the photonic structure being probed is governed by this divergent field. Consequently, there is no limit to the resolution, which in experiment is only limited by the finite size of the electron beam.

In this chapter, we investigate whispering-gallery plasmon excitations [23, 60, 61, 137, 138] supported by grooves of annular shape that share a unique combination of features associated to both standing wave modes and propagating modes. We pattern the grooves in a single-crystal gold surface and study the spatial and spectral evolution of the modes with unprecedented detail by using cathodoluminescence spectroscopy and boundary-element-method (BEM) calculations. We report excellent agreement between experiment and theory, which allows us to classify plasmon modes according to their azimuthal symmetry and radial order. We formulate a dispersion model relating circular grooves to straight grooves that explains satisfactorily the detailed dependence of mode frequencies and spatial distributions on ring radius and groove depth.

4.2 Methods

Nanoresonators consisting of ring-shaped grooves (Fig. 4.1(a)) were fabricated in a Czochralski grown and polished (RMS roughness < 1 nm) single-crystal Au substrate, by focused-ion-beam-milling (FIB). Ring radii R range from 100–300 nm; the depth d of the groove ranges from 130–530 nm. The FIB process yields a very smooth shape (roughness < 5 nm) with high control over depth. Cross-sections that reveal the depth profile of the grooves were made using FIB-induced Pt deposition and subsequent cross-sectional milling (Fig. 4.1(b)).

On these structures we excite surface plasmons with the 30 keV electron beam of a scanning electron microscope [58]. The resulting light emission is collected by a parabolic mirror covering a 1.4π sr solid angle, and led to a spectrometer equipped with a CCD array detector. We collect spectra for every electron beam position while the beam is scanned. Spectra are corrected for system response by comparing a recorded CL spectrum from unstructured Au to an analytical calculation of the transition radiation spectrum [133]. Using this method, the measured intensity can be expressed in terms of photon emission probability per incoming electron per nm spectral bandwidth.

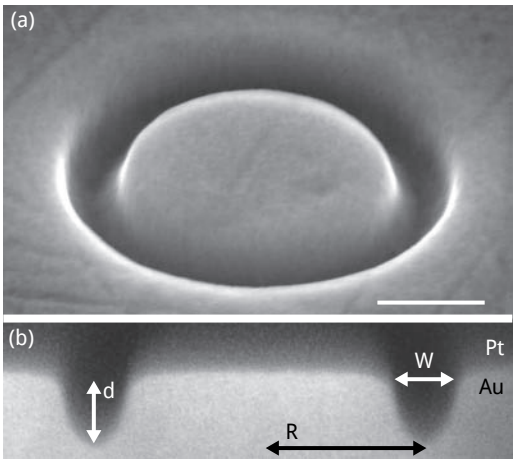

Figure 4.1: Scanning electron micrographs of a FIB-fabricated ring groove in single-crystal Au. The ring radius R is ~300 nm. **(a)** Top view. **(b)** A FIB-milled cross-section through the ring. The dark material is a Pt protection layer used for imaging. The cross-section allows us to determine the precise groove geometry. Scale bar: 200 nm

4.3 Results

Figure 4.2(a) shows measured CL spectra for rings with different radii and constant depth and groove width. The electron beam was scanned in 10 nm steps over a 1 μm long line through the center of a ring, with an exposure time of 0.5 s per step. The light spectrum emitted during this scan was collected and summed. The figure shows such spectra for rings with radius R increasing from 100 to 300 nm, at a fixed groove depth of 130 nm. Interestingly, the CL emission spectrum from the rings has one or more distinct peaks, which shift to longer wavelength for increasing radius. Moreover, there are new peaks that appear as the radius is increased. As we will show, the different peaks in the emission spectra can be attributed to geometric plasmonic resonances that couple to radiation.

We studied how these resonances are tuned by the groove depth, varying depths from 130 nm to 530 nm while keeping the radius fixed to 200 nm. The collected spectra are shown in Fig. 4.3(a). For increasing depth, the peaks in the CL spectrum are seen to shift to longer wavelengths. These results show that the ring structure supports surface plasmon resonances that are very dependent to the geometry, with a remarkable sensitivity for the depth of the groove.

Boundary-element-method (BEM) calculations [128] were performed to determine the electric field distribution in the axially-symmetric ring geometry of the CL experiment. In this method, the electric field is expressed in terms of charges and currents on the boundary of the geometry, which are calculated self-consistently to

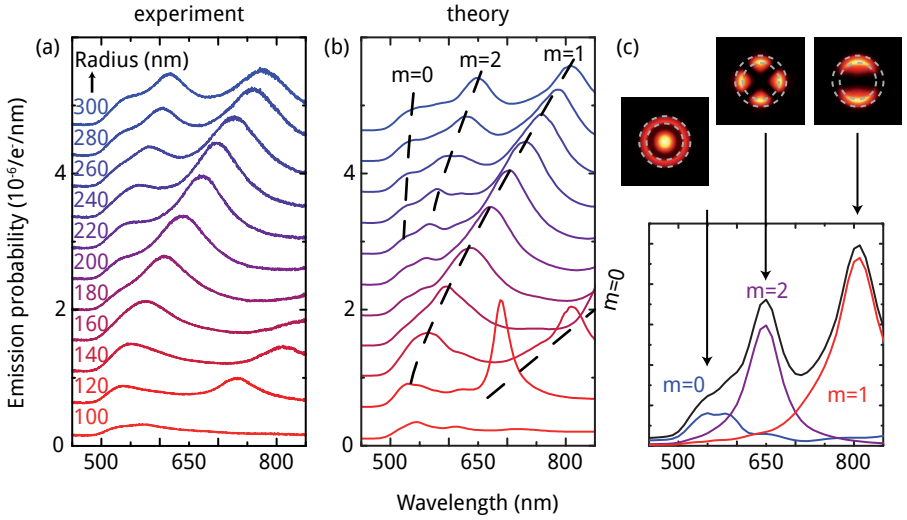

Figure 4.2: Plasmonic ring resonances for rings with increasing radius. **(a)** Cathodoluminescence (CL) spectra from rings in single-crystal Au with radii increasing from 100 nm (bottom) to 300 nm (top) in 20 nm steps and a constant depth of 130 nm. **(b)** Boundary-element-method calculated CL spectra. The azimuthal mode number m is indicated for the major resonance peaks. Spectra are offset vertically for clarity. **(c)** The contributions of modes with different m to the total cathodoluminescence for a ring with radius 300 nm. The corresponding calculated azimuthal near field mode profiles are plotted on top. Dashed circles indicate the location of the groove.

fulfill the field boundary conditions. We use optical constants for single-crystal Au from spectral ellipsometry as input for the calculations, which are performed in the frequency domain. Analogous to the experiment, the far-field emission spectrum resulting from incoming electrons impinging on the ring structure was calculated. The calculated results for rings with increasing ring radius are shown in Fig. 4.2(b). The features seen in the calculated spectra are in excellent agreement with those of the experimental spectra, reproducing the shifts to longer wavelengths with increasing radius, the appearance of additional resonances at shorter wavelengths, and the resonance peak intensities. Figure 4.3(b) shows the calculated CL spectra for rings with increasing groove depth. The presence of a large resonance peak for shallow rings and the appearance of additional resonances at short wavelengths for deeper rings are well reproduced. Deviations of the wavelength and amplitude of the resonant peaks is attributed to slight differences between experimental and calculated geometry that become more prominent as the groove depth is increased. These differences are probably most important in the bending radius of the bottom of the groove, to which a V-groove plasmon is very sensitive [139].

Figure 4.4(a) shows the light intensity collected as the electron beam (0.5 nA

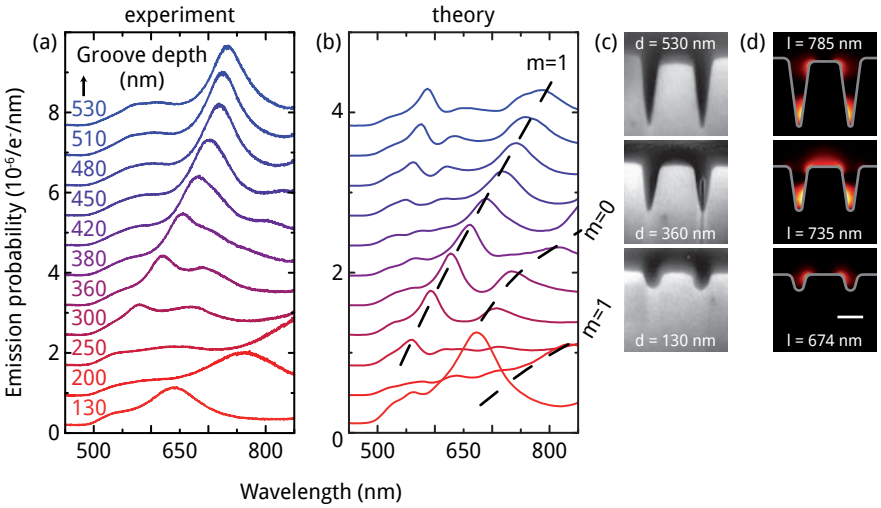

Figure 4.3: Plasmonic ring resonances for rings with increasing groove depth. **(a)** CL spectra from rings with constant radius of 200 nm and a groove depth increasing from 130 (bottom) to 530 nm (top). **(b)** BEM calculated CL spectra. The azimuthal mode number m is indicated for the major resonance peaks. Spectra are offset vertically for clarity. **(c)** Scanning electron micrographs of ring grooves with different groove depths (see insets). **(d)** Calculated near field $|E|^2$ corresponding to the rings in (c), showing distinct radial profiles at wavelengths shown by insets. For the deepest ring, an $n = 2$ mode appears. The strong asymmetry in the mode profiles indicates the coupling of the groove mode across the disk. Scale bar: 200 nm

beam current) is scanned over a 300 nm-radius ring ($d = 130$ nm): the intensity is plotted as a function of emission wavelength (horizontal axis) and electron beam position (vertical axis). Emission maxima in the plot correspond to the resonant peaks in the topmost spectrum in Fig. 4.2(a). The image shows that the excitations that give rise to these peaks have a different spatial dependence, illustrating the spatial mapping of resonant modes by CL plasmon microscopy. Figure 4.4(b) shows the corresponding BEM-calculated spectra. The features of the experimental data set in both spectral and spatial dimension are very well reproduced by the calculation. The white curves in Fig. 4.4(b) are line traces through the central peak in the data of a and b. The higher intensity measured on the center plateau is attributed to factors not accounted for in the calculation, such as scattering from roughness. We fit the outer half of the peaks at the position of the steep rise near the edge of the groove (i.e. at ± 250 nm) in measurement and calculation with a Gaussian distribution and find $\sigma = 17.7 \pm 1.1$ nm for the experimental and $\sigma = 16.7 \pm 0.5$ nm for the calculated data. We find for the corresponding spatial resolution of the CL scan a value of $2\sigma = 11 \pm 8$ nm.

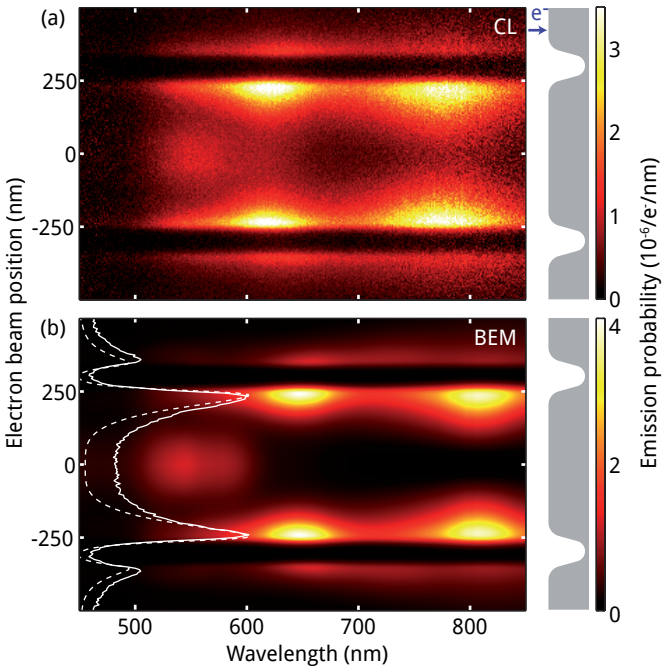

Figure 4.4: Spatial mapping of modes by cathodoluminescence plasmon microscopy. **(a)** Cathodoluminescence spectra as function of electron beam position as the beam is scanned through a ring groove with $R = 300$ nm radius along a 1 μm line in 5 nm steps (the ring geometry is drawn to the right of the figures). The center of the ring is at position 0. The maxima in this plot correspond to the peaks in the topmost spectrum of Fig. 4.2(a). Note that different resonances are excited at different positions; the $m = 0, n = 1$ resonator mode at 535 nm is mostly excited at the center of the ring, while the modes at 620 nm ($m = 2$, $n = 1$) and 775 nm ($m = 1$, $n = 1$) are predominantly excited at the edge of the center plateau. **(b)** Boundary-element-method calculated CL spectra for the experiment in (a). White curves: line traces through CL (solid) and BEM (dashed) data at the central peak (620 and 650 nm, respectively) show the 11 nm resolution of CL plasmon microscopy.

In order to understand the nature of the resonant behavior, we have used BEM calculations to obtain the azimuthal dependence of the resonant electric field, described by $\mathbf{E}_m(r,z,\varphi) = \mathbf{f}_m(r,z)e^{im\varphi}$, with a radial part and an azimuthal number m. Figure 4.2(c) shows the calculated CL spectrum of a 300-nm-radius ring as a sum of $m = 0,1,2$ contributions. For each m, a top view of the modal electric field intensity is plotted. The dashed curves in Fig. 4.2(b) and Fig. 4.3(b) indicate the resonance peaks assigned to these m numbers. Figure 4.2(b) shows for small rings a rotationally-symmetric field ($m = 0$), and dipolar ($m = 1$) and quadrupolar ($m = 2$) resonances as the ring radius is increased. For the 300-nm-radius ring a second $m = 0$ resonance is found near 550 nm, which is associated to a higher-order

radial mode. Similarly, for rings with increasing depth (Fig. 4.3(b)), the shortest-wavelength $m = 1$ mode is related to a higher-order radial field dependence. The cross-sectional views of the electric field intensity $|E|^2$ in Fig. 4.3(d) show the difference in the field distribution of these radial modes, from which we define a radial mode number n (number of antinodes in the field) for $m > 0$ resonances.

The observation of well-defined azimuthal modes, together with the radial field profiles of Fig. 4.3 indicates that the localized plasmons found here are whispering gallery ring-resonator modes [15] originating from circulating groove plasmons [10, 11, 13, 14] that are strongly coupled across the metal disk. The analogy with straight groove waveguides is demonstrated using two-dimensional BEM [140] calculations. We find the dispersion and field profile $|E|^2$ of straight groove modes according to our particular groove geometry (Fig. 4.1(b)). The photonic local density of states (LDOS) was calculated in the groove as a function of energy and separated in contributions arising from different spatial frequencies along the groove. For each energy, we determine the modal wave vectors from the maxima in the LDOS. The modes thus found are shown in Fig. 4.5 for different groove depths. The figure shows that deep grooves support modes with wave vector $k_\parallel$ (directed along the groove) larger than the SPP wave vector for a planar Au surface, indicating strong localization to the groove, with a confinement that grows with increasing groove depth [14]. The 530-nm-deep groove also shows an $n = 2$ mode with a smaller $k_\parallel$ and an additional node in its near field [13]. The ring resonance condition $k_\parallel = m/R$, based on an integer number of wavelengths in the circumference of the ring, is indicated in Fig. 4.5 for a large ring with radius $R = 600\,\text{nm}$ by vertical dashed lines, predicting resonances with $m = 6, 7$ and 8 for the $n = 1$ mode at wavelengths of 742 nm, 659 nm, and 611 nm, respectively. The inset of Fig. 4.5 shows the LDOS spectrum, calculated in the $R = 600\,\text{nm}$, $d = 530\,\text{nm}$ ring geometry. The $m = 6, 7, 8$ components of the LDOS show maxima that coincide with these predicted resonances. The modal field intensity for this geometry, also plotted in Fig. 4.5, indeed shows the strong confinement to the groove.

From the calculated dispersion in Fig. 4.5 it also follows that for an $R = 240\,\text{nm}$, $d = 130\,\text{nm}$ ring, the dispersion of the $n = 1$ mode would correspond to an $m = 2$ resonance at 754 nm. Instead, Fig. 4.2(b) shows that this resonance occurs at 580 nm. This blue shift is attributed to coupling of the groove mode across the disk [141]. It occurs in all resonator geometries with small diameter and/or shallow groove depth. This interaction is further corroborated by the strong asymmetry of the CL signal across a groove observed in Fig. 4.4 as well as the field asymmetry found inside the grooves in Fig. 4.3(d). The very strong red shift for the $m = 1, n = 1$ mode in Fig. 4.3 for increasing groove depth is due to the combined effect of a decreasing interaction across the disk and an increasing wave vector along the groove.

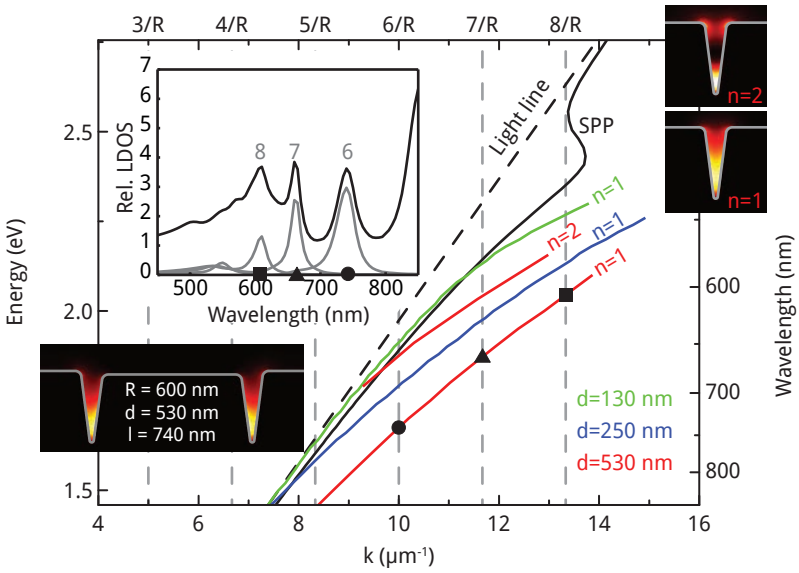

Figure 4.5: Analogy between the dispersion of linear groove modes and ring resonances in annular grooves. The energy of the $n = 1$ mode is displayed for 130 nm, 250 nm and 530-nm-deep linear grooves as a function of the wave vector $k_{\parallel}$ along the groove. For the 530 nm-deep groove, the less confined $n = 2$ mode is also plotted. The near-field pictures on the right show the electric field intensity for these $n = 1$ and $n = 2$ modes. A $k_{\parallel}$ exceeding the SPP $k_{\parallel}$ indicates localization to the groove, which increases for deeper grooves. Vertical dashed lines show $k_{\parallel} = m/R$ for $m = 3$–8, indicating the ring resonance condition in an $R = 600$ nm radius ring. Top left inset: LDOS spectrum calculated in the groove of a $d = 530$ nm, $R = 600$ nm ring. Contributions of the $m = 6, 7, 8$ azimuthal components are shown. Symbols in the inset correspond to the symbols in the main figure, indicating the wavelengths for the ring resonance condition. Indeed, the LDOS components show ring resonances at these wavelengths, confirming a virtually absent interaction for deep, large diameter rings. The bottom left inset shows the corresponding resonant $n = 1$, $m = 6$ field intensity.

4.4 Conclusions

In conclusion, we have unveiled whispering-gallery plasmons in nanoscale ring grooves patterned in single-crystal gold. The symmetry, ordering, and confinement of these modes has been resolved with an unprecedented combination of spatial and spectroscopic resolution ($2\sigma = 11 \pm 8$ nm), by combining scanning cathodoluminescence spectroscopy and rigorous electromagnetic modeling of both plasmon modes and electron-metal interaction. The plasmon resonances of the ring groove structure originate from circulating groove plasmons with different azimuthal mode number ($m = 1, 2$ in Fig. 4.2). We have observed that as the ring

radius and groove depth become smaller, the groove plasmon modes become less localized and the ring resonances undergo a blue shift. This shift is explained by interaction over the central disk of the propagating groove plasmon with itself in resonances with $m \neq 0$ azimuthal symmetry, where the plasmon is confined in the grooves even for ring diameters as small as half a wavelength. In contrast, $m = 0$ modes are found to have significant intensity in the center plateau of the ring. The reported modes are ideally suited to realize plasmon-assisted nanolasing and parallel optical sensing at light wavelengths matching the designed modes of the rings. Further progress in these directions is underway, facilitated by the reported combination of comprehensive experimental and theoretical understanding of this plasmonic system.

5

Broadband Purcell enhancement in plasmonic ring cavities

We present a theoretical study of a surface plasmon ring resonator geometry that shows strong spontaneous emission control due to an extremely small optical cavity mode volume. V-grooves made in the surface of a metal confine whispering gallery surface plasmon polariton modes at the bottom of the groove, with the confinement determined by groove depth and width. Resonances in ring-like cavities defined by grooves patterned into circular shape, determined using the boundary element method, are in agreement with calculations based on dispersion for linear V-grooves. Cavity quality factors are relatively insensitive to cavity geometry (Q = 10–50*), while mode volume is very sensitive to small differences in the cavity shape. The smallest mode volume* $V = 0.00073\,\lambda_0^3$ *is found for a ring with a 10-nm-wide, 100-nm-deep groove with straight sidewalls and a diameter of 180 nm. Purcell factors well above 2000 are found in the energy range from* E = 1.0–1.8 *eV depending on cavity geometry. For a given cavity geometry the Purcell enhancement is observed over a broad spectral range (*50–100 *meV), enabling application of these cavities beyond the typical low temperature cavity QED experiments.*

5.1 Introduction

Control over spontaneous emission is key to many photonic applications, and also a subject of great fundamental interest. According to Fermi s Golden Rule, the rate of spontaneous emission of an optical emitter is proportional to the local density of optical states (LDOS). In a homogeneous medium, the spontaneous emission rate of an emitter is fixed and it depends on the transition dipole moment of the emitter and the refractive index of the surrounding medium. In an environment that is structured at the scale of the wavelength the LDOS can be spatially controlled [142]. As a result, the spontaneous emission rate of an emitter can be locally increased or decreased, depending on the geometry.

An optical microcavity provides an environment in which the LDOS can be strongly increased. The increase of spontaneous emission in the cavity, known as the Purcell effect [143], is given by the Purcell factor,

$$F_P = \frac{3}{4\pi^2}\frac{Q}{V}\left(\frac{\lambda}{n}\right)^3, \tag{5.1}$$

where Q is the cavity quality factor, which is proportional to the time light is stored in the cavity, and V the mode volume, a measure for the spatial extent of the modal field inside the cavity; n is the refractive index of the cavity medium.

Optimization of the Purcell factor enables low-threshold lasing, bright luminescent sources, and the possibility to avoid quenching in materials that classically show strong non-radiative decay. Most work so far has focused on achieving high Purcell factors by optimizing Q, for example in Fabry-Perot, microsphere [144, 145], micropillar [146, 147], microtoroid [148], microdisk [149] or photonic crystal cavities [150, 151]. The highest Q factors were reached in microspheres ($Q = 10^{10}$) [144]; in integrated on-chip microcavities a Q of 10^7 was observed [148].

One problem with using these high-Q cavities is that due to the narrow line width associated with the high cavity Q, the interaction between light and matter occurs only over a very narrow bandwidth. Most emitters however, have emission spectra with a broad line width. As a result, the coupling of these emitters to the cavities is relatively weak. The highest decay rate enhancements reported so far were measured on photonic crystal cavities doped with semiconductor quantum dots [152], for which a 75-fold increase in decay rate at a wavelength of 945 nm was found. Moreover, such enhancements were only found at low temperature [146, 152].

An alternative way to increase the Purcell factor is to reduce the mode volume. If this can be achieved, high Purcell factors can be observed at modest Q, and thus over a broader bandwidth, enabling broadband light sources with high emission rate at room temperature.

So far, the smallest mode volumes are observed in photonic crystals [153], in which the mode volume V is limited by diffraction; typically $V = (\lambda/n)^3 \approx 0.1\,\mu m^3$. Much smaller mode volumes can be achieved using surface plasmon polaritons (SPPs), surface waves at a metal-dielectric interface resulting from the coupling

between photons and the free electron plasma of the metal. SPPs are strongly bound to the interface and evanescently decay into either medium. The field confinement offered by plasmons allows enhanced interaction with emitters even for propagating modes [30, 154].

Three-dimensional confinement of plasmons was demonstrated in Fabry-Perot-type plasmon cavities where SPPs propagate either on a single metal interface or in the dielectric gap in a metal-insulator-metal (MIM) geometry [38, 155, 156], leading to a mode volume of $V = 0.01\,(\lambda/n)^3$. Most recently, 3D MIM cavities were demonstrated having a smallest (predicted) volume $V = 0.00033\,(\lambda/n)^3$ for a 105 nm diameter MIM disk [119].

Indeed, MIM waveguides offer the smallest possible confinement of light, thus enabling the largest Purcell factor. So far, however, MIM cavities are made of closed material layers and are thus not easily accessible for optical probes of the LDOS. An MIM plasmon geometry that has a more open geometry is a V-groove made in the surface of a metal [14]. Such V-grooves provide strong confinement of light in the lateral dimension and if made into a ring they form a 3D plasmon cavity. In contrast to the planar MIM cavities demonstrated so far, these V-grooves can be easily infilled with optical emitters or gain media.

Ring resonators based on V-groove plasmon waveguides [11, 13, 15] support whispering-gallery resonances due to circulating plasmons even when the circumference fits only a single plasmon wavelength, as we have shown previously [19]. The resonances are easily tunable through both the diameter of the ring and the shape of the groove and they have an extremely small mode volume. The groove void allows for incorporation of emitters near the maximum of the electric field. Ring resonators based on surface plasmons are therefore a promising candidate for use as high F_P cavities.

In this chapter we investigate these V-groove ring cavities with the aim of determining the smallest possible mode volume while maintaining a reasonable cavity Q. We find a mode volume as small as $0.00073\,\lambda_0^3$ at a cavity $Q = 10$–50. The corresponding Purcell factor is $F_P > 2000$. This opens up possibilities for broadband enhanced interaction between an emitter and light stored in the ring cavity.

5.2 Methods

We have performed boundary-element-method (BEM) calculations [128, 129] in which Maxwell s equations are rigorously solved for an electric field that is expressed in terms of charges and currents on the metal surface. We first use a two-dimensional boundary (as shown in Fig. 5.1(a)) to calculate the optical properties of an infinitely-long groove in an otherwise planar Au surface. In the direction along the groove (z), the fields are taken to evolve as $e^{ik_z z}$. A similar groove geometry was then used to define a ring cavity (Fig. 5.1(b)). Here, solutions for the field depend on azimuthal angle φ as $e^{im\varphi}$, with $m = 0, \pm1, \pm2, \ldots$. In the calculation, contributions up to an order $|m| < 5$ were taken into account, high

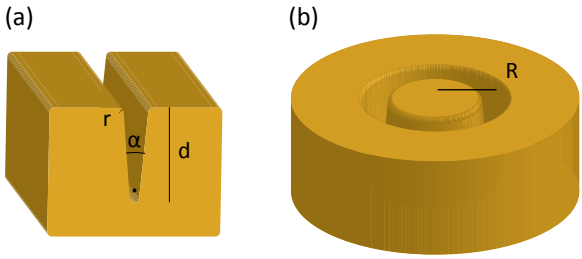

Figure 5.1: The boundary geometry as used in the calculations. **(a)** Groove parametrized by minor radius r, opening angle α, and depth d, as used in 2D-BEM calculations. The solid dot indicates the position at which the local density of states was calculated. **(b)** Ring resonator based on the groove of (a), having major radius R, used in axially symmetric BEM calculations. The minor radius r is used for smoothing the external edges and the bottom wedge of the groove.

enough for the results to reach convergence. The calculations are performed using tabulated optical constants for Au [157]. The ring resonator is parametrized by 4 parameters: major radius R, groove depth d, opening angle of the groove α and minor radius $r = 5\,\text{nm}$ that describes the curvature of the corners and bottom of the groove. In the calculations we have varied α from 0° to 10°, d from 100 to 1000 nm, and R from 50 to 600 nm. These parameters are at the limits of state-of-the-art fabrication techniques like focused-ion-beam milling. Recent advances [19, 32, 158] show that grooves can be made narrower and narrower and that the ultimate limits of fabrication have not been reached. The choice of Au is motivated by existing experimental measurements of the resonance spectra of ring resonators on this material [19].

5.3 Results

Dispersion in straight grooves

Before treating resonant cavities, we first present the calculated dispersion relation and mode profiles for linear V-grooves. Using BEM we calculate the local density of optical states (LDOS), associated with the electric field, at a point inside the groove, at 10 nm above the bottom (solid dot in Fig. 5.1(a)). The LDOS is calculated for a range of energies and separated into contributions arising from different wave vectors k_z along the groove*. Optical modes of the geometry show up as maxima in the LDOS. For each energy, we find the k_z for which the LDOS peaks and so obtain the dispersion relation in this geometry. Figure 5.2(a) shows the dispersion of the

*The LDOS for linear grooves is separated into the contribution of different k_z components. This quantity is defined in the 2D plane normal to the groove direction and it is normalized such that its integral over k_z gives the LDOS at a point in 3D space.

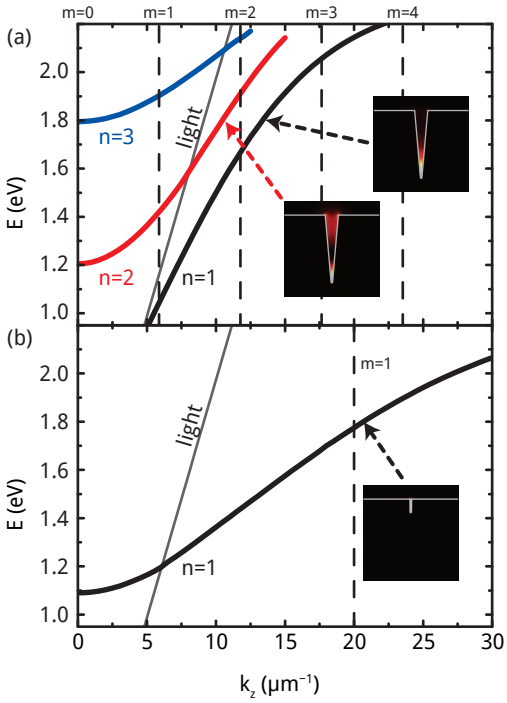

Figure 5.2: Dispersion of plasmons propagating in straight grooves in Au derived from BEM calculations of the LDOS. **(a)** V-grooves with $d = 500\,\text{nm}$, $\alpha = 10°$. The lowest order groove mode ($n = 1$) is below the light line in this energy range, so that it does not couple to light or planar SPPs. Higher orders have smaller k_z and experience cutoff. For the two lowest orders, the electric field intensity is plotted at 1.8 eV. The $n = 2$ mode has an extra node in its field distribution. **(b)** Dispersion for a $d = 100\,\text{nm}$, $\alpha = 0°$ (width 10 nm) groove with the field intensity for the $n = 1$ mode at 1.8 eV. Vertical dashed lines in both plots indicate the condition $k_z = m/R$ required for a resonance in a ring with radius $R = 170\,\text{nm}$ (a) and $R = 50\,\text{nm}$ (b), respectively. Ring resonances are expected at the intersection of the plasmon dispersion with these lines.

three lowest-order plasmon modes for grooves with $d = 500\,\text{nm}$ and $\alpha = 10°$. Also plotted is the light line in vacuum. The dispersion of the lowest-order plasmon mode ($n = 1$) deviates significantly from the light line for energies as low as 1.1 eV, in contrast to what is observed for planar SPPs. As a result, the $n = 1$ groove mode does not couple to light or planar SPPs. Similar high dispersion has also been found for plasmons in planar MIM slabs [37, 159]. The groove also supports higher order modes, with mode number n defined by the number of field antinodes. The insets of Fig. 5.2(a) show the distribution of the electric field intensity for the $n = 1,2$ modes. Both modes are confined well inside the V-groove with the $n = 1$ mode

concentrated in the bottom of the V-groove. This demonstrates how these linear V-grooves offer strong 2D confinement. The effective index of a planar MIM-plasmon is strongly dependent on the separation between the two metal interfaces; it increases for smaller separation [37]. The strong confinement to the groove can be understood from the fact that the plasmon is concentrated in the region with the highest effective index, which is near the bottom of the groove, where the metal walls are closest together [160]. Figure 5.2(a) shows that the $n = 2$ and $n = 3$ modes have a threshold within the energy range of the graph. At the threshold energy, the groove mode has no wave vector in the groove direction and is thus a completely delocalized plasmon along the groove [156].

The dispersion of groove plasmons can be further increased by narrowing the groove, as is shown in Fig. 5.2(b), which shows the dispersion of the groove plasmon in a $d = 100\,\text{nm}$, $\alpha = 0°$, 10-nm-wide groove, in which the vertical walls are parallel [160]. For example, at 2.0 eV, k_z is three times larger than it is for free space light. As is shown in the inset in Fig 5.2(b), the plasmon field is very well confined inside the narrow groove. The field of this mode at 1.8 eV is plotted at the same length scale as in Fig. 5.2(a), demonstrating the very high degree of confinement possible using V-groove plasmons. In this groove with parallel sidewalls, the field is not confined to the bottom, but there is still strong vertical confinement due to the small depth of the groove ($d = 100\,\text{nm}$). These shallow grooves show modal cutoff at ~1.1 eV.

Ring resonances

Next, we study plasmons confined in V-groove ring cavities. Resonant circulating groove plasmons satisfy the relation $k_z = m/R$, where k_z is the wave vector of the straight-groove plasmon, m is the azimuthal order, i.e. the number of wavelengths that equals a circumference, and R is the ring radius. We can now find the resonant energies for a ring with radius R using the calculated dispersion relation. Dashed lines in Fig. 5.2(a) indicate the values of k_z for resonances in an $R = 170\,\text{nm}$ ring. At the energies of intersection of a groove mode with a dashed line, the resonance condition is satisfied. We verify that these resonances indeed exist by calculating the LDOS spectrum. Figure 5.3(a) shows the BEM-calculated LDOS, normalized to the vacuum LDOS, in an $R = 170\,\text{nm}$ ring with a $d = 500\,\text{nm}$, $\alpha = 10°$ groove corresponding to the straight groove of Fig. 5.2(a). The peaks in the spectrum (dashed curve) represent optical resonances of the geometry. The separate azimuthal contributions to the LDOS are indicated by the drawn curves, with the corresponding m values indicated next to the curves. The arrows drawn near the top horizontal axis of Fig. 5.3(a) indicate ring resonance energies derived from Fig. 5.2(a); the numbers denote the corresponding azimuthal order m. Both the resonant energies and the mode numbers agree well.

Figure 5.3(b) shows the LDOS spectrum of an $R = 50\,\text{nm}$ ring with a $d = 100\,\text{nm}$, $\alpha = 0°$ groove, corresponding to the geometry of Fig. 5.2(b). Due to the small radius, there are fewer resonances over the spectral range in Fig 5.3. Interestingly, the LDOS

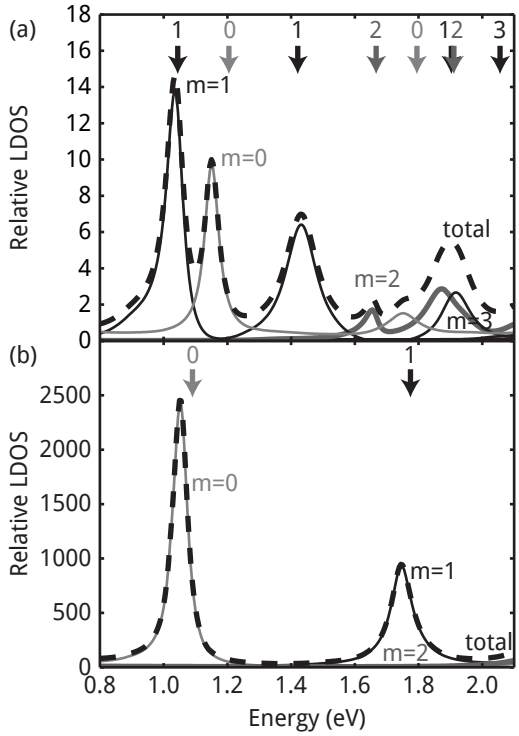

Figure 5.3: Photonic local density of states (dashed lines) in the groove of a ring resonator at 10 nm above the groove bottom. **(a)** Ring with $d = 500\,\text{nm}$, $\alpha = 10°$, $R = 170\,\text{nm}$. **(b)** Shallower, smaller ring with $d = 100\,\text{nm}$, $\alpha = 0°$, $R = 50\,\text{nm}$. The LDOS, which is normalized to the vacuum LDOS, peaks at the resonance energies. Separate azimuthal mode (m) contributions are plotted by the solid curves, following from the 3D calculation. For comparison, arrows indicate the resonant energies derived from the straight-groove dispersion (Fig. 5.2) with the corresponding m. Even for small ring radius the model predicts the resonances reasonably well.

reaches values well over 2000, demonstrating the potential of these rings for strong spontaneous emission control. Analogous to panel (a), the arrows in Fig. 5.3(b) indicate resonances derived from the straight-groove dispersion of Fig. 5.2(b). Again, good agreement is observed.

Figure 5.3 shows that plasmonic ring resonances, even in resonators with single-wavelength circumference ($m = 1$), directly follow from the straight groove plasmon dispersion. The small deviations between the energies indicated by the arrows and the actual resonances in the LDOS are attributed to interaction of the V-groove modes over the center plateau [19], which is not included in the simple straight-groove model.

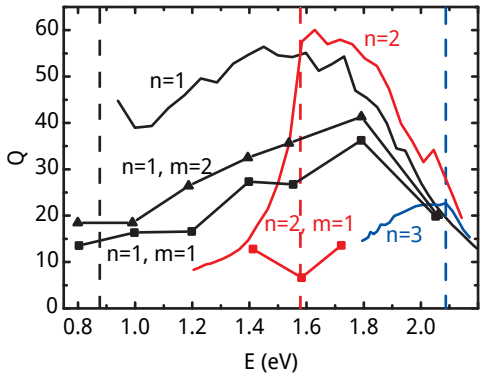

Figure 5.4: Quality factors derived from LDOS calculations. Drawn lines: Q factor of the $n = 1, 2, 3$ linear groove modes in $d = 500\,\text{nm}$, $\alpha = 10°$ grooves. For the $n = 1$ mode, these Q values correspond to propagation lengths in the range 1–7 μm. Vertical dashed lines indicate the energy at which the mode crosses the light line. Squares indicate $m = 1$ resonances, triangles indicate $m = 2$ ring resonances. Ring radii in this figure were varied for each data point to achieve the required resonance and range from 56 to 522 nm.

Quality factor of ring resonances

Next we study the quality factor Q of the rings and compare it to the propagation length in linear grooves. In a cavity, the Q factor is a measure of the number of optical cycles that the light remains stored in the cavity. For linear V-grooves, an effective Q can be related to the propagation length. We derive it from the LDOS calculations made to find the dispersion relation (as in Fig. 5.2), deriving Q from the width of each LDOS maximum in the energy domain ($Q = E/\Delta E$). The drawn curves in Fig. 5.4 show these Q factors for the three lowest-order ($n = 1,2,3$) modes of a $d = 500\,\text{nm}$, $\alpha = 10°$ groove, as in Fig. 5.2(a). Dashed lines indicate the energy at which the mode crosses the light line. For all three modes Q initially increases for increasing energy. This is attributed to the vanishing radiation damping as the plasmon becomes more confined and obtains a k_z that is progressively increasing beyond that of free-space light or planar surface plasmons, reducing the radiation loss to those channels. Q then reaches a maximum and decreases for even higher energy. This is due to increased ohmic damping at higher energy. The differences in Q between the different order modes are attributed to differences in dispersion and the corresponding differences in overlap of the mode with the metal.

In a ring resonator, Q can be determined from the width of the resonant LDOS peak as in the spectra of Fig. 5.3. These data are indicated by the squares ($m = 1$) and triangles ($m = 2$) in Fig. 5.4. Each data point corresponds to a different ring, with a radius such that it sustains an $m = 1$ or $m = 2$ resonance at that energy. The Q values for the ring resonances show a similar increasing an then decreasing

trend with energy as the linear groove, but at a lower absolute value in all cases. This is due to the fact that ring resonances have radiation damping as an extra loss channel. The difference in Q between linear grooves and ring resonances is less for the higher-order azimuthal ($m = 2$) modes. Such modes correspond do not have a dipole moment and therefore couple less to radiation.

Figure 5.5(a) shows a systematic comparison of Q values for a range of ring geometries. Q factors are plotted for the $m = 1$ resonance resulting from the lowest-order groove mode ($n = 1$). Plotted are results from rings with $\alpha = 10°$ and $d =$ 100, 500, 1000 nm (thick lines). Also plotted are results for $\alpha = 0°$, $d = 100$, 500 nm (thin lines). The figure shows that Q factors in these rings with such different shapes are almost all between 10 and 50 (corresponding to peak widths of ~ 50–100 meV). Given that the differences in groove shape span a large range for these calculations, it appears that optimization of Q/V in ring resonators is more a matter of mode volume rather than quality factor.

Mode volume of ring resonances

The effective volume of a resonant mode can be determined by performing the following integral:

$$V_{\text{eff}}(\mathbf{r}_e, \omega) = \frac{\int_V W(\mathbf{r}, \omega) d^3\mathbf{r}}{W(\mathbf{r}_e, \omega)} \tag{5.2}$$

where W is the electromagnetic energy density [161] given by $W(\mathbf{r}, \omega) = \frac{\epsilon_0}{2}\left(n^2 + \frac{2\omega n\kappa}{\Gamma}\right)|\mathbf{E}(\mathbf{r}, \omega)|^2$ using an oscillator model with damping frequency Γ for the dielectric constants. $\mathbf{r}_e$ is the position of the emitter for which the Purcell factor is to be found. The electric field $E(\mathbf{r}, \omega)$ of a resonant mode is found using BEM by calculating the induced field of a dipole radiating at the resonance energy. In this calculation, the field of the dipole itself is subtracted from the total field. The position $\mathbf{r}_e$ of the emitter is chosen to be in the center of a groove, at a depth for which the field is highest.

Figure 5.5(b) shows the calculated mode volumes for the ring resonances of the same groove geometries as in Fig. 5.5(a). Each curve represents properties of different rings, with ring radii chosen such that there is a lowest-order $m = 1$ resonance at that particular energy. The general trend of decreasing mode volume with energy is attributed to an increase in mode index with energy, which means that relatively smaller rings are needed to obtain a resonance. The increase in effective mode volume for higher energies, as is observed in the $\alpha = 0°$ and $\alpha = 10°$, $d = 100$ nm geometries, is not attributed to an increase in the absolute size of the modal field, but solely to the decrease of the wavelength to which the volumes are normalized. The figure shows that the mode volumes of rings with $\alpha = 10°$ follow a similar general trend. This is consistent with the fact that the field of the lowest-order groove mode is localized to the groove bottom and thus not very sensitive to the groove depth. The termination of some of the curves at low energies is caused by cutoff of the groove mode. For higher energies, the size of deeper grooves poses a geometrical limit to the smallest possible ring radius. The smallest mode volume

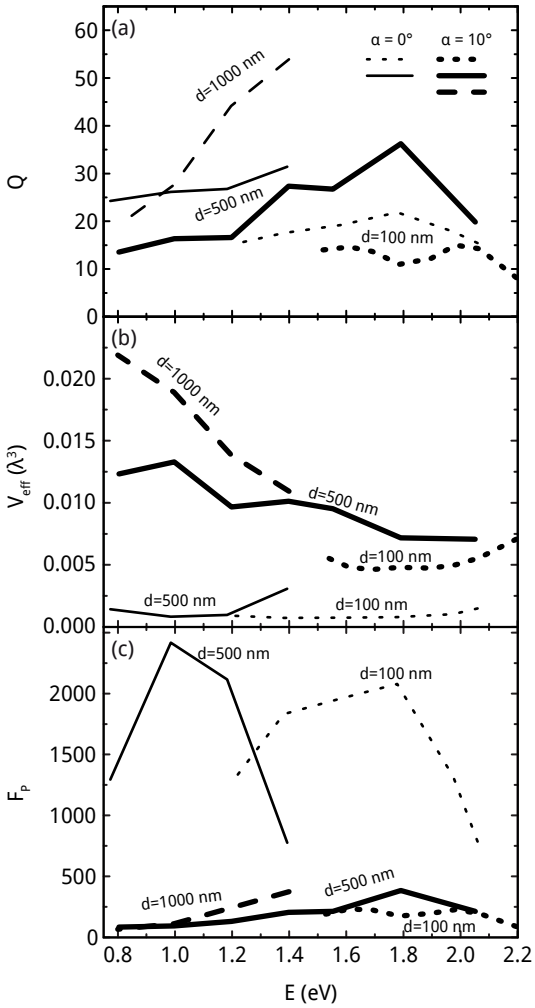

Figure 5.5: Q factors, mode volumes and Purcell factors for the $n = 1$, $m = 1$ resonance of ring resonators with $d = 100, 500, 1000$ nm, $\alpha = 10°$ (thick lines), and $\alpha = 0°$ (thin lines). **(a)** Q factor. For a large range of geometries, Q remains between 10 and 50. **(b)** Mode volumes. All mode volumes are far below the diffraction limit ($0.125\,\lambda^3$). Ring resonators with $\alpha = 0°$ (10 nm groove width) show the smallest volumes. For a $d = 100$ nm groove at 1.38 eV, the mode volume is as small as $0.00073\,\lambda_0^3$. **(c)** Purcell factors. In the lower three curves ($\alpha = 10°$), a Purcell enhancement of more than 350 is found. For the resonators based on thin grooves ($\alpha = 0°$) Purcell factors reach to over 2000.

is reached for the $\alpha = 0°$ ring resonators, with values below $0.001\,\lambda_0^3$. In the high energy spectral range, this is achieved for $d = 100$ nm grooves; for lower energies, deeper grooves are required to reach similar low mode volume. The smallest mode volume is observed for the (10 nm width) $d = 100$ nm ring at 1.38 eV. The V-groove structures with the same width and depth all show higher mode volume, indicating that lowest mode volumes are observed for closely spaced parallel sidewalls. The extremely small mode volume found here is ~180 × smaller than the diffraction limit.

Purcell factor of ring resonances

With a known Q and V, the Purcell enhancement can now be calculated from equation 5.1. The index of the medium is taken to be $n = 1$, as the field is mostly present in the void. Figure 5.5(c) shows the Purcell factors for the different ring geometries in Fig. 5.5(a) and (b). For the rings with $\alpha = 10°$, Purcell factors range to over 350 at $E = 1.4$ eV for $d = 1000$ nm and 1.8 eV for $d = 500$ nm. Indeed, such a high Purcell factor can be achieved over the broad spectral range from 1.4–1.8 eV by choosing the proper depth. The $\alpha = 0°$ (10 nm wide) geometries have Purcell factors that reach well beyond 2000 at 1.0 eV for $d = 500$ nm and 1.8 eV for $d = 100$ nm. For these narrow grooves, Purcell factors beyond 2000 can be achieved over a very broad bandwidth of 1.0–1.8 eV by tuning the ring cavity depth.

From the data in Fig. 5.5 it follows that the cavity quality factor varies by only a factor 5 (Q = 10–50) while the mode volume varies by a factor 30. As a consequence, the variations in the Purcell factor are governed by variations in mode volume rather than quality factor.

It is well known that dipole emitters spaced closely to a metal surface experience an enhanced decay rate as a result of nonresonant coupling to a continuum of surface modes [162]. For example, an emitter spaced at 5 nm from a planar Au surface experiences a decay rate that is enhanced approximately 25 times at 1.6 eV [163], mainly as a result of coupling to the so-called lossy surface waves. This effect was not taken into account in the calculations presented here. However, in the structures presented here, the nonresonant coupling is substantially smaller than the Purcell enhancement due to coupling to cavity plasmons. As a result, these nonresonant effects can be neglected.

The groove-based resonator geometry presented here is a versatile cavity that allows for large spontaneous emission enhancements over a broad spectral range, enabling experiments with a broad range of emitters (QDs, dyes, rare earth ions) incorporated in its circular void. Recent work [32] has shown that narrow (< 20 nm) grooves with depth well beyond 100 nm can be fabricated using focused-ion-beam milling, which brings ultra-high spontaneous emission enhancements within reach. Further optimization of the geometry should lead to Purcell factors even higher than those reported in the present chapter.

5.4 Conclusions

In conclusion, we have shown that the resonances of plasmonic V-groove ring resonators directly follow from the dispersion in linear V-groove plasmon waveguides. This allows for tuning of the ring cavity resonances by the ring radius. For these resonances, we have calculated the quality factor Q and mode volume V for different groove shapes and ring radii. Quality factors range from 10–50 depending on geometry; mode volumes vary by a factor 30. Smaller cavities suffer from larger radiation losses. For higher energies, cavity modes are well confined to the bottom of the groove, thus Q and V are less sensitive to depth. The smallest mode volume was found to be $0.00073\,\lambda_0^3$ for a ring based on a $\alpha = 0°$, 100-nm-deep, 10-nm-wide groove with a radius of 90 nm. In this plasmon resonator, light can be confined more than 1000 times stronger than in a photonic crystal cavity. A very high Purcell factor, $F_P > 2000$, can be achieved over a broad range of energies (1.0–1.8 eV) by choosing the proper ring geometry. For a given geometry, similar Purcell enhancement is observed over a broad spectral range ($\sim$ 50–100 meV) due to the moderate cavity Q.

This allows for control of spontaneous emission, and light-matter interaction in general [164], over broad spectral range, paving the way for plasmon enhanced lasers and broadband light sources.

6

Plasmonic whispering gallery cavities as optical nanoantennas

We study the lowest-order ($m = 0, 1, 2$) azimuthal resonant modes of surface plasmon whispering gallery cavities based on a circular groove in a Au surface. We relate the local field symmetry to coupling of the resonances to far-field radiation, optical emitters, incoming electrons or photoelectrons emitted from the surface. To do so, we combine four complementary techniques: optical scattering, fluorescence, cathodoluminescence and photoelectron emission microscopy. We exploit the field symmetries of the plasmonic whispering gallery cavity to demonstrate spectral reshaping of emitters, mode-specific angular emission patterns and a mode-selective excitation by incoming light, and we directly resolve the modal fields at high resolution. The results show that plasmonic whispering gallery resonators can be used as versatile antennas both in receiving and transmitting mode.

6.1 Introduction

Optical nanoantennas [165] provide an interface between the optical near field and far field. Optical antennas coupled to optical emitters can cause strong modification in the spontaneous emission rate [78, 82, 83, 166], polarization [80], and angular distribution of the light [71, 71, 73, 166]. Conversely, in the receiving mode,

optical nanoantennas concentrate light from far-field illumination into a small volume, enlarging the effective absorption cross section of molecules, quantum dots, or atomic emitters placed near the antenna, or concentrating energy into a small detector [88].

So far, most studies of antenna-emitter coupling have focused on single metal nanoparticles, with shapes varying from spheres [83, 167] to elongated nanorods [168, 169], and coupled nanoparticle geometries such as two coupled nanorods [170–174], or arrays of metal nanoparticles [35, 64, 72, 175, 176]. All these geometries take advantage of the fact that light is concentrated in a localized mode, with high absorption or emission cross section due to the high polarizability at the metal plasmon resonance.

Here, we introduce a ring resonator in a planar Au surface as a novel optical nanoantenna geometry that provides unique control over the near-to-far field coupling. The circular groove sustains surface plasmon resonances that are due to groove-bound surface plasmon polaritons that are confined between the two closely spaced groove sidewalls [19]. Resonances occur when the circumference of the ring equals an integer number m of plasmon wavelengths. The lowest order azimuthal resonance in these plasmonic whispering gallery cavities occurs if the ring circumference equals the plasmon wavelength λ. As we have shown previously [58], these plasmon ring cavities also support many high-order azimuthal modes for increasing diameter. In addition, for deeper grooves, higher-order radial modes (indicated by n) are observed that correspond to an increase in the number of antinodes in the radial direction of the cavity.

The large degree of control over the mode field symmetries of the plasmon whispering gallery resonators provides a unique way to control the coupling between the near and far field. In this chapter we use white-light scattering, cathodoluminescence imaging spectroscopy, fluorescence microscopy and photoelectron emission microscopy to study this behavior. We find that excitation from the far field is strongly influenced by the multipole moment of the local field, as well as by Fano interference effects. We use excitation in the near field by fast electrons to selectively excite well-defined antenna modes by tuning the position of excitation. Next, we show how near-field coupling of a fluorescent dye molecule to the cavity modes provides strong control over the fluorescence spectrum and decay rate. The angular distribution and polarization of the antenna emission is tuned by the resonant mode order. Finally, far-field excitation of these plasmonic ring cavities also gives rise to resonant photoelectron emission that is strongly correlated to the local field distribution at the antenna.

These experiments show that plasmonic whispering gallery cavities are ideal structures in which the radial and azimuthal mode symmetries of the resonant near field can be precisely tuned leading to accurate control over the coupling between near and far field. Interestingly, while the azimuthal modes are due to cavity resonance of propagating surface plasmon resonances, they can be well described by mode field symmetries of dipolar, quadrupolar and higher order localized modes.

6.2 Mode selectivity and Fano line shapes in far- eld optical excitation

Methods

Arrays of plasmonic whispering gallery resonators were fabricated using focused-ion-beam milling. The resonators consist of a circular groove milled into a smooth Au surface. A representative structure and its cross-section are shown in Figure 6.1. The V-shaped grooves are approximately 100 nm wide at the top with a depth d ranging from 25 to 500 nm. Ring radii r are in the range 100–300 nm. The substrate was obtained by thermal evaporation of a thick (3 µm) Au layer onto a freshly cleaved mica substrate. After annealing at 500° C it was glued to a silicon wafer using an epoxy resin (EPO-TEK 377), cured at 150° C, and subsequently stripped off the mica template. The resulting film has a very smooth surface composed of large (~10 µm) crystal domains. Arrays composed of multiple rings are made within a single crystal domain allowing for smooth FIB milling that does not suffer from differences in milling rate between crystal grains. A rectangular array of 20×17 rings with a 2 µm pitch was milled. At each column, the depth is increased; for each row, the radius is increased.

Cathodoluminescence (CL) measurements were taken in an FEI XL30 SEM using 30 keV electrons (see chapter 1.3 for details). Ring resonators were excited by scanning the electron beam (current ~1 nA) over a 900-nm-long line across the ring in 10-nm steps with an exposure time of 0.25 s per step. Spectra were recorded with

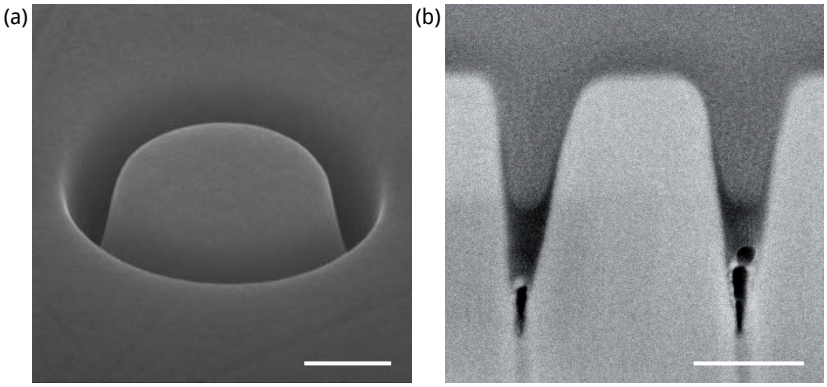

Figure 6.1: Scanning electron micrographs of plasmonic whispering gallery resonator with radius r = 300 nm and groove depth d = 500 nm. **(b)** FIB-milled cross-section through resonator infilled with a PVB polymer layer spin coated onto the sample surface from solution. It forms a thin (< 50 nm) layer onto the surface and fills the bottom part of the V-groove (dark contrast). Air inclusions are formed at the bottom of the groove. Scale bars: 200 nm

a liquid-nitrogen-cooled CCD array detector. Spectra taken along a single line scan were summed to yield an integrated spectrum of the resonator.

White-light scattering measurements were taken using a 60× NA=0.9 objective which focused white light from an incandescent lamp source onto the sample surface. Scattered light was collected by the same objective and, using a beam splitter, projected onto a 9 µm core diameter fiber guiding the light into a thermoelectrically-cooled CCD array detector. Using a piezoelectrically controlled stage, the array of rings was scanned through the focus in 200-nm steps. From this scan, the scattering spectra of the individual rings were taken by summing over nine pixels covering a single resonator. Spectra were divided by the scattering spectrum of unstructured Au.

Results and discussion

Ring resonances can both be excited by an incoming plane wave and by an incoming electron beam; however the mechanisms of excitation are different. We compare the scattering spectrum with the CL emission spectrum and use the differences between these spectra to study the mode symmetries.

Figure 6.2 shows the scattering and CL spectra of three representative rings with radii of 100, 210 and 290 nm and a depth of approximately 100 nm. For the smallest ring with a 100-nm radius, the CL spectrum (black curve) shows one clear peak. In contrast, the white-light scattering spectrum for this ring (red curve) is featureless. As known from previous work (see chapter 4) the CL emission peak for a small ring of 100-nm radius is caused by a resonance with an $m = 0$, $n = 1$ symmetry, which corresponds to a charge distribution that is symmetric around the ring; the modal charge distribution has a vertical dipole moment. Such resonances are efficiently excited by an electron beam incident from the top, parallel to the dipole moment [120], in agreement with the clear emission peak observed in the CL spectrum. Light that is incident through an objective, on the other hand, offers an electric field that is mostly polarized in the sample plane and thus perpendicular to the resonator modal field. This explains why the excitation is not visible in the scattering spectrum.

For the second ring ($r = 210$ nm), the $m = 0$ peak has shifted to a longer wavelength outside the measurement range and another peak is clearly visible at 675 nm in the CL spectrum. At this wavelength, the white-light scattering spectrum shows a dip. This corresponds to the excitation of an $m = 1$ resonance that has a dipolar charge distribution in the plane of the ring resonator. Both the incoming electron and a plane wave couple to this resonance. Although the resonant dipole moment is perpendicular to the electron beam, the modal electric field vector has vertical components in significant parts of the resonator groove [19] resulting in excitation of the resonance (see also section 6.4).

The CL spectrum of the largest ring ($r = 290$ nm) shows two peaks. Here, the scattering spectrum only shows a feature at the wavelength of the rightmost peak. This peak at 780 nm corresponds to the $m = 1$ mode [19] also observed in the $r =$

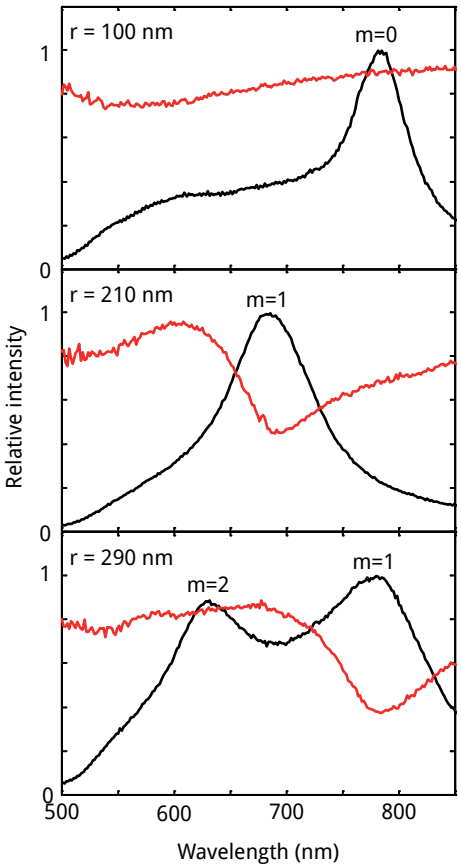

Figure 6.2: White-light scattering spectra (red curves) and 30 keV cathodoluminescence spectra (black curves) of ring resonators with increasing radius r. Resonances give rise to peaks in the cathodoluminescence spectra and Fano-type line shapes in the scattering spectra. All optical resonances ($m = 0, 1, 2$) are excited by the electron beam, but only dipolar ($m = 1$) resonances are excited in the white-light scattering experiment.

210 nm ring, now shifted to a longer wavelength due to the increased size of the resonator. The peak at 625 nm corresponds to an $m = 2$ resonance, with a quadrupolar charge distribution. As with the dipolar $m = 1$ mode, this quadrupole mode is efficiently excited by the electron beam at positions where its near field has a large vertical component. Quadrupolar charge distributions are often disregarded when considering far-field radiation. This is valid when the oscillating charges are confined in a deep subwavelength volume. Here, however, the charges are distributed over wavelength-scale dimensions of the whispering gallery cavity and far-field emission is indeed observed under electron excitation. In contrast, such a quadrupolar oscillation does not couple to a plane wave incident from the top, for symmetry reasons analogous to the $m = 0$ case. Indeed, there is no signature of the $m = 2$ resonance in the scattering spectrum.

In the comparison between CL and scattering, another interesting feature is observed. The peaks in the CL spectra have an apparent Lorentzian line shape, as is expected for this resonant behavior, whereas the dips in the white-light scattering spectra are asymmetric. This difference is attributed to interference between directly reflected light and radiation by the resonant mode. At an excitation wavelength below resonance, the resonator oscillates out of phase (phase shift is close to π) with the driving field, i.e. the incident light. The incident light itself undergoes a phase shift of $\sim\pi$ upon direct reflection off the substrate. These effects combined cause constructive interference of the two light paths, leading to an enhanced scattering signal at wavelengths shorter than the resonance wavelength. Above the resonance wavelength, the phase shift upon reflection remains π, however, the resonator now oscillates in phase with the driving field, leading to destructive interference between directly reflected light and light that is coupled out of the resonator. Indeed, at longer wavelengths a decreased scattering intensity is observed. This Fano-type interference [177] between a continuum and a single resonance that leads to this line shape is a well-known phenomenon in plasmonic resonances [178].

6.3 Spectral reshaping of uorescence by coupling to antenna resonances

An advantage of the plasmonic ring resonator geometry is that the resonant field is strongly enhanced over a relatively large modal volume that is easily addressed from the outside. Here we study how the fluorescence of dye molecules incorporated inside the groove is affected by coupling to plasmonic ring modes.

Methods

Ring cavities were coated by a polymer layer that was doped with ATTO680 dye molecules. The layer was obtained by spin coating a solution of $3 \cdot 10^{-5}$ M dye and 5 wt% poly-vinyl butyral (PVB) in ethyl-lactate onto the Au substrate [82]. The

resulting layer thickness is 10–50 nm as can be seen in Fig. 6.1(b). The bottom half of the groove void of the plasmon cavities is infilled with PVB with the exception of small air inclusions at the bottom.

Scanning confocal optical microscopy was performed using the same setup as in the scattering experiments. A 5 mW diode laser emitting at 640 nm was used as an excitation source and filtered through a 650 nm short-pass filter; in the detection path a 700 nm long-pass filter was used.

Results and discussion

As a result of infilling the groove void with a polymer layer, the resonances undergo a red shift [139]. Figure 6.3 shows white-light scattering and CL emission spectra of an $r = 200$ nm, $d = 600$ nm ring. Before infilling, the ring resonance is at 700 nm, as can be seen in the CL spectrum (black). The scattering spectrum (red) shows a dip around this wavelength due to coupling of the incident light to the $m = 1$ resonance. After infilling, the scattering measurement shows a dip at 750 nm (blue curve), showing that the resonance has indeed shifted to a longer wavelength. A change in the shape of the scattering spectrum is observed upon infilling, which is attributed to a change in the interference conditions due to the presence of the PVB layer on the Au surface. The observed red shift is smaller than what would be ex-

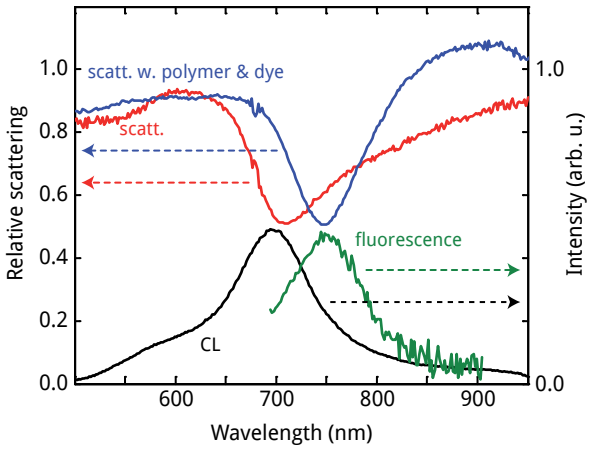

Figure 6.3: Resonance spectra of a single ring resonator ($r = 175$ nm, $d = 50$ nm) before and after infilling with dye-containing polymer. Black curve: cathodoluminescence spectrum, showing a clear resonant peak. Red curve: normalized white-light reflection spectrum showing a Fano line shape at the resonance wavelength. As a result of a polymer layer covering the resonator the white-light reflection spectrum red shifts (blue curve). Green curve: fluorescence enhancement of dye molecules incorporated in the polymer layer, showing a spectral reshaping due to coupling to the cavity mode.

pected assuming full infiltration of the V-groove with the polymer ($n_{\text{polymer}} = 1.49$). We attribute this to the presence of air voids at the bottom of the groove, which effectively lower the index and the fact that a significant fraction of the resonant field extends above the polymer film.

The ATTO680 fluorescent dye used in these experiments has a quantum efficiency of ~30% with a broad luminescence above 700 nm and a maximum absorption at 680 nm. Figure 6.4 shows the emission spectrum (labeled reference) of ATTO680 molecules embedded in a 10-nm layer of PVB on a flat Au substrate. The spectrum recorded from ATTO680 dye molecules inside the $r = 175$ nm, $d = 50$ nm ring cavity (same as Fig. 6.3) is also shown in Fig. 6.4. This spectrum is clearly different from the reference and shows a strong enhancement of the fluorescence in the central part of the spectrum. The fluorescence enhancement spectrum, obtained by division of the cavity spectrum by the reference, is also plotted in Fig. 6.4. We observe an enhancement of the fluorescence over a broad range around 750 nm. The fluorescence enhancement at 750 nm is more than 5 times higher than at the edges of the spectrum, suggesting an enhancement of the radiative rate at this wavelength that is at least a factor 5. The fluorescence enhancement spectrum is also plotted in Fig 6.3. Clearly, the fluorescence is enhanced right at the cavity resonance.

Taking advantage of the large tunability of plasmon cavity resonance, we now make a systematic comparison of the fluorescence enhancement for different cavity geometries. Figure 6.5 shows a confocal microscopy scan of an array of resonators with different depth and diameter. In the confocal scan, the fluorescence

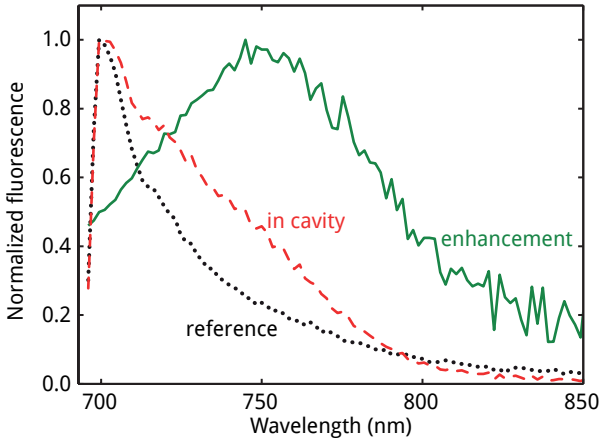

Figure 6.4: Normalized fluorescence spectrum of ATTO 680 dye embedded in PVB inside an $r = 175$ nm, $d = 50$ nm plasmon ring cavity. A reference spectrum from dye in a 10 nm polymer layer on unstructured Au is also shown. The fluorescence enhancement in the ring resonator is shown by the green curve. ($\lambda_{\text{pump}} = 640$ nm)

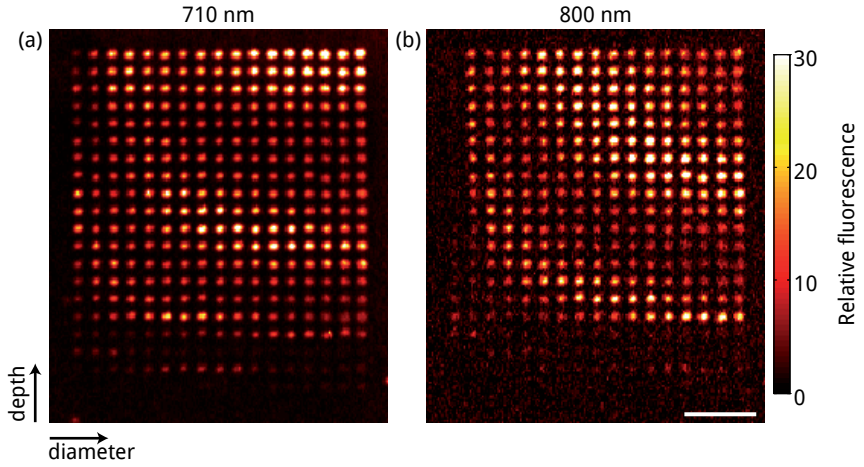

Figure 6.5: Confocal microscopy scan of ATTO680 fluorescence in an array of 17 × 20 ring resonators. The rings have groove depths ranging from 25 nm (bottom) to 500 nm (top) and radii of 100 nm (right) to 300 nm (left). Excitation was at 640 nm. Plotted in these scans is the fluorescence in a 10-nm band around **(a)** 710 nm and **(b)** 800 nm, showing that the emission is enhanced for certain rings at specific wavelengths at which the plasmonic cavity is resonant. Data are normalized to fluorescence of the planar part of the Au substrate. Scale bar: 10 µm

spectrum was recorded for every pixel in a rectangular grid. In this figure, only the emission at 710 nm and 800 nm is shown (spectral bandwidth 10 nm). Each bright dot in the figure corresponds to an individual ring resonator. Data are normalized to the fluorescence from a planar part of the substrate. The resonators have a diameter that increases from left to right; the groove depth increases from bottom to top. Clearly, the fluorescence enhancement strongly depends on cavity geometry. The bright resonators appear as bands in the image. This is due to the fact that different combinations of depth and diameter yield the same resonant wavelength. The figure clearly shows that the fluorescence is enhanced in ring resonators over a broad range of cavity sizes and shapes, due to their cavity resonance. These bands are both observed at 710 and 800 nm but at different cavity geometries. Exploiting the tunability of the ring resonances, the fluorescence enhancement can be engineered throughout the entire emission band of the ATTO680 molecules. Comparison of the data in Fig. 6.5 with white-light scattering data (not shown) shows that the bright fluorescence bands correspond to resonances with $m = 1$ and $n = 1, 2, 3...$, that all have a dipolar character. Most cavities in the array have depth $d > 100$ nm. In these deep structures, the resonance spectrum is dominated by several higher-order n-modes. These modes efficiently couple to free-space light. However, their fluorescence might obscure effects due to $m = 2$ resonances, which should also lead to fluorescence enhancement.

Finally, we note that resonance effects near the 640-nm laser excitation wave-

length do not play a role in the intensity enhancements observed.

6.4 Spatially resolved excitation and angle-resolved emission of antenna resonances

The experiments above show clear signatures of different multipolar field symmetries. In this section, we use electron beam excitation to directly resolve these modes and study their angle-resolved emission pattern.

Methods

Due to the rotational symmetry of the ring resonators, the different multipolar fields are twofold degenerate. This degeneracy can be lifted by analyzing the CL emitted from the resonator through a polarizing plate. The CL setup (see Fig. 1.4) allows for the placement of a polarizer in the part of the beam that emerges from the parabolic mirror. As the mirror alters the polarization distribution from the sample, light is collected through a vertical slit in the center of the beam (see Fig. 1.6). When analyzing this light with a polarizer, a single polarization emitted from the mirror focus is selected. In these experiments, a 0.9-mm-wide slit was used (less than 1/20 of the beam width) and the polarizer was set to either horizontal or vertical orientation. In polarized-emission experiments the electron beam was scanned in a rectangular grid of 10-nm steps using a 0.1 s exposure time per pixel. For every pixel, a spectrum was acquired.

Angle-resolved measurements were taken without the slit, collecting light from the full area of the mirror, while the electron beam was fixed to one position on the resonator. The resonant mode was selected using band-pass filters with a 40-nm-bandwidth around the wavelength of interest. Data is collected by a CCD array detector placed in the parallel beam that leaves the parabolic mirror. In this beam, every position corresponds to a unique emission angle. The CCD data was converted to an angular distribution. The exposure time was 6 s.

Results and discussion

Figure 6.6(d-o) shows CL data taken from two different ring resonators with r = 120 nm (Fig. 6.6(a)) and r = 300 nm (Fig. 6.6(b,c)). The groove depth was d = 100 nm in both cases. The left column shows CL data for the m = 0 resonance of the small ring at 750 nm. For this resonance the phase is constant throughout the groove and the dipole moment is oriented perpendicular to the sample surface. The center and right columns show CL data for the m = 1 resonance at 770 nm and the m = 2 resonance at 630 nm for a larger ring, that correspond to one or two plasmon wavelengths fitting in the ring circumference, respectively.

Figures 6.6(d-f) show spatially-dependent cathodoluminescence excitation maps for the $m = 0, 1, 2$ resonances. The data in Fig. 6.6(d) is taken at the peak

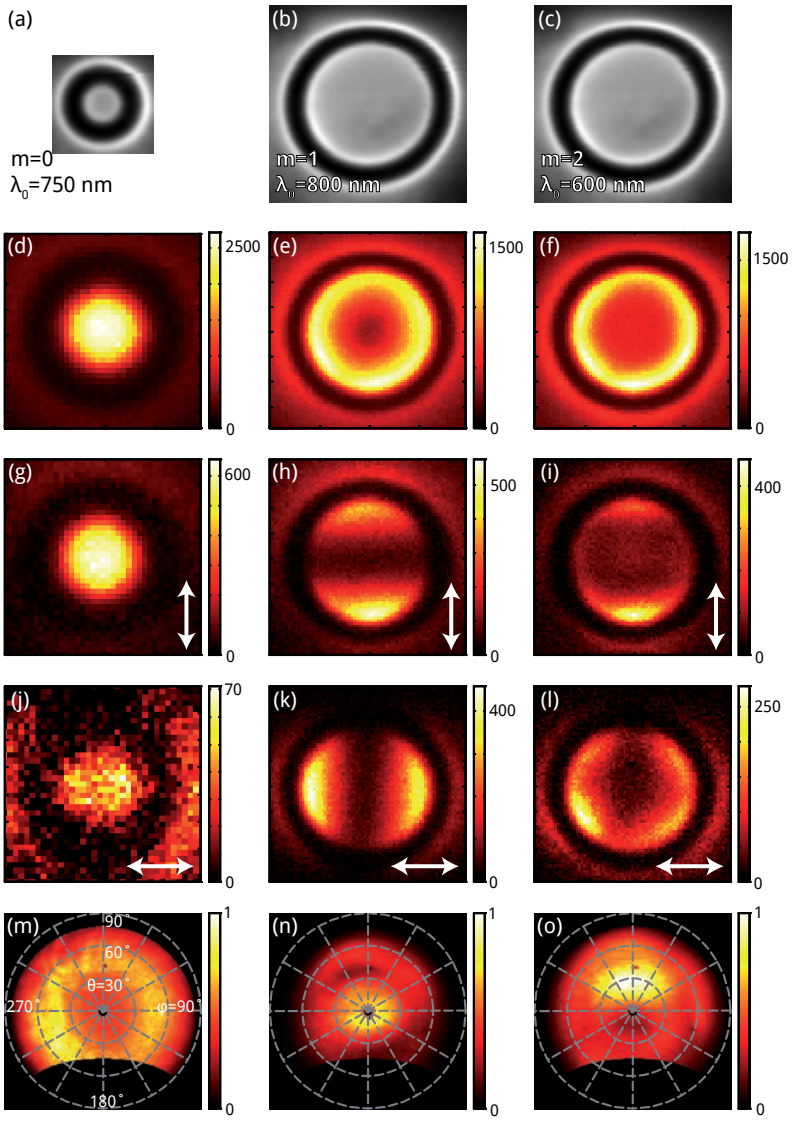

Figure 6.6: Spatially-resolved excitation and angle-resolved emission of $m = 0, 1, 2$ resonances in plasmonic whispering gallery resonators. Left column: $m = 0$; data for an $r = 120$ nm ring resonator at a wavelength of 750 nm. Image size: 400 × 400 nm^2. Center column: $m = 1$; data for an $r = 200$ nm ring resonator at 800 nm wavelength. Image size: 800 × 800 nm^2. Right column: $m = 2$; data for the same $r = 200$ nm ring resonator at 600 nm wavelength, with the same image size. First row: Scanning electron micrographs. Second row to fourth row: e-beam excitation maps (30 keV e^-), acquired using unpolarized detection, vertical polarization and horizontal polarization, respectively. Color scales indicate CCD counts. The arrows indicate the orientation of the polarizer. Fifth row: angle-resolved emission of the resonant mode for excitation in the center of the resonator **(m)** and excitation at the bottom edge of the center plateau of the resonator **(n)** and **(o)**.

resonant wavelength of 750 nm. Data for the $m = 1$ and 2 resonances in Figs. 6.6(e,f) is taken at $\lambda_0 = 600$ and 800 nm, respectively, to avoid overlap between the resonant peaks. Data taken with unpolarized detection (second row) shows circular features for all resonances, which is expected for a rotationally symmetric structure with accordingly degenerate modes. Interestingly, the $m = 0$ resonance in Fig. 6.6(d) is mostly excited at the center of the ring. This is in agreement with the $m = 0$ mode symmetry and a vertical dipole moment, which is efficiently excited in the center of the structure. The $m = 1,2$ resonances in (e) and (f) are best excited at the edges of the center plateau because the resonant field for these modes is strongest inside the groove. The strongest excitation is observed on the inner edges of the groove, as here the out-of-plane component of the modal field, which couples efficiently with the field of the electron beam, has a maximum [19].

The third row of Fig. 6.6 shows CL scans acquired through a slit with a polarizer transmitting vertically polarized light. The $m = 0$ dipole mode is expected to emit a rotationally symmetric radiation pattern with a polarization that is perpendicular to the sample surface. This emission is readily transmitted through the polarizer. Indeed, the excitation map Fig. 6.6(g) at 750 nm is very similar to the unpolarized case, consistent with the dipole moment being vertical to the sample surface. The data for the $m = 1$ resonance in Fig. 6.6(h), also taken through the polarizer is very different. Here the rotational symmetry is lost and two lobes are clearly visible. This behavior is attributed to an in-plane dipole moment of which we only detect the far-field radiation through the polarizer if it is excited with the matching polarization. The vertical polarization is only excited when the electron beam dwells near the top or the bottom of the resonator in the image of Fig. 6.6(b), where the maxima in the CL image of Fig. 6.6(h) are observed. The data for the $m = 2$ resonance in Fig. 6.6(i) are more complex; the image shows that this mode is mostly excited near the top and the bottom but there is a nonzero excitation around the full circumference of the ring. The excitation map for a quadrupolar resonance is indeed expected to be more complex than that of a dipole; we will clarify this result later. The intensity in the center of Fig. 6.6(i) is attributed to an $m = 0, n = 2$ resonance that overlaps with the signal at 600 nm [19].

The excitation maps collected through the vertical slit drastically change when the polarizer is rotated to a horizontal orientation (fourth row). The $m = 0$ dipole mode does not emit the corresponding polarization and indeed, the signal in Fig. 6.6(j) is very low. The small intensity that is transmitted is attributed to a dipolar mode also present in this structure with its maximum at a much shorter wavelength. In Fig. 6.6(k), the dipolar pattern of the $m = 1$ image now has the high-intensity lobes on the left and the right of the image, as is expected. The quadrupolar $m = 2$ mode (Fig. 6.6(l)) shows four clear lobes with maxima that are rotated by 45° with respect to the vertical-polarization-scan.

Angle-resolved measurements without polarizer were taken to verify the conclusions made about the dipole orientations of the $m = 0$ and $m = 1$ resonances as well as to clarify the patterns observed for the quadrupolar $m = 2$ resonance. The fifth row of Fig. 6.6 shows the angular emission patterns for a half sphere covering

the ring resonator; azimuthal angle φ and polar angle θ are indicated. The black area in the bottom of each image corresponds to the open part of the parabolic mirror, where no light is collected. The orientation of the angular plots corresponds to that of the excitation maps. Figure 6.6(m) shows the emission owing to excitation of the $m = 0$ resonance on the center plateau. A bright ring is observed, indicating azimuthally symmetric emission into all directions. The polar angle of maximum intensity is around 45°. This angular emission pattern is in agreement with what is expected for a vertical dipole ($\lambda = 750$ nm) oscillating at the Au-air interface and is similar to the angular distribution of transition radiation [107]. Figure 6.6(n) shows the angular distribution for the $m = 1$ dipole emission. Here the beam was placed at the bottom edge of the center plateau (position of maximum intensity in (h)). For a dipole oriented parallel to the sample surface and vertically in these figures, a horizontal emission band is expected through the center of the angular plot, but due to the presence of the Au surface, this band should be truncated at shallow angle, resulting in emission that is mostly upward. The figure indeed shows maximum intensity in the center of the distribution, corresponding to upward emission. The upward emission is always transmitted by the slit used for polarized measurements, independent of the orientation of the $m = 1$ dipole mode. This is in agreement with the fact that the signal intensities in Fig. 6.6(h) and 6.6(k) are comparable.

Figure 6.7 shows the angular emission pattern of the $m = 1$ resonance for several electron beam positions around the ring circumference. The center image shows the excitation map of the resonator at 800 nm for a coarse scan of the electron beam. For each pixel, the angular emission was recorded and the pixel intensity represents the integrated angular emission. The angular emission patterns are plotted for 8 selected pixels on the ring circumference. The results confirm that the observation of upwards emission from the $m = 1$ mode is a consistent effect that is independent of electron beam position.

The emission pattern of the $m = 2$ quadrupole mode (also excited at the bottom of the ring) is given in Fig. 6.6(o). A bright spot is emitted at ~30° from the normal in a direction opposite the electron beam position. The signal has a minimum at the center of the plot, and a higher intensity towards the bottom. This emission pattern, having a node in the center, reminds of the pattern of a linear quadrupole with a vertical orientation [136, 179]. For a vertically oriented linear quadrupole the emitted polarization is also vertical. By comparing excitation maps Fig. 6.6(i,l) it is found that for excitation at the bottom edge of the center plateau the emission indeed has a predominantly vertical polarization, in agreement with the linear quadrupole picture. However, the asymmetry in Fig. 6.6(o) between top and bottom shows that not only a pure quadrupole is excited. We attribute these effects to a complex interplay between the quadrupole mode and the dipolar mode which is also weakly excited at 800 nm. Further study is required to fully explain the observed angular emission pattern. It is interesting to note that the asymmetry does not arise in the $m = 1$ dipolar emission pattern.

For the $m = 2$ resonance, Fig. 6.8 shows the angular emission at 600 nm for different excitation positions, analogous to the $m = 1$ resonance patterns in Fig. 6.7.

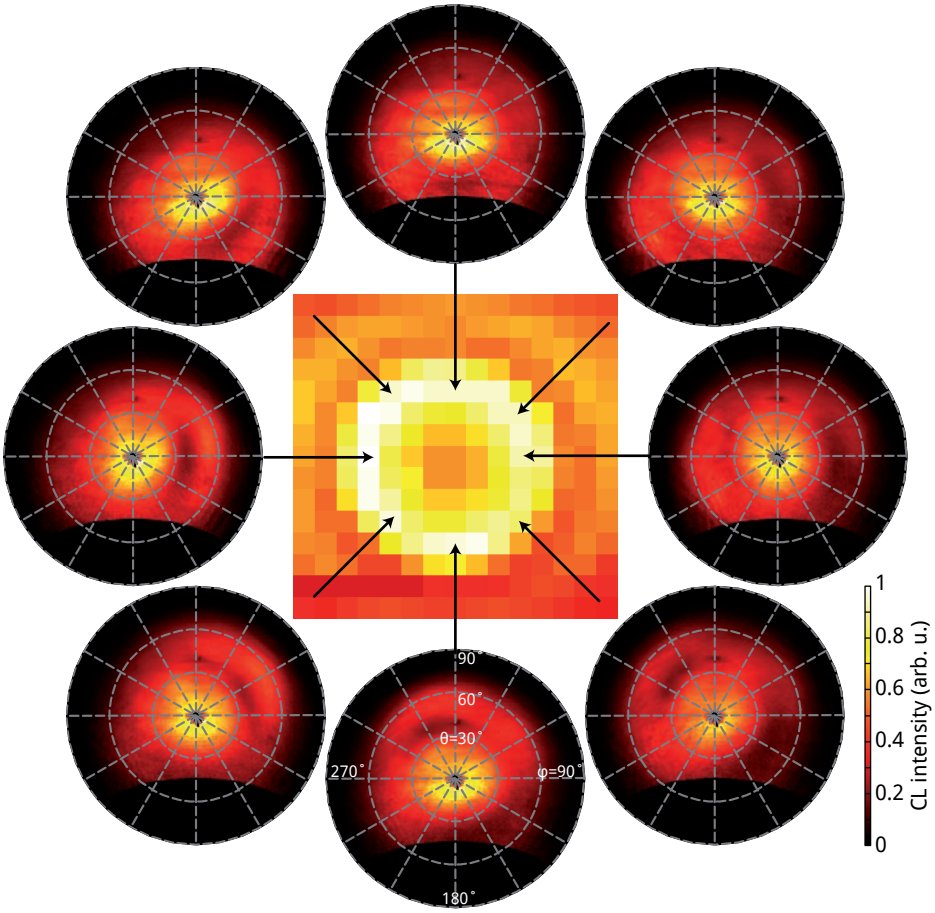

Figure 6.7: Angle-resolved emission from the $m = 1$ dipolar mode of an $r = 300$ nm, $d = 100$ nm ring resonator. Center: excitation map at 800 nm of the dipolar plasmon mode. For selected pixels on the inner edge of the center plateau, the angular emission pattern is plotted. The figure shows that the dipolar resonance always radiates towards the surface normal, independent of electron beam position.

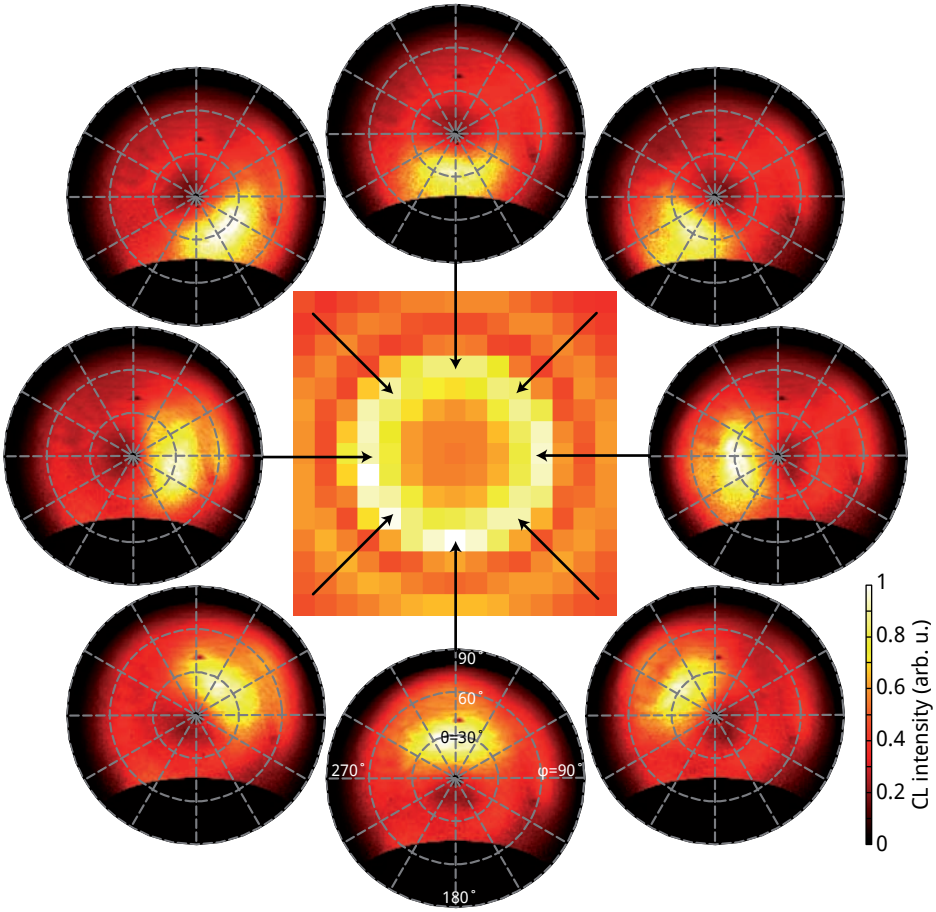

Figure 6.8: Angle-resolved emission from the $m = 2$ quadrupolar mode of an $r = 300$ nm, $d = 100$ nm ring resonator. Center: excitation map at 600 nm. For selected pixels on the inner edge of the center plateau, the angular emission pattern is plotted, showing a maximum in emission that is 30° from the normal and pointing in a direction opposite the electron beam position.

Clearly, the angular emission pattern is rotated for different excitation positions along the edge of the center plateau. The bright emission spot at 30° from the normal always points to the direction opposite the electron beam position, confirming that the electron beam position determines the local field symmetries.

Using the angular emission data, the patterns observed in the excitation maps of Fig. 6.6 can now be fully explained. In Fig. 6.6(i) the emission maximum only falls on the slit when the electron beam is positioned at the top or bottom of the ring, hence the two maxima. The upper maximum has a lower intensity, which is because the emission partly falls outside of the mirror acceptance angles. In Fig. 6.6(l), there is only a horizontal polarization component in the emission when the electron beam dwells at the left or right, but in this case the emission falls completely outside of the slit. At positions between top, bottom, left and right, a small fraction will fall on the slit with a small horizontal component. Here, four maxima appear. Clearly, when considering the angular emission pattern and the acceptance range of the slit, the polarized experiment provides us with a method to distinguish between mode orders.

The results show that although the same mode is excited at different positions in the resonator, its polarization and far-field emission patterns are very position-dependent. By choosing mode order and excitation position, the far-field emission and polarization of a ring antenna can be fully engineered. This implies that despite their spherical symmetry, plasmonic whispering gallery cavities can be employed to beam emission from light sources embedded in the cavity to non-zero angles.

6.5 Photoelectron emission due to antenna resonances

As we have seen above, the electromagnetic field of a ring resonance couples to free space light, incoming electrons and fluorescent molecules. In the remainder of this chapter, we exploit the use of one other coupling mechanism to study the antenna properties of plasmonic whispering gallery resonators.

Photoelectron emission occurs when a photon transfers enough energy to an electron to raise its energy from the Fermi level to a free state. The photoelectric effect also occurs as a multiple-photon process. In this case, the probability for photoemission depends nonlinearly on intensity. Photoelectron emission microscopy (PEEM) is a technique in which electrons emitted from a sample are accelerated and imaged onto a screen using an electrostatic lens system [180, 181]. Due to the high quality of electron imaging systems, PEEM enables the study of optical fields at subwavelength resolution. As was recently found, PEEM can be used to study propagation and dephasing of plasmons on metal particles [182], exploiting the high local field of surface plasmons for photoelectron emission.

Here, we use PEEM as a direct high-resolution probe of the electric field in plasmonic ring resonators that are excited by an incoming light pulse.

Methods

An array of ring resonators consisting of 10 columns (nominal groove depth: 60–150 nm) × 11 rows (radius: 100–350 nm) was fabricated using focused-ion-beam milling in an Au surface obtained using template stripping off a mica substrate. The sample was inserted into the PEEM system, where it was excited using a Ti-sapphire laser having linearly polarized 30 fs pulses of 800 nm that were directed onto the sample under an angle of 65° to the normal. Emitted photoelectrons were collected by an electrostatic lens system using a 10 kV extraction voltage and imaged onto a P46 scintillator screen. A sensitive CCD array detector records images of the screen. An integration time of a few seconds was used for acquisition of an image.

Results and discussion

Photoelectron emission at 800 nm on a Au surface involves the simultaneous absorption of 3 photons, making it highly nonlinear. The PEEM pictures are therefore expected to show a strong dependence on local field in the ring cavity. Figure 6.9 shows a PEEM image of the ring array. Bright pixels in this image correspond to areas from which a high number of electrons was emitted. The rectangular array of ring resonators is clearly visible: every bright spot corresponds to an individual resonator structure. The image shows two bands of resonators that show a high emission intensity; other resonators remain dark. Clearly, the photoelectron emission due to ring resonators is subject to resonant effects. The enhanced photoelectron emission in these bands is attributed to the fact that these cavities are resonant with the 800 nm excitation light ($m = 1, n = 1,2$ mode).

A CL experiment was done to verify this hypothesis. Figure 6.9(d) shows the emission at 800 nm as function of beam position on the same resonator array as

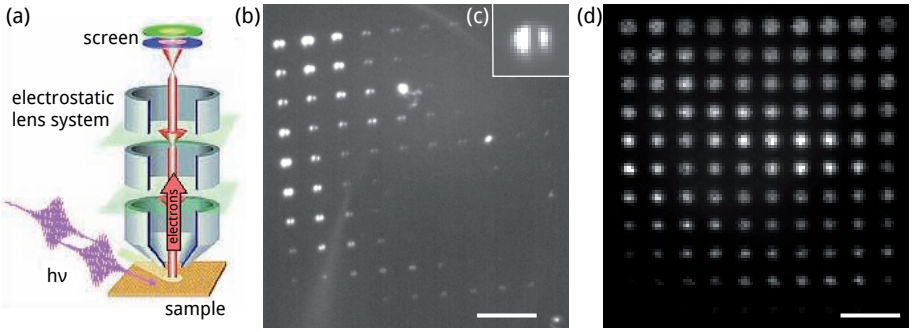

Figure 6.9: **(a)** Schematic of photoemission electron-microscopy (PEEM) setup **(b)** PEEM image of ring resonator array using excitation with 30-fs-pulses at 800 nm **(c)** Magnified PEEM image from a resonant ring, showing intensity enhanced on two lobes on either side of the resonator. **(d)** Cathodoluminescence excitation map at 800 nm. Scale bars: 4 µm

used in the PEEM experiments. Here too, two bands are observed due to ring resonances. The bands have a similar position as the bands in the PEEM figure, suggesting they correspond to the same resonance.

Since PEEM has a high spatial resolution, it is possible to accurately image the field intensity in a resonator. The inset Fig. 6.9(c) shows a magnified image of a single $r = 275\,\text{nm}$, $d = 60\,\text{nm}$ ring. Here, two lobes are seen, corresponding to a dipolar excitation pattern similar to what is observed in Fig. 6.6(h) and (k). The degeneracy of the ring resonance is lifted by the polarization of the excitation pulse. The two lobes on either side of the center plateau correspond to regions of high electric field. Close inspection of the PEEM data shows that all ring resonators have a dipolar pattern ($m = 1$). As we have previously seen, free space light only excites the dipolar resonances and no enhanced photoelectron emission due to other field symmetries is expected.

The results show that ring resonators function as an effective receiving antenna, providing a mechanism for photoelectron emission from a Au surface. PEEM can be used to measure the intensity distribution around the structure with high resolution. The next step is to exploit the high time resolution of the PEEM technique to study the time evolution of the excited plasmon modes.

6.6 Conclusions

We have demonstrated that plasmonic whispering gallery resonators are effective optical antennas both in the receiving and transmitting modes. By exploiting complementary excitation and detection techniques we fully resolve the resonant modes, their spatial distribution and emission polarization. We have shown how far-field excitation selectively excites dipolar resonances leading to a Fano line shape in the scattering spectrum. In contrast, electron-beam excitation leads to $m = 0, 1, 2$ dipolar and quadrupolar modes that can be selectively excited. Molecular fluorescence is strongly reshaped due to coupling of optically excited dye molecules to the cavity resonance. Near-field excitation by fast electrons allows us to choose the orientation of the multipolar resonance by accurately positioning the electron beam. We detect the corresponding angular emission distribution in the far field. Finally, far-field excitation of the cavity resonances gives rise to photoelectron emission due to high field confinement in the groove of the ring resonator. Imaging the photoelectron emission provides one with an additional method to directly resolve the nanoscale dipolar field distribution.

The resonance tunability and control over the mode structure offered by plasmonic whispering gallery resonators offers many possibilities for their use as optical antennas both in the receiving and transmitting mode.

7

A metal-insulator-metal waveguide at cutoff as effective $n = 0$ material

The spatial advance of the phase of light is controlled by the refractive index, essential to many if not all optical applications. Surface plasmons enable a strong modification of the dispersion of light, allowing to tailor effective refractive indices that are very large [38] or even negative [41, 43]. A special case occurs when the refractive index reaches a value close to 0 [183]. This condition can be met in waveguides near cutoff, which was experimentally demonstrated in the microwave regime [184] and was also predicted for plasmonic waveguides [185]. So far, it was impossible to reach this condition at visible wavelengths due to limitations in nanofabrication and the difficulty of probing the $n = 0$ condition in a buried waveguide. Here, we present a metal-insulator-metal plasmon waveguide that shows an effective $n = 0$ at cutoff. Waveguides with accurately controlled dimensions were fabricated using a sequence of steps including focused-ion-beam milling. Modes of the waveguides were excited using a 30 keV electron beam penetrating through the layer stack. We directly observe the spatial mode profiles and determine the dispersion relation of plasmon modes near cutoff. A group velocity as low as 0.21 c was found. At cutoff, the $n = 0$ condition was observed causing an enhanced density of optical states and a line dipole angular emission pattern.

7.1 Introduction

Optical waveguides are essential components in many modern applications. Guiding light through refractive index contrast, waveguides are used in optical fibers for telecommunication, lasers and optical integrated circuits. A special type of waveguide is based on surface plasmons, electromagnetic waves that are bound at the interface between a metal and a dielectric. The high field confinement and small lateral extent offered by surface plasmon waves enable shrinking optical integrated circuits to deep-subwavelength dimensions. This brings together optical and electronic functionality on a chip, and has lead to the realization of ultrasmall lasers [186, 187]. The dispersion of guided modes in a plasmonic waveguide strongly depends on the geometry. For example, plasmons in a metal-insulator-metal waveguide are squeezed to a small mode area when the insulator thickness is decreased, enabling high mode indices at frequencies below the surface plasmon resonance [37, 38], and a negative refractive index for frequencies above it [41, 43]. The dispersion of an MIM mode can be further controlled by limiting the lateral extent, e.g. in a rectangular waveguide geometry. Below a certain size, the waveguide modes will experience cutoff: below a certain cutoff frequency the mode ceases to exist. For frequencies approaching cutoff, the group velocity strongly decreases and the phase velocity increases. At cutoff, the phase velocity diverges, effectively corresponding to $n = 0$, i.e. the phase of light is constant throughout the waveguide. Many cases of extraordinary optical transmission [31, 188–190], strong field enhancement [70], enhanced interactions with emitters [79] and enhanced nonlinear effects [68] that have been observed in metal hole arrays are attributed to cutoff. These examples all feature waveguides that are shorter than the plasmon wavelength. Here, we investigate several fascinating physical effects that occur near cutoff in MIM waveguides that are much longer than the wavelength, allowing to study the transition between propagating modes and the resonance at cutoff. Achieving $n = 0$ in optical waveguide circuits offers many interesting applications in optical circuits, because it offers full control over the phase advance of light. So far, it has been difficult to study the propagation of light in rectangular plasmonic waveguides, because of their inherently closed nature: light is confined within the metallic boundaries, and cannot be easily addressed from the outside.

Here, we introduce the use of a 30 keV electron beam as a point source of surface plasmons to selectively excite the mode structure of waveguides consisting of metal-insulator-metal layers. The electron beam has a waist of less than 10 nm, enabling direct mapping of the plasmon mode field distribution with nanoscale resolution. We detect the far-field radiation pattern emitted from the waveguides using a piezoelectrically positioned parabolic mirror assembly in combination with an imaging CCD system. We spatially resolve the waveguide modes and determine the full dispersion near cutoff.

An impinging electron that makes the transition between two materials with different dielectric constants gives rise to an excitation that is similar to a radiating dipole. As a result of this excitation, free space light is emitted (transition radi-

ation) and surface plasmons are excited [107, 109]. The excitation probability of a plasmon by an impinging electron is proportional to the local density of states (LDOS) at the position of electron beam impact [109]. The probability with which plasmons are excited is therefore strongly connected to local resonances and their nanoscale field distribution. Furthermore, electron-beam excitation is particularly suited to generate the lowest-order MIM slot waveguide mode, because it has a symmetric field distribution: this modal field shows good overlap with the exciting field of the electron beam [119, 120, 191]. The cathodoluminescence (CL) radiation collected in the experiment provides a powerful means to resolve the dispersion in MIM waveguides.

7.2 Results

Figure 7.1 shows scanning electron micrographs of an 85-nm-thick dielectric layer composed of an SiO_x core that is fully surrounded by a Ag cladding. The structure is fabricated using a sequence of evaporation, sputtering and focused-ion-beam milling. An array of such waveguides was fabricated with a core width ranging from 100 to 600 nm and a length of 2 µm. The Ag cladding is covered by a 10 nm Cr layer, both on top and bottom, in order to absorb plasmon modes of which the field is predominantly at interfaces outside the core.

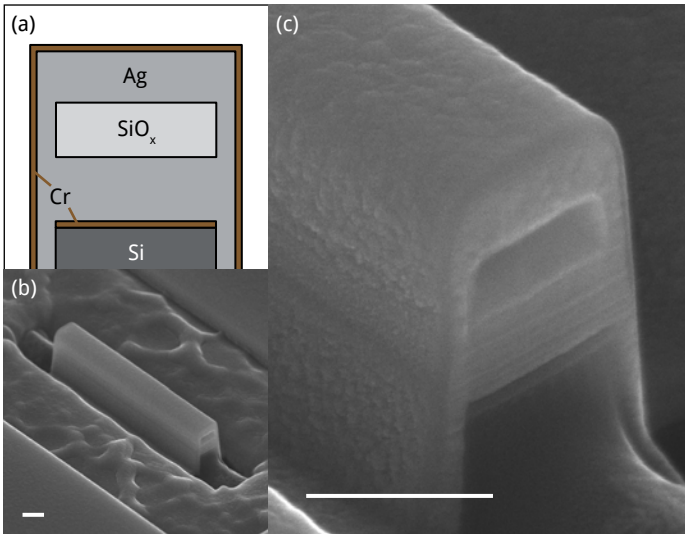

Figure 7.1: Scanning electron micrographs of a 2 µm long, focused-ion-beam fabricated MIM waveguide. **(a)** Schematic of the end facet, showing the Si/Cr/Ag/SiO_x/Ag/Cr layer structure. **(b)** Finalized waveguide **(c)** Detail of end facet. Scale bars: 200 nm

An MIM plasmon mode that exists in this geometry will propagate through the waveguide and reflect at the end facets, giving rise to standing plasmon waves. At the end facets, plasmons propagating through the MIM waveguide will not only reflect, but also couple to far-field radiation. We have studied this emission by recording the emitted spectrum as function of position of the electron beam across the surface of the waveguide. The waveguide is excited using a 30 keV, ~1 nA beam of a scanning electron microscope (SEM). The light emission that results from this excitation is spectrally detected for each position of the electron beam (exposure time: 0.25 s).

Figure 7.2 shows the result of an electron beam scan over a 600 nm × 2000 nm area in 20-nm steps. The recorded intensity is plotted for two wavelengths. The scan clearly shows the outline of the waveguide; it is brighter than the surroundings. The CL emission that is excited on the waveguide also shows a strong position dependence: at 910 nm emission wavelength we observe 6 maxima along the waveguide axis while at 624 nm 11 maxima are found. We attribute these maxima in CL emission to the antinodes of a standing plasmon wave [58, 115], in agreement with the increasing number of maxima for a shorter wavelength and the fact that the separation between two maxima equals half a plasmon wavelength in this geometry (see below).

Figure 7.3 shows the full spectrum recorded in a line scan of the electron beam along the waveguide axis; at each 5-nm step of the electron beam a spectrum is

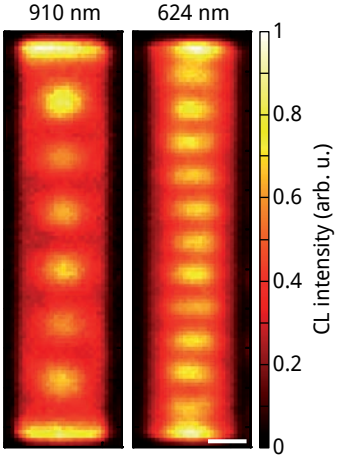

Figure 7.2: Excitation maps of the plasmon resonances at 910 nm and 624 nm, respectively, of an 85-nm-thick MIM waveguide with a 400-nm-wide SiO_x core, obtained using 30 keV electron-beam excitation. The cathodoluminescence intensity at the indicated wavelength is given as function of position of the electron beam (20-nm steps). Clearly, two different resonances are excited, having 7 and 12 half-wavelengths fit in the waveguide length, respectively. Scale bar: 200 nm

collected. Data for the waveguide of Fig. 7.2 with a 400-nm-wide SiO_x core is shown in the left panel. A large number of resonances are clearly resolved, each corresponding to an integer number of half-wavelengths fitting in the waveguide length. Towards shorter wavelengths, up to 15 antinodes within the waveguide are seen ($\lambda_0 = 500$ nm). The signal vanishes for shorter wavelengths due to increasing losses of the MIM plasmon mode.

The data for the 190-nm-wide waveguide (Fig. 7.3(b)) shows a completely different behavior. In the 600–700 nm spectral band, the waveguide supports resonances, similar to the wider waveguide, although at a larger period between the maxima. However, at longer wavelength, the resonances become more closely spaced in the wavelength domain, in contrast to the data for the wide waveguide, where resonances are observed in greater steps as the wavelength is increased. Correspondingly, for the narrow waveguide, the spacing between maxima along the waveguide rapidly increases for increasing wavelength. The standing wave antinodes in the narrow waveguide of Fig. 7.3(b) merge together in a band around ~800 nm. The constant CL intensity along the MIM waveguide at 800 nm and the fact that no antinodes are observed for longer wavelength clearly show that at this wavelength cutoff occurs. At cutoff the electromagnetic field in the waveguide oscillates in phase along the entire waveguide, corresponding to $n = 0$. For wavelengths longer than cutoff, no propagating modes exist and the field of a radiating dipole in the waveguide will decay exponentially. Indeed, Fig. 7.3(b) shows decaying intensity tails near the ends of the waveguide above 800 nm.

To further investigate the relation between cutoff wavelength and waveguide

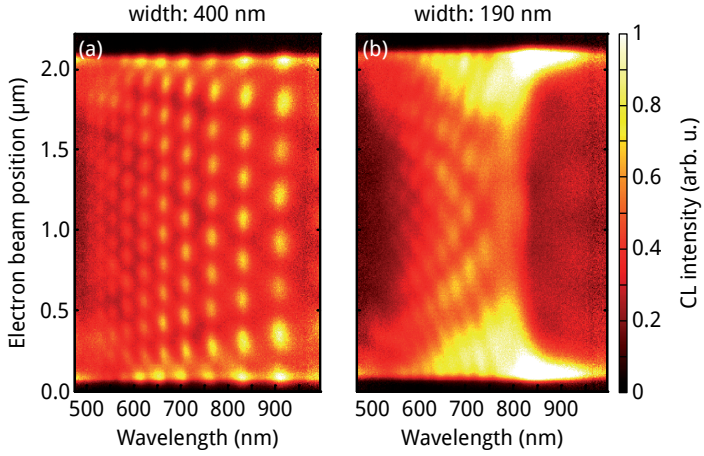

Figure 7.3: Cathodoluminescence spectrum versus electron beam position for MIM waveguides with an 85-nm-thick, **(a)** 400-nm-wide and **(b)** 190-nm-wide SiO_x core. The electron beam was scanned in a line over the axis of the 2 μm long waveguide. The 190-nm-wide waveguide shows cutoff near 800 nm.

width, Fig. 7.4 shows integrated spectra from a range of waveguides with different widths. Data are taken by integrating spectra over a 500-nm-long line scan along the center of the waveguide. The spectrum from the 400-nm-wide waveguide is shown in Fig. 7.4(a), and has emission peaks throughout the spectrum consistent with Fig. 7.3(a). The spectra for the 190-nm-wide waveguide shows cutoff around 800 nm as evidenced by the sharp decrease in intensity, and a number of resonant peaks at shorter wavelengths, as is also clear from Fig. 7.3(b). For narrower waveguides the cutoff wavelength monotonically shifts towards shorter wavelength: for a 120-nm-wide waveguide cutoff occurs at 570 nm. These data show that cutoff can be controlled over the full visible/near-infrared spectral range by varying the waveguide width from ~100 to 200 nm. In all cases, the emission is clearly enhanced at cutoff, an effect that is most pronounced at 150 nm width.

The detailed spatial and spectral distributions collected using CL spectroscopy can now be used to derive the dispersion of the lowest order plasmon mode for each waveguide. Figure 7.5 shows the dispersion relation of 9 different waveguides determined by analysis of line scan data as in Fig 7.3. The resonant mode energies were obtained by fitting spectra as in Fig 7.4(a) using a Lorentzian profile. A background signal attributed to transition radiation was subtracted from the data. The k-vector was determined by counting the number of half-wavelengths m in the waveguide length $L = 2\,\mu$m using $k = m\pi/L$ and assuming a phase jump equal to zero upon reflection at the waveguide ends. In this way, several (up to 10), experimental dispersion data points could be derived for each waveguide width. These data are plotted in Fig. 7.5 for the 9 waveguide widths: data are found for mode numbers in the range $m = 3$–16 (see top horizontal axis). The solid black line in the figure is the light line in vacuum. The dashed black curve shows the calculated

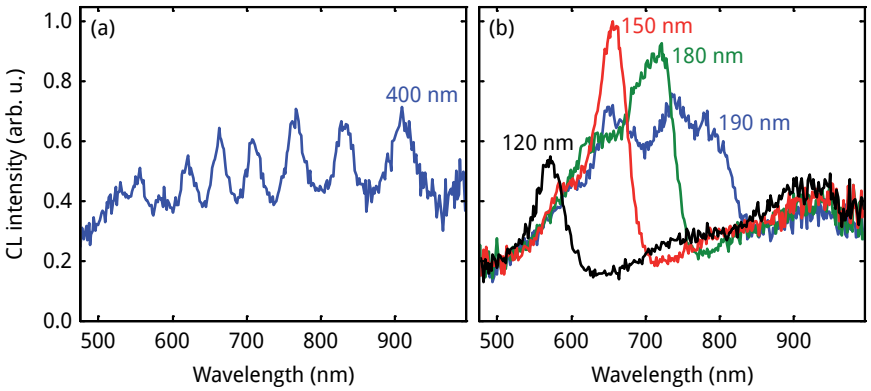

Figure 7.4: Spectra emitted from MIM waveguides with different widths. The 400-nm-wide waveguide **(a)** shows distinct resonances. Narrower waveguides **(b)** show cutoff at a wavelength that monotonically decreases with waveguide width. At the cutoff wavelength, the CL emission is strongly enhanced.

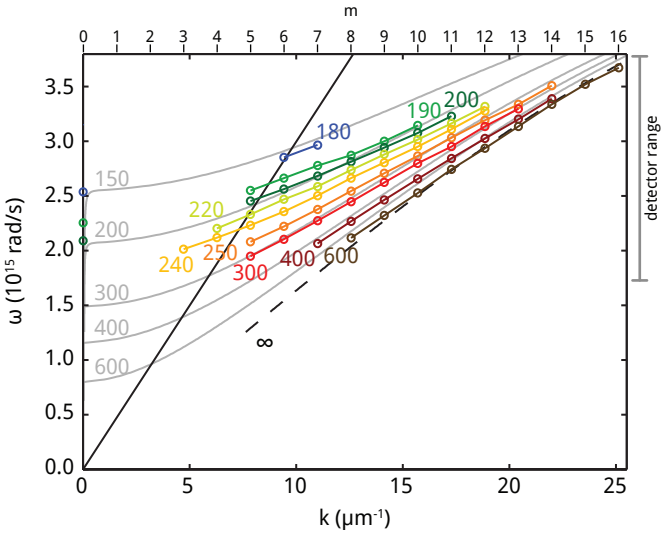

Figure 7.5: Dispersion relation for MIM waveguide modes above and close to the cutoff frequency. The width (in nm) of the waveguide core is indicated next to the curves. Black dashed curve: calculated MIM dispersion for an infinitely wide MIM slab. Grey curves: calculated MIM dispersion in narrower waveguides. Solid line: light line in air. The data points on the y-axis are the cutoff frequencies derived from the CL spectra. The available spectral detection range is indicated at the right hand side. Resonant mode numbers ($k = m\pi/L$) are indicated on top.

dispersion of the symmetric lowest-order MIM mode in an infinitely extended MIM stack consisting of an 85-nm-thick SiO_x layer (refractive index: 1.5) embedded in Ag. The grey curves indicate the calculated dispersion for the waveguides with finite widths [185]. The data show that when the waveguides become narrower, the dispersion undergoes a strong shift with a progressively smaller k-vector observed at a given plasmon frequency. The experimental data agrees well with the calculated dispersion relations over the whole range of waveguide widths. This demonstrates that the spatially-resolved electron beam spectroscopy technique is an excellent method to probe the dispersion of waveguide modes buried in the substrate. The good correspondence between experiment and calculation also indicates that the assumption of zero phase jump at the waveguide end facets is correct. Data points for low m for the narrowest waveguides could not be taken because at the corresponding wavelengths the visibility of the mode pattern was too weak to reliably derive the plasmon frequency. For the 190–240-nm-wide waveguides, data corresponding to m = 3–5 are found that lie left of the light line (for wider waveguides, these modes fall outside the range of the detector sensitivity). Such modes will weakly couple to free-space radiation due to leakage through the finite metal layer thickness. Preliminary measurements on waveguides that are

completely encapsulated in Ag, without open end facets, indeed show that clear resonant behavior as well as cutoff can also be probed when there is no direct radiation from the end facets indicating the waveguide acts as a resonant antenna. Figure 7.5 also shows data for $k = 0$; these are the cutoff frequencies at which the CL spectra are at half the peak value.

The small slope of the dispersion towards low frequency corresponds to a strong reduction in the group velocity $v_g = \mathrm{d}\omega/\mathrm{d}k$, and correspondingly a large increase in density of states. From the dispersion relation we find a v_g as low as 0.21 c. The strongly enhanced CL intensity observed at cutoff is a direct measure of the enhanced density of states.

Finally, we study the phase distribution in the waveguide by measuring the angular CL emission pattern. Figure 7.6 shows the emission at 700 nm from two waveguides with widths of 210 and 170 nm that are excited by an electron beam at the center of the waveguide. The waveguides are oriented vertically in the figure. At 700 nm, the 210-nm-wide waveguide is far from cutoff and its dispersion lies below the light line. Hence, when this waveguide is excited, the emission at 700 nm only emerges from the waveguide ends. Figure 7.6(a) shows a clear fringe pattern which is attributed to interference of the emission from the two waveguide ends. The narrower 170-nm-wide waveguide is at cutoff at 700 nm. The oscillation in the waveguide is therefore in phase and above the light line, allowing direct coupling of the plasmon resonance to the far field. The angular emission pattern at 700 nm in Fig. 7.6(b) clearly shows two lobes corresponding to the angular emission pattern of a line dipole antenna. This confirms the waveguide oscillates in phase ($k = 0$).

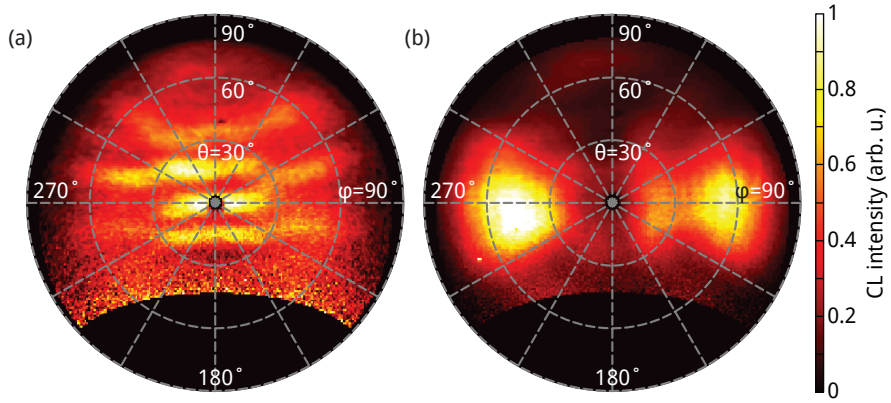

Figure 7.6: Angular emission profiles at 700 nm from waveguides above and at cutoff. Waveguides are oriented vertically in the figure. **(a)** A 210-nm-wide waveguide, far from cutoff, shows interference of radiation from the waveguide ends. **(b)** For the 170-nm-wide waveguide at cutoff, two clear lobes are observed indicative of oscillation with constant phase along the waveguide.

7.3 Conclusions

In conclusion, we have observed propagating optical modes with vanishing phase advance ($n = 0$) in metal-insulator-metal waveguides at cutoff. Resonant guided plasmon modes buried in the metal-insulator-metal stack were excited by a 30 keV electron beam incident on the waveguide. By scanning the beam, standing plasmon waves inside these waveguides were directly resolved both spectrally and spatially. From the data the dispersion relation was derived over a broad spectral range for a range of waveguide widths. Strong modal dispersion is observed, in particular near the cut-off frequency: a group velocity as low as 0.21 c is found. At cutoff, when effectively $n = 0$, the waveguide radiates in a line dipole antenna emission pattern. At this condition, we have observed a strongly enhanced density of states. The metal-insulator-metal plasmon waveguides provide an ideal tool for nano-scale integrated optical circuits, nanolasers and radiative decay control in active metamaterials.

7.4 Methods

Device fabrication

MIM waveguides were fabricated by thermal evaporation onto a Si substrate of 10 nm Cr, 100 nm Ag and 85 nm SiO_x layers. In this layer stack, rectangular ridges are defined using focused-ion-beam milling using an FEI Helios dual beam system. Subsequently, layers of 100 nm Ag and 10 nm Cr are sputtered onto these ridges, resulting in a SiO_x core that is completely embedded in Ag. As a final step, the end facets of the waveguide are defined using focused-ion-beam milling (see Fig. 7.1(b) and (c)), resulting in a 2 µm long waveguide. The width of the SiO_x core was varied from 100 to 600 nm.

Measurement techniques

Samples were placed in the vacuum chamber of an FEI XL30 SEM equipped with an 11 mm high parabolic mirror positioned between the pole piece and the sample. A 600 µm hole in this mirror allows the electron beam to fall through. The mirror is mounted on a piezoelectrically controlled stage having two translation and two rotation axes, allowing the mirror to be accurately aligned. The mirror casts the light that is emitted from the electron beam focus (covering a 1.46π sr solid angle) as a parallel beam onto an achromat lens that focuses it into a 600 µm core diameter optical fiber. The fiber is fed to a spectrometer (grating: 150 l/mm, blaze 800 nm) equipped with a LN cooled CCD array detector. The spectral resolution is 15 nm. The electron beam (30 keV, ~1 nA) is scanned over the sample in 5–20-nm steps; for every pixel the emission spectrum is acquired with an exposure time of 0.25 s. The spectrum is corrected for system response using both the measured and calculated transition radiation spectrum, which is emitted when 30 keV electrons impinge on

a planar Au surface. Angular emission profiles were recorded by directly imaging the emission from the parabolic mirror into a 2D CCD array detector. By a transformation of the data a (θ, φ)-plot is obtained.

8

Applications

This chapter discusses possible applications inspired by this thesis. We present:

- *a sensitive ultra-small localized surface plasmon sensor;*
- *a surface plasmon laser;*
- *a template stripping technique for the large-scale replication of ion-milled structures;*
- *an in-situ monitor that enables better control over the focused-ion-beam milling process;*
- *a novel design for a single-photon source for use in quantum optical communication.*

8.1 Introduction

In this thesis several focused-ion-beam fabricated metal cavities were presented. These cavities confine light to a very small volume. The confinement is due to surface plasmons, oscillations at optical frequencies of the free electrons in the metal. Surface plasmons enable the manipulation of light at very short length scales due to their inherent confinement and tunable dispersion. This thesis introduces cathodoluminescence imaging spectroscopy as a new method to resolve the confinement, dispersion and modal structure of surface plasmons in these nanoscale cavities at deep-subwavelength scale.

The insights derived from this work inspire several new applications that may be realized using further research and development. In section 8.2 we investigate how the plasmonic whispering gallery nanoresonators described in chapters 4 and 6 can be used in a small-footprint refractive index sensor. In section 8.3 the same geometry may be used to realize an ultra-small whispering gallery ring laser. Section 8.4 and 8.5 describe applications related to the ion milling technique that is central in this thesis; in section 8.4 we introduce an in-situ monitoring technique during FIB milling; in section 8.5 a template stripping technique to replicate ion-milled structures is presented. Finally, in section 8.6 we introduce a novel concept for a single photon source that is directly derived from the new cathodoluminescence imaging spectroscopy technique developed in this thesis.

8.2 A localized surface plasmon sensor

Application of surface plasmon technology is widespread in sensing [6]. Surface plasmon resonance (SPR) sensors are commercially available and use a metal-coated prism in the Kretschmann reflection geometry. By probing variations in the angle/wavelength dependent reflection due to the excitation of surface plasmon polaritons on the metal film, the refractive index of an analyte at the surface is sensitively measured. One major disadvantage of the prism-based geometry is that it is bulky as it relies on the measurement of a surface plasmon that propagates over a relatively large distance and that relatively large amounts of analyte are required.

To solve this problem, the sensor can be based on plasmons confined to metallic resonators in which light at the cavity resonance frequency is recirculated in a small volume. Such localized surface plasmon resonance (LSPR) sensors [192] hold promise for devices with an intrinsically small footprint and offer a range of possible applications in miniaturized geometries, nanofluidics and multiplexing arrangements [193].

The resonance of an LSPR sensor undergoes a spectral shift as a result of a change in the refractive index of the surrounding medium. A measurement of this shift, for example by recording the scattered intensity at a certain wavelength, is thus a sensitive probe of the refractive index change. The figure of merit for the sensitivity is defined as FOM = $\Delta\lambda/(\Delta n W)$, with $\Delta\lambda$ the spectral shift as a result of index change Δn of the resonance with spectral full-width-at-half-maximum W. Aside from having a high FOM, an effective geometry must also be integrable with read-out optics [193].

Here we present a plasmonic ring resonator in Au as a localized plasmon sensor. As described in this thesis (chapters 4, 5 and 6), the resonator supports a multitude of plasmon resonances that can be tuned throughout the visible wavelength range. The resonator is bound to the Au surface, which makes it an interesting candidate for integration and addressing of single resonators. The resonance of an individual resonator can be measured by recording its scattering spectrum. Alternatively, the

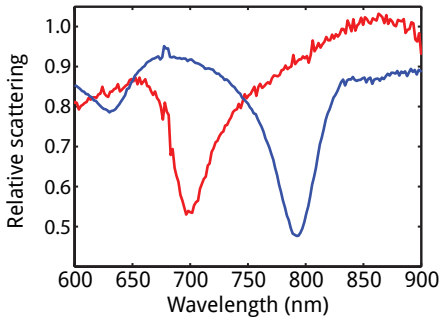

Figure 8.1: Scattering spectra of a 260-nm radius, 375-nm-deep ring resonator having a groove filled with air (red curve) and with PVB (blue curve). From the spectral shift and resonance width, the refractive index sensitivity can be derived.

metal sensor geometry could be integrated with a p-n junction to directly detect the local resonant intensity [194].

We investigate the sensitivity by studying the spectral shift of the resonance as a result of infilling the resonator by a dielectric medium. Figure 6.1 shows a ring resonator infilled with poly-vinyl butyral (PVB), a polymer with a refractive index $n = 1.49$. Figure 8.1 shows scattering spectra of a 260-nm radius, 375-nm depth ring resonator, infilled with air (red curve) or with PVB (blue curve). The spectral shift of the 40-nm-wide resonance is 94 nm, corresponding to a FOM of 4.8. While the geometry studied here was not optimized for sensing, this sensitivity is already comparable to that of other localized plasmonic sensors reported [195, 196]. The sensitivity could be further improved using two different strategies. First, the width of the resonant peaks depends on radiation losses. These losses and thereby the resonance width are reduced for higher-order resonances in larger-radius rings. Sensors based on these rings offer an increased sensitivity while still having a wavelength-scale size. A second strategy takes advantage of interference effects. As we have demonstrated in chapter 6, scattering spectra from the ring resonator have a Fano-type line shape, due to interference between scattered and reflected light. This interference could be engineered to provide sharp spectral features (e.g. by using a dielectric surface layer to modify the reflection), thereby increasing the sensitivity [197].

The sensitivity is also strongly influenced by noise in the spectral measurement. The spectra in Fig. 8.1 were taken in sub-second exposure times on a cooled CCD array detector while the surface plasmon sensor was illuminated with an intensity less than 1 μW. The measurement shows that at this noise level, refractive index changes could be resolved that are much smaller than the $n = 1$ to $n = 1.49$ shift of the material in this sensor. Moreover, there is ample room for improvement of the signal-to-noise level by increasing the exposure time and illumination intensity.

In conclusion, the possibilities for integration and incorporation in microfluidic

environments and the prospects of further improvements show that plasmonic ring resonators are promising geometries for compact, sensitive and highly integrable sensing devices.

8.3 A surface plasmon laser

Lasers with a nanoscale footprint hold great promise for application in opto-electronic circuits, where optical and electronic functionality are integrated on a single chip. Conventional waveguide-type lasers typically have sizes that are not compatible with the 10–100 nm dimensions of the electronic circuit architecture. Plasmon lasers offer a solution to this problem, as light is confined by the metal-dielectric interface, leading to tight lateral confinement of light.

Cavities employing surface plasmons enable a further reduction of the laser size. Indeed, as demonstrated in chapter 5, the mode volume in a whispering-gallery type plasmonic cavity is well below λ_0^3. Plasmons bound to a metal-dielectric interface can be amplified in a manner analogous to amplification of light in a conventional dielectric laser cavity provided that the plasmon interacts strongly with a high-gain dielectric. The first surface plasmon lasers have recently appeared, using either metal-insulator-metal cavities [186], or a metal geometry in which the confinement is due to a nanostructured dielectric waveguide [187, 198].

Here, we present a cavity geometry that can be used to create the first plasmonic ring laser. Cavities consisting of a circular groove in a flat metal surface (see Fig. 6.1) confine surface plasmons inside the groove, allowing an integer number of plasmon wavelengths to fit in the circumference. A surface plasmon laser based on this whispering gallery-type cavity will show far-field emission with a distinct angular dependence that is determined by the azimuthal mode order, as we have demonstrated in section 6.4. The mode volume in these cavities can be as small as $10^{-3}\lambda_0^3$.

In the geometry we propose here, the groove in which the resonant mode is confined is filled with a gain medium. As plasmons are intrinsically lossy, a high gain is required to compensate for the losses and achieve lasing. Conjugated polymers have gain values of up to $10^4\,\mathrm{cm}^{-1}$ and can be embedded in the groove using spin coating. Here we use poly(9,9-dioctylfluorene) (PFO) as a gain medium, for which lasing at λ_0 = 450–460 nm has been demonstrated in dielectric geometries [199–202] under pulsed excitation at 350–390 nm. Figure 8.2(a) shows a ring cavity infilled with PFO fabricated using spin coating and a subsequent heating step, showing complete infilling.

To demonstrate the feasibility of this plasmon laser geometry, we plot in Fig. 8.2(b) the threshold gain required to overcome the losses of the plasmon mode propagating in a 500-nm-deep, 100-nm-wide straight Ag groove infilled with PFO (n_{polymer} = 1.7), obtained by calculating the losses of the lowest-order surface plasmon mode in this groove using the boundary element method. Also plotted in Fig. 8.2(b) is the gain spectrum of PFO. As a first approximation it is assumed that

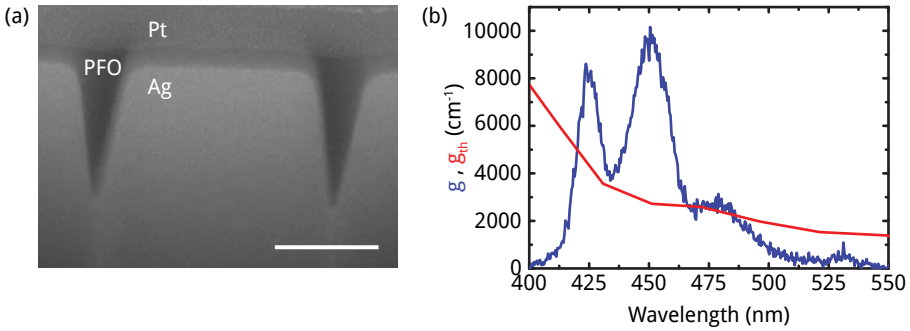

Figure 8.2: A PFO-based surface plasmon ring laser. **(a)** Scanning electron micrograph of a cross section through ring cavity infilled with gain medium. The Ag substrate, the PFO polymer and a Pt protection layer are indicated. Scale bar: 300 nm **(b)** PFO gain spectrum and calculated threshold gain for a groove plasmon in a 500-nm-deep Ag groove.

the plasmon mode profile is fully confined in the polymer. Also, radiation losses are not included (see chapter 5 for details on radiation losses). In this first-order analysis, the figure shows that around 450 nm, the PFO gain exceeds the plasmon loss by a factor three. It is thus expected that if the PFO is efficiently excited, plasmons propagating through the groove will be amplified giving rise to laser oscillation in the plasmonic ring cavity. The ring geometry allows for excitation by a pump laser incident from the top, exciting the polymer at a wavelength that is off-resonance with the cavity. Initial experiments to test this lasing geometry using a 350 nm 5 ps laser show that PFO incorporated in the groove gives rise to a strong luminescence. The far-field pattern of the laser emission can be engineered by choosing the symmetry of the lasing mode.

In conclusion, the plasmonic ring cavity geometry may thus enable the realization of an ultra-small plasmonic whispering gallery laser, offering control over mode confinement and coupling to the far field by selecting the resonant modes.

8.4 Light detection as a monitor for focused-ion-beam milling

In a focused-ion-beam (FIB) system, Ga^+ ions are accelerated to an energy of typically 30 keV and focused to a beam waist of 10-20 nm. The ions transfer energy to the atoms near the surface leading to sputtering, the gradual removal of surface atoms. In addition, secondary electrons are emitted and light is generated.

The ion-excited secondary electrons can be used for imaging and offer contrast between different crystal domains that is not available in regular electron beam microscopy. While ion beam imaging is often undesired because of damage to the

sample, it provides additional imaging contrast not present in electron microscopy. The disadvantage of ion beam electron imaging is that it induces a gradual erosion of the sample, limiting its use.

In a dual-beam FIB system an electron beam column is integrated to perform electron microscopy to directly image the sample as it is milled. In this way, detailed studies of the ion milling process can be made in real time.

Here we propose the use of light emission from the sample as an additional monitor during FIB milling. The so-called ionoluminescence [203] is collected by a system comprising an optical fiber which guides the light into a spectrometer [204]. Alternatively, cathodoluminescence generated by electron irradiation can be collected by the same fiber. Figure 8.3(a) shows the light collection system that we developed, consisting of a vacuum-compatible 600 µm core-diameter optical fiber mounted onto a microscope stub that collects the light from the beam impact position. The fiber guides the light into a spectrometer equipped with a CCD array detector for parallel spectral collection (Fig. 8.3(b)). When collecting through an optical fiber in the presence of an ion or electron beam, spurious contributions arising from iono- or cathodoluminescence of the fiber have to be prevented. For this purpose, the fiber is mounted at a shallow angle to the sample surface, in order to minimize irradiation of the fiber by ions, electrons or atoms originating from the beam impact position.

The spectrum that is emitted upon ion beam impact is very dependent on the target material. We have observed luminescence from Au, Si and In showing characteristic spectra with many (> 20) sharp (< 2 nm) peaks at visible wavelengths. From the spectrum, the material that is irradiated can directly be identified. For a multilayer sample, these spectra can be continuously collected during FIB milling, providing a direct monitor of the material that is removed [205, 206]. Correspondingly, a change in spectrum during milling is a clear indicator that the FIB process has reached an interface.

We illustrate the use of the ionoluminescence spectrum as an in-situ FIB monitor in Fig. 8.4(a), which shows consecutive emission spectra (exposure time: 5 s) from a surface consisting of a 300-nm-thick SiO_2 layer on top of a Si substrate as

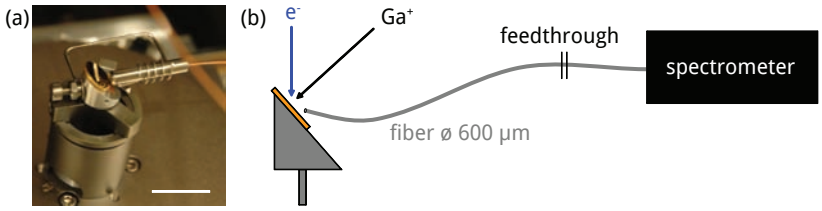

Figure 8.3: In-situ light collection system using an optical fiber mounted close to the sample position in a focused-ion-beam system. **(a)** Photograph of a microscope stub with sample and fiber. **(b)** Schematic of light collection system, showing how the electron beam and Ga^+ beam are incident on the sample. Scale bar: 2 cm

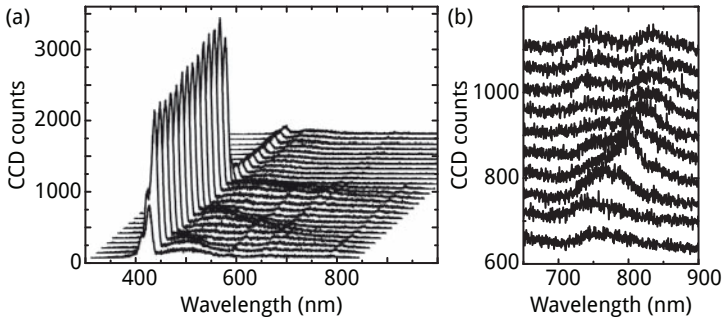

Figure 8.4: Ionoluminescence and cathodoluminescence spectra collected during focused-ion-beam milling. **(a)** Ionoluminescence from a 300 nm SiO_2 layer on top of a Si substrate as material is sputtered from the surface by a 30 keV 21 nA Ga^+ beam (exposure time: 5 s). **(b)** Cathodoluminescence from a surface plasmon nanoresonator as its resonance shifts during fabrication. Spectra are shifted for clarity; the bottom spectrum is taken first (exposure time: 3 s)

it is milled by a 21 nA Ga^+ beam. The first exposures show a distinct spectrum peaking at 420 nm that is attributed to optical transitions in the SiO_2 layer and atomic emission from sputtered atoms. As the milling progresses through the layer, the spectrum remains the same, indicative of a homogeneous layer. At the 16^{th} spectrum, there is a sudden change in emission at 420 nm. At this stage, the SiO_2 layer is fully removed and the ion beam progresses by milling the Si substrate. It is estimated that on this substrate, at least a 1 μm^3 volume of material is sputtered from the Si layer before it is detected.

The monitoring system can be further extended by using electron beam excitation during FIB milling. The additional cathodoluminescence allows for the observation of additional features that are not present in the ionoluminescence spectrum. We illustrate this concept by monitoring the cathodoluminescence that is emitted from an optical nanoresonator as it is being fabricated in a Au surface. The nanoresonator consists of a circular groove (see Fig. 6.1(a)) that supports an optical resonance that is strongly dependent on the groove depth. The resonance can be excited by electrons incident on the resonator; the emitted cathodoluminescence spectrum shows a peak at the resonant wavelength (see chapter 6). During fabrication of the resonator (radius: 210 nm) by a 1.5 pA 30 keV Ga^+ beam, it is excited on the center plateau by a 22 nA electron beam. Figure 8.4(b) shows the cathodoluminescence spectra (exposure time: 3 s) recorded while the ion beam mills the groove of the resonator with a groove depth increasing from 0 to ~500 nm. In the first spectrum, a peak is visible at 740 nm, corresponding to the $m = 0$, $n = 1$ resonance. Consecutive spectra show that this peak shifts to a longer wavelength, consistent with the resonance red shift as the groove depth is increased (see chapter 4). As the groove depth increases further, a second resonator peak appears at 720 nm, corresponding to a higher order azimuthal mode ($m = 1$, $n = 1$). These

in-situ spectra demonstrate that geometric optical resonances can be monitored in real-time during FIB fabrication enabling direct feedback of the milling process.

In conclusion, a system is presented in which ionoluminescence and cathodoluminescence emission is collected in a focused-ion-beam system providing detailed complementary in-situ information on the ion milling process. A detection system collecting light from the beam impact position enables materials identification, monitoring of multilayer sample milling and monitoring of nanophotonic resonances as the surface is shaped by the ion beam.

8.5 Template stripping off focused-ion-beam-structured Si templates

Nanolithography techniques have been key enablers for today s low-cost and high-performance electronic integrated circuits. These applications require a high spatial patterning resolution and great scalability. On the other hand, scientific experiments or industrial tests often require rapid prototypes: nanostructures that can be fabricated rapidly without the need for scalable fabrication. Focused-ion-beam milling is a unique technique that is suitable to fabricate such prototypes. The scanning 30 keV Ga^+ beam that is used in a typical FIB system allows for patterning of a variety of materials and provides a high resolution down to 10 nm. However, due to the use of a single scanning beam, FIB is not useful for large-volume lithography. Here we present a method using FIB for high-resolution patterning of metal layers with a re-usable template that allows for rapid prototyping, but which is also suitable for larger scale replication.

The proposed technique uses FIB patterning of the surface of a polished silicon wafer to create a template that is then used to replicate the structure multiple times. This template replication technique was proposed before [103], but a patterning resolution below 100 nm was not yet demonstrated. Figure 8.5(a) shows an example of a patterned Si(100) template. In the center, a 100-nm-wide circular ridge was fab-

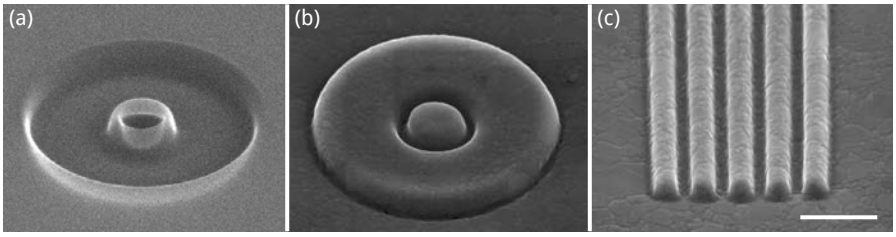

Figure 8.5: Scanning electron micrographs of silicon template and stripped metal layers. **(a)** Focused-ion-beam-fabricated template in a Si(100) wafer. **(b)** Ag structure as stripped from a template similar to the template in (a). **(c)** Ag grating, showing gaps of 100 nm width between the ridges. Scale bar: 500 nm

ricated by sputtering material away around this ridge using 30 keV Ga^+ ion milling. Due to the well-controlled crystallinity of the substrate, structures are smooth and made with very high resolution. In a next step, a metal layer (thickness typically tens of nm) is evaporated or sputtered onto the template. Subsequently, a second silicon wafer is glued onto the metal surface using an epoxy resin. After curing of the epoxy, the adhesion of the metal to the epoxy is stronger than the adhesion to the patterned template. Therefore, the metal layer can be stripped off the template. Figure 8.5(b) shows a Ag structure obtained using this template stripping technique. The silicon substrate used was similar to the one shown in Fig. 8.5(a); on top of this template a 100 nm Ag layer was sputtered. The image shows that after stripping this layer off, the template features are well replicated in the metal film: the circular ridge on the silicon substrate gives rise to a circular groove in the metal. Figure 8.5(c) shows another template-stripped structure, composed of a grating made in Ag. This figure demonstrates that gaps can be patterned with sub-100-nm gap size. The silicon substrates used for these structures can be reused after stripping, allowing for fabrication of a large number of identical structures without the need to use additional FIB milling steps.

While the Ag structures in Fig. 8.5(b) and (c) show precise reproduction of the Si template, close inspection using electron microscopy shows small surface roughness that is not present in the template. This roughness is attributed to the polycrystalline nature of the evaporated Ag layer. The roughness may be reduced by the evaporation rate or sample temperature. Also, depending on the geometry, annealing may be used to grow crystal grains beyond the size of the patterned structure [103].

In conclusion, template stripping off focused-ion-beam-milled Si templates can be used to reproduce complex nanostructures at high precision in a limited number of processing steps. Templates can be reused, allowing to scale up sample fabrication and providing a means to repeatedly fabricate identical structures.

8.6 Single-photon source

Future quantum optical techniques for communication or computation heavily rely on the availability of sources of single photons [208, 209]. Single-photon sources that are presently being investigated often consist of quantum dots, atoms or NV-centers in diamond. In an ideal single-photon source, the generation of a single photon is determined by a trigger signal. Excitation of emitters by a short laser pulse allows for such a trigger. However, in such triggered sources the photons are emitted with a time uncertainty that is on the order of the radiative lifetime, which is typically several nanoseconds. Moreover, due to the stochastic nature of the excitation process, the excitation rate per laser pulse is uncertain. Alternatively, quantum optical devices can be based on a herald signal that announces the generation of a single photon.

In this section, we will discuss the coupling of an electron beam to an optical

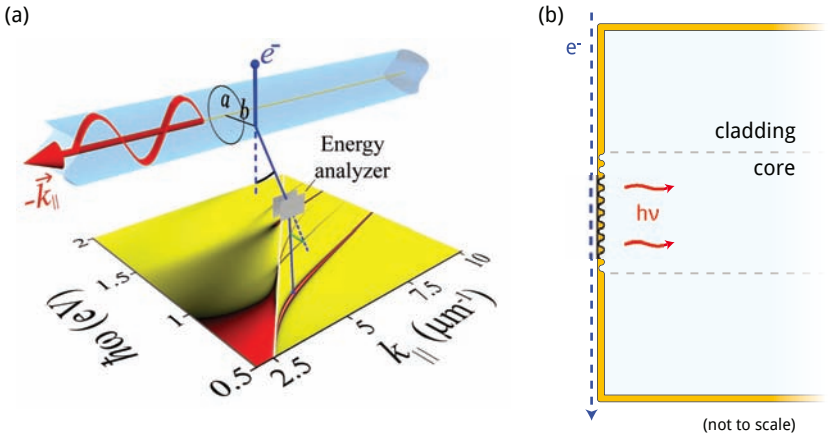

Figure 8.6: Schematic for excitation of a single photon in an optical optical fiber by an incoming electron. **(a)** (from Ref. [207]) Geometry for electrons that pass the fiber perpendicularly. As a result of coupling to a guided photon, the electron loses energy (analyzed by an electrostatic analyzer) and transfers momentum, resulting in deflection of the electron trajectory. **(b)** An alternative geometry consisting of an optical fiber of which the end facet is coated with a Au film. At the fiber core, a grating provides efficient coupling of the electron beam to a waveguided photon.

fiber as a strategy for producing heralded single photons. The source has excellent timing accuracy, a potentially high photon yield and a tunable emission over a very broad spectral range that is conveniently coupled into a single-mode optical fiber.

Figure 8.6(a), taken from Ref. [207], shows a realization of a single photon source using electron beam excitation, involving an electron beam passing by an optical fiber. When the distance between the electron beam and the fiber is sufficiently short, evanescent coupling occurs of the electric field generated by the moving electrons to the waveguide modes of the fiber. As a result, photons are excited that travel through the optical fiber. The photogeneration process is a statistical process with a probability that is typically 10^{-4}–10^{-6} depending on the geometry and electron energy. To detect if a certain electron has generated a photon, the energy and momentum of the electron are measured. When an electron excites a guided photon, it loses an amount of energy equal to the photon energy. The electron also experiences a recoil $\hbar k$, with k the wave vector of the photon. The lateral momentum that the electron beam acquires leads to deflection of the electron trajectory at the waveguide as shown in Fig. 8.6(a). This deflection is difficult to measure for realistic beam conditions given the typical angular spread in the beam. However, the electron energy loss can be readily measured using a sensitive electron spectrometer. Indeed, energy-loss spectrometers in modern TEM systems have sub-0.1 eV resolution and are able to distinguish energy losses of less than 1 eV. This allows for measuring the electron energy loss corresponding to the

generation of a single photon quantum. Using a sensitive, high-speed detector such as a photomultiplier tube or avalanche photodiode, single electrons can be detected. In this way, an electron energy-loss measurement showing a distinct energy loss in the desired range generates a herald signal related to the generation of a single photon. Relying on this herald signal, the excitation of waveguided photons by electrons functions as a single photon source. Multiple-photon events are discarded as this leads to electron energy loss that is outside the set energy loss range. Due to the short length (several μm) over which the electron and the photon interact, the timing uncertainty in the photon generation is within tens of femtoseconds.

In a practical implementation of the single photon source, electrons may accidentally hit the fiber which leads to undesired cathodoluminescence. A single electron is able to excite many photons in this incoherent process, leading to a potentially large undesired background signal. Therefore, an effective shielding geometry must be employed to prevent electrons from directly impacting the optical fiber. In Figure 8.6(b) we present a geometry that may serve this goal in which the end facet of an optical fiber is covered with a Au film. Electrons impinging on the Au film could also give rise to cathodoluminescence emission, but the excitation efficiency is much lower than that for glass. Moreover, on the sides of the waveguides the Au layer can be made sufficiently thick for it to be intransparent for both photons and electrons. The structure could be fabricated using FIB milling and template

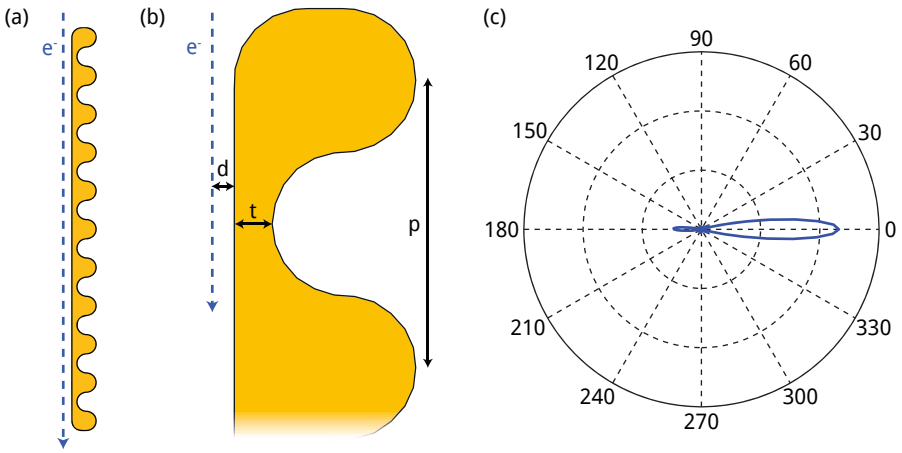

Figure 8.7: Boundary-element-method calculation of photon generation by a 30 keV electron. **(a)** Two-dimensional boundary geometry defining a Au grating. The blue dashed line indicates the electron trajectory. **(b)** Detail, showing grating pitch p, distance to the electron beam d and Au thickness t. **(c)** Angular emission pattern for excitation of this structure by a 30 keV electron. Parameters were $p = 150$ nm, $d = 10$ nm, $t = 20$ nm.

stripping. First, a Au film is evaporated onto a flat template, such as silicon or mica. FIB milling is subsequently used to pattern a grating onto this film. The gold film is then attached to the facet of an optical fiber using an optical epoxy resin. After curing of the epoxy, the film is stripped off the template, which exposes a flat Au surface (see sections 1.2 and 8.5). The Au film aids in preventing electrons from reaching the glass. Importantly, it also prevents the optical fiber from acquiring a static charge in case it would be hit by the electron beam. The grating patterned into the Au layer is aligned with the core of the waveguide (see Fig. 8.6(b)). When the grating pitch p satisfies the condition $p = \lambda_0 v/c$, with v the electron velocity, polarization of the grating by a passing electron generates directional diffraction radiation [210] that propagates into the fiber with vacuum wavelength λ_0. This condition is independent of the refractive index of the fiber core. The coupling configuration can be tuned to the desired wavelength by choosing electron energy or grating pitch p. Moreover, this geometry allows for tuning the emission wavelength λ_0 by rotating the fiber around its axis, which enlarges the effective grating pitch.

In order to investigate the emission characteristics of the proposed new geometry, boundary-element-method calculations [128, 140] were performed on a simplified model geometry. Figure 8.7(a) shows a free-standing Au grating (10 periods) in vacuum, the boundary of which was used as input for the calculations. The boundary was defined in 5-nm-steps. Figure 8.7(b) shows an enlarged detail view showing the distance to the electron beam $d = 10\,\text{nm}$. The Au thickness inside the grating grooves was taken $t = 20\,\text{nm}$. In this simulation structure, no fiber is present. However, studying the angular emission resulting from a passing electron provides good insight in the usability and efficiency of this source configuration. Figure 8.7(c) shows the angular emission upon excitation with a 30 keV electron ($v/c = 0.3$) at an operating wavelength of 500 nm (grating pitch $p = 150\,\text{nm}$). The figure shows that the emission is highly directional with a predominant beaming towards the right. This means that the energy lost by passing electrons is mostly due to photons that are emitted in the direction of the waveguide. The calculation also allows us to derive the efficiency with which photons are excited in this geometry. We find that at an electron energy of 30 keV the probability to excite a photon in the 450–550 nm wavelength range is $\sim 10^{-3}$.

In conclusion, the excitation of waveguided photons by passing high-energy electrons is a new and useful mechanism for deterministic single-photon generation. The geometry presented here can be readily applied in a standard scanning electron microscope system. Several options for integration of the concept in a miniaturized geometry come to mind.

References

[1] H. Raether, *Surface plasmons*, volume 111, Springer, 1988.

[2] T. W. Ebbesen, H. J. Lezec, H. F. Ghaemi, T. Thio, and P. A. Wolff, *Extraordinary optical transmission through sub-wavelength hole arrays*, Nature **391**, 667 (1998).

[3] W. L. Barnes, A. Dereux, and T. W. Ebbesen, *Surface plasmon subwavelength optics*, Nature **424**, 824 (2003).

[4] J. A. Schuller, E. S. Barnard, W. Cai, Y. C. Jun, J. S. White, and M. L. Brongersma, *Plasmonics for extreme light concentration and manipulation*, Nature Mater. **9**, 193 (2010).

[5] K. Okamoto, I. Niki, A. Shvartser, Y. Narukawa, T. Mukai, and A. Scherer, *Surface-plasmon-enhanced light emitters based on InGaN quantum wells*, Nature Mater. **3**, 601 (2004).

[6] Homola, J., *Surface Plasmon Resonance Based Sensors*, Springer, 2006.

[7] H. A. Atwater and A. Polman, *Plasmonics for improved photovoltaic devices*, Nature Mater. **9**, 205 (2010).

[8] S. Lal, S. Link, and N. J. Halas, *Nano-optics from sensing to waveguiding*, Nature Phot. **1**, 641 (2007).

[9] R. F. Oulton, G. Bartal, D. F. P. Pile, and X. Zhang, *Con nement and propagation characteristics of subwavelength plasmonic modes*, New J. Phys. **10**, 105018 (2008).

[10] M. Yan and M. Qiu, *Guided plasmon polariton at 2D metal corners*, J. Opt. Soc. Am. B **24**, 2333 (2007).

[11] E. Moreno, S. G. Rodrigo, S. I. Bozhevolnyi, L. Martín-Moreno, and F. J. García-Vidal, *Guiding and focusing of electromagnetic elds with wedge plasmon polaritons*, Phys. Rev. Lett. **100**, 023901 (2008).

[12] E. J. R. Vesseur, R. de Waele, H. J. Lezec, H. A. Atwater, F. J. G. de Abajo, and A. Polman, *Surface plasmon polariton modes in a single-crystal Au nanoresonator fabricated using focused-ion-beam milling*, Appl. Phys. Lett. **92**, 083110 (2008).

[13] I. V. Novikov and A. A. Maradudin, *Channel polaritons*, Phys. Rev. B **66**, 035403 (2002).

[14] S. I. Bozhevolnyi, V. S. Volkov, E. Devaux, and T. W. Ebbesen, *Channel plasmon-polariton guiding by subwavelength metal grooves*, Phys. Rev. Lett. **95**, 046802 (2005).

[15] S. I. Bozhevolnyi, V. S. Volkov, E. Devaux, J.-Y. Laluet, and T. W. Ebbesen, *Channel plasmon subwavelength waveguide components including interferometers and ring resonators*, Nature **440**, 508 (2006).

[16] S. Bozhevolnyi, V. Volkov, E. Devaux, J.-Y. Laluet, and T. Ebbesen, *Channelling surface plasmons*, Appl. Phys. A: Mater. Sci. Process. **89**, 225 (2007).

[17] D. Arbel and M. Orenstein, *Plasmonic modes in W-shaped metal-coated silicon grooves*, Opt. Express **16**, 3114 (2008).

[18] J. Dintinger and O. J. F. Martin, *Channel and wedge plasmon modes of metallic V-grooves with nite metal thickness*, Opt. Express **17**, 2364 (2009).

[19] E. J. R. Vesseur, F. J. García de Abajo, and A. Polman, *Modal decomposition of surface-plasmon whispering gallery resonators*, Nano Lett. **9**, 3147 (2009).

[20] P. Berini, *Plasmon-polariton waves guided by thin lossy metal lms of nite width: bound modes of asymmetric structures*, Phys. Rev. B **63**, 125417 (2001).

[21] J. Krenn and J.-C. Weeber, *Surface plasmon polaritons in metal stripes and wires*, Phil. Trans. R. Soc. Lond. A. **362**, 739 (2004).

[22] M. Sandtke and L. Kuipers, *Slow guided surface plasmons at telecom frequencies*, Nature Phot. **1**, 573 (2007).

[23] C. A. Pfeiffer, E. N. Economou, and K. L. Ngai, *Surface polaritons in a circularly cylindrical interface: Surface plasmons*, Phys. Rev. B **10**, 3038 (1974).

[24] G. Schider, J. R. Krenn, A. Hohenau, H. Ditlbacher, A. Leitner, F. R. Aussenegg, W. L. Schaich, I. Puscasu, B. Monacelli, and G. Boreman, *Plasmon dispersion relation of Au and Ag nanowires*, Phys. Rev. B **68**, 155427 (2003).

[25] J.-C. Weeber, A. Dereux, C. Girard, J. R. Krenn, and J.-P. Goudonnet, *Plasmon polaritons of metallic nanowires for controlling submicron propagation of light*, Phys. Rev. B **60**, 9061 (1999).

[26] E. Verhagen, M. Spasenović, A. Polman, and L. K. Kuipers, *Nanowire plasmon excitation by adiabatic mode transformation*, Phys. Rev. Lett. **102**, 203904 (2009).

[27] T. Holmgaard, S. I. Bozhevolnyi, L. Markey, and A. Dereux, *Dielectric-loaded surface plasmon-polariton waveguides at telecommunication wavelengths: excitation and characterization*, Appl. Phys. Lett. **92**, 011124 (2008).

[28] R. F. Oulton, V. J. Sorger, D. A. Genov, D. F. P. Pile, and X. Zhang, *A hybrid plasmonic waveguide for subwavelength con nement and long-range propagation*, Nature Phot. **2**, 496 (2008).

[29] J. Jung, T. Søndergaard, and S. I. Bozhevolnyi, *Gap plasmon-polariton nanoresonators: scattering enhancement and launching of surface plasmon polaritons*, Phys. Rev. B **79**, 035401 (2009).

[30] Y. C. Jun, R. D. Kekatpure, J. S. White, and M. L. Brongersma, *Nonresonant enhancement of spontaneous emission in metal-dielectric-metal plasmon waveguide structures*, Phys. Rev. B **78**, 153111 (2008).

[31] F. I. Baida, A. Belkhir, D. Van Labeke, and O. Lamrous, *Subwavelength metallic coaxial waveguides in the optical range: role of the plasmonic modes*, Phys. Rev. B **74**, 205419 (2006).

[32] R. de Waele, S. P. Burgos, A. Polman, and H. A. Atwater, *Plasmon dispersion in coaxial waveguides from single-cavity optical transmission measurements*, Nano Lett. **9**, 2832 (2009).

[33] S. I. Bozhevolnyi, J. Erland, K. Leosson, P. M. W. Skovgaard, and J. M. Hvam, *Waveguiding in surface plasmon polariton band gap structures*, Phys. Rev. Lett. **86**, 3008 (2001).

[34] C. R. Williams, S. R. Andrews, S. A. Maier, A. I. Fernandez-Dominguez, L. Martin-Moreno, and J. F. García-Vidal, *Highly con ned guiding of terahertz surface plasmon polaritons on structured metal surfaces*, Nature Phot. **2**, 175 (2008).

[35] S. A. Maier, P. G. Kik, and H. A. Atwater, *Observation of coupled plasmon-polariton modes in Au nanoparticle chain waveguides of different lengths: estimation of*

waveguide loss, Appl. Phys. Lett. **81**, 1714 (2002).

[36] S. A. Maier, P. G. Kik, H. A. Atwater, S. Meltzer, E. Harel, B. E. Koel, and A. A. Requicha, *Local detection of electromagnetic energy transport below the diffraction limit in metal nanoparticle plasmon waveguides*, Nature Mater. **2**, 229 (2003).

[37] J. A. Dionne, L. A. Sweatlock, H. A. Atwater, and A. Polman, *Planar metal plasmon waveguides: frequency-dependent dispersion, propagation, localization, and loss beyond the free electron model*, Phys. Rev. B **72**, 075405 (2005).

[38] H. T. Miyazaki and Y. Kurokawa, *Squeezing visible light waves into a 3-nm-thick and 55-nm-long plasmon cavity*, Phys. Rev. Lett. **96**, 097401 (2006).

[39] S. P. Burgos, R. de Waele, A. Polman, and H. A. Atwater, *A single-layer wide-angle negative-index metamaterial at visible frequencies*, Nature Mater. **9**, 407 (2010).

[40] G. Dolling, C. Enkrich, M. Wegener, C. M. Soukoulis, and S. Linden, *Simultaneous negative phase and group velocity of light in a metamaterial*, Science **312**, 892 (2006).

[41] H. J. Lezec, J. A. Dionne, and H. A. Atwater, *Negative refraction at visible frequencies*, Science **316**, 430 (2007).

[42] J. B. Pendry, *Negative refraction makes a perfect lens*, Phys. Rev. Lett. **85**, 3966 (2000).

[43] E. Verhagen, R. de Waele, L. Kuipers, and A. Polman, *Three-dimensional negative index of refraction at optical frequencies by coupling plasmonic waveguides*, Phys. Rev. Lett. **105**, 223901 (2010).

[44] S. Xiao, V. P. Drachev, A. V. Kildishev, X. Ni, U. K. Chettiar, H.-K. Yuan, and V. M. Shalaev, *Loss-free and active optical negative-index metamaterials*, Nature **466**, 735 (2010).

[45] J. Yao, Z. Liu, Y. Liu, Y. Wang, C. Sun, G. Bartal, A. M. Stacy, and X. Zhang, *Optical negative refraction in bulk metamaterials of nanowires*, Science **321**, 930 (2008).

[46] J. Dintinger, S. Klein, F. Bustos, W. L. Barnes, and T. W. Ebbesen, *Strong coupling between surface plasmon-polaritons and organic molecules in subwavelength hole arrays*, Phys. Rev. B **71**, 035424 (2005).

[47] E. Feigenbaum and M. Orenstein, *Ultrasmall volume plasmons, yet with complete retardation effects*, Phys. Rev. Lett. **101**, 163902 (2008).

[48] D. K. Gramotnev, *Adiabatic nanofocusing of plasmons by sharp metallic grooves: geometrical optics approach*, J. Appl. Phys. **98**, 104302 (2005).

[49] S. A. Maier, *Plasmonic eld enhancement and SERS in the effective mode volume picture*, Opt. Express **14**, 1957 (2006).

[50] S. A. Maier, *Effective mode volume of nanoscale plasmon cavities*, Opt. Quantum. Electron. **38**, 257 (2006).

[51] E. Verhagen, L. Kuipers, and A. Polman, *Enhanced nonlinear optical effects with a tapered plasmonic waveguide*, Nano Lett. **7**, 334 (2007).

[52] V. S. Volkov, S. I. Bozhevolnyi, S. G. Rodrigo, L. Martín-Moreno, F. J. García-Vidal, E. Devaux, and T. W. Ebbesen, *Nanofocusing with channel plasmon polaritons*, Nano Lett. **9**, 1278 (2009).

[53] M. Schnell, P. Alonso-Gonzalez, L. Arzubiaga, F. Casanova, L. E. Hueso, A. Chuvilin, and R. Hillenbrand, *Nanofocusing of mid-infrared energy with tapered transmission lines*, Nature Phot. **5**, 283 (2011).

[54] G. Della Valle, T. Søndergaard, and S. I. Bozhevolnyi, *Plasmon-polariton nano-stripresonators: from visible to infra-red*, Opt. Express **16**, 6867 (2008).

[55] E. S. Barnard, J. S. White, A. Chandran, and M. L. Brongersma, *Spectral properties of plasmonic resonator antennas*, Opt. Express **16**, 16529 (2008).

[56] H. Ditlbacher, A. Hohenau, D. Wagner, U. Kreibig, M. Rogers, F. Hofer, F. R. Aussenegg, and J. R. Krenn, *Silver nanowires as surface plasmon resonators*, Phys. Rev. Lett. **95**,

257403 (2005).

[57] J. Li and N. Engheta, *Subwavelength plasmonic cavity resonator on a nanowire with periodic permittivity variation*, Phys. Rev. B **74**, 115125 (2006).

[58] E. J. R. Vesseur, R. de Waele, M. Kuttge, and A. Polman, *Direct observation of plasmonic modes in Au nanowires using high-resolution cathodoluminescence spectroscopy*, Nano Lett. **7**, 2843 (2007).

[59] Y. Kurokawa and H. T. Miyazaki, *Metal-insulator-metal plasmon nanocavities: analysis of optical properties*, Phys. Rev. B **75**, 035411 (2007).

[60] R. Cole, J. Baumberg, F. García de Abajo, S. Mahajan, M. Abdelsalam, and P. Bartlett, *Understanding plasmons in nanoscale voids*, Nano Lett. **7**, 2094 (2007).

[61] R. M. Cole, Y. Sugawara, J. J. Baumberg, S. Mahajan, M. Abdelsalam, and P. N. Bartlett, *Easily coupled whispering gallery plasmons in dielectric nanospheres embedded in gold lms*, Phys. Rev. Lett. **97**, 137401 (2006).

[62] J. J. Penninkhof, L. A. Sweatlock, A. Moroz, H. A. Atwater, A. van Blaaderen, and A. Polman, *Optical cavity modes in gold shell colloids*, J. Appl. Phys. **103**, 123105 (2008).

[63] B. Auguié and W. L. Barnes, *Collective resonances in gold nanoparticle arrays*, Phys. Rev. Lett. **101**, 143902 (2008).

[64] L. A. Sweatlock, S. A. Maier, H. A. Atwater, J. J. Penninkhof, and A. Polman, *Highly con ned electromagnetic elds in arrays of strongly coupled Ag nanoparticles*, Phys. Rev. B **71**, 235408 (2005).

[65] N. Talebi, A. Mahjoubfar, and M. Shahabadi, *Plasmonic ring resonator*, J. Opt. Soc. Am. B **25**, 2116 (2008).

[66] L. Novotny and N. van Hulst, *Antennas for light*, Nature Phot. **5**, 83 (2011).

[67] S. Kim, J. Jin, Y.-J. Kim, I.-Y. Park, Y. Kim, and S.-W. Kim, *High-harmonic generation by resonant plasmon eld enhancement*, Nature **453**, 757 (2008).

[68] J. A. H. van Nieuwstadt, M. Sandtke, R. H. Harmsen, F. B. Segerink, J. C. Prangsma, S. Enoch, and L. Kuipers, *Strong modi cation of the nonlinear optical response of metallic subwavelength hole arrays*, Phys. Rev. Lett. **97**, 146102 (2006).

[69] J. Renger, R. Quidant, N. van Hulst, and L. Novotny, *Surface-enhanced nonlinear four-wave mixing*, Phys. Rev. Lett. **104**, 046803 (2010).

[70] E. Verhagen, L. Kuipers, and A. Polman, *Field enhancement in metallic subwavelength aperture arrays probed by erbium upconversion luminescence*, Opt. Express **17**, 14586 (2009).

[71] T. Kosako, Y. Kadoya, and H. F. Hofmann, *Directional control of light by a nano-optical Yagi-Uda antenna*, Nature Phot. **4**, 312 (2010).

[72] R. de Waele, A. Koenderink, and A. Polman, *Tunable nanoscale localization of energy on plasmon particle arrays*, Nano Lett. **7**, 2004 (2007).

[73] A. G. Curto, G. Volpe, T. H. Taminiau, M. P. Kreuzer, R. Quidant, and N. F. van Hulst, *Unidirectional emission of a quantum dot coupled to a nanoantenna*, Science **329**, 930 (2010).

[74] P. Anger, P. Bharadwaj, and L. Novotny, *Enhancement and quenching of single-molecule uorescence*, Phys. Rev. Lett. **96**, 113002 (2006).

[75] J. N. Farahani, D. W. Pohl, H.-J. Eisler, and B. Hecht, *Single quantum dot coupled to a scanning optical antenna: a tunable superemitter*, Phys. Rev. Lett. **95**, 017402 (2005).

[76] Y. Fedutik, V. V. Temnov, O. Schöps, U. Woggon, and M. V. Artemyev, *Exciton-plasmon-photon conversion in plasmonic nanostructures*, Phys. Rev. Lett. **99**, 136802 (2007).

[77] V. Giannini and J. A. Sánchez-Gil, *Excitation and emission enhancement of single molecule uorescence through multiple surface-plasmon resonances on metal trimer*

nanoantennas, Opt. Lett. **33**, 899 (2008).

[78] A. Kinkhabwala, Z. Yu, S. Fan, Y. Avlasevich, K. Mullen, and M. W. E., *Large single-molecule uorescence enhancements produced by a bowtie nanoantenna*, Nature Phot. **3**, 654 (2009).

[79] E. J. A. Kroekenstoel, E. Verhagen, R. J. Walters, L. Kuipers, and A. Polman, *Enhanced spontaneous emission rate in annular plasmonic nanocavities*, Appl. Phys. Lett. **95**, 263106 (2009).

[80] H. Mertens, J. S. Biteen, H. A. Atwater, and A. Polman, *Polarization-selective plasmon-enhanced silicon quantum-dot luminescence*, Nano Lett. **6**, 2622 (2006).

[81] H. Mertens, A. F. Koenderink, and A. Polman, *Plasmon-enhanced luminescence near noble-metal nanospheres: comparison of exact theory and an improved Gersten and Nitzan model*, Phys. Rev. B **76**, 115123 (2007).

[82] O. Muskens, V. Giannini, J. Sánchez-Gil, and J. Gómez-Rivas, *Strong enhancement of the radiative decay rate of emitters by single plasmonic nanoantennas*, Nano Lett. **7**, 2871 (2007).

[83] M. Ringler, A. Schwemer, M. Wunderlich, A. Nichtl, K. Kurzinger, T. A. Klar, and J. Feldmann, *Shaping emission spectra of uorescent molecules with single plasmonic nanoresonators*, Phys. Rev. Lett. **100**, 203002 (2008).

[84] A. Trügler and U. Hohenester, *Strong coupling between a metallic nanoparticle and a single molecule*, Phys. Rev. B **77**, 115403 (2008).

[85] J. Wenger, D. Gérard, J. Dintinger, O. Mahboub, N. Bonod, E. Popov, T. W. Ebbesen, and H. Rigneault, *Emission and excitation contributions to enhanced single molecule uorescence by gold nanometric apertures*, Opt. Express **16**, 3008 (2008).

[86] F. De Angelis, M. Patrini, G. Das, I. Maksymov, M. Galli, L. Businaro, L. C. Andreani, and E. Di Fabrizio, *A hybrid plasmonic-photonic nanodevice for label-free detection of a few molecules*, Nano Lett. **8**, 2321 (2008).

[87] F. Neubrech, A. Pucci, T. W. Cornelius, S. Karim, A. García-Etxarri, and J. Aizpurua, *Resonant plasmonic and vibrational coupling in a tailored nanoantenna for infrared detection*, Phys. Rev. Lett. **101**, 157403 (2008).

[88] L. Tang, S. E. Kocabas, S. Latif, A. K. Okyay, D.-S. Ly-Gagnon, K. C. Saraswat, and D. A. B. Miller, *Nanometre-scale germanium photodetector enhanced by a near-infrared dipole antenna*, Nature Phot. **2**, 226 (2008).

[89] M. W. Knight, H. Sobhani, P. Nordlander, and N. J. Halas, *Photodetection with active optical antennas*, Science **332**, 702 (2011).

[90] K. R. Catchpole and A. Polman, *Design principles for particle plasmon enhanced solar cells*, Appl. Phys. Lett. **93**, 191113 (2008).

[91] N. C. Lindquist, W. A. Luhman, S.-H. Oh, and R. J. Holmes, *Plasmonic nanocavity arrays for enhanced ef ciency in organic photovoltaic cells*, Appl. Phys. Lett. **93**, 123308 (2008).

[92] K. Nakayama, K. Tanabe, and H. A. Atwater, *Plasmonic nanoparticle enhanced light absorption in GaAs solar cells*, Appl. Phys. Lett. **93**, 121904 (2008).

[93] H. Eghlidi, K. G. Lee, X.-W. Chen, S. Götzinger, and V. Sandoghdar, *Resolution and enhancement in nanoantenna-based uorescence microscopy*, Nano Lett. **9**, 4007 (2009).

[94] T. Kalkbrenner, U. Håkanson, A. Schädle, S. Burger, C. Henkel, and V. Sandoghdar, *Optical microscopy via spectral modi cations of a nanoantenna*, Phys. Rev. Lett. **95**, 200801 (2005).

[95] T. Taubner, D. Korobkin, Y. Urzhumov, G. Shvets, and R. Hillenbrand, *Near- eld*

microscopy through a SiC superlens, Science **313**, 1595 (2006).

[96] C. Loo, A. Lowery, N. Halas, J. West, and R. Drezek, *Immunotargeted nanoshells for integrated cancer imaging and therapy*, Nano Lett. **5**, 709 (2005).

[97] Y. Fu and N. K. A. Bryan, *Investigation of physical properties of quartz after focused ion beam bombardment*, Appl. Phys. B **80**, 581 (2005).

[98] K. Zinoviev, C. Dominguez, and A. Vilà, *Diffraction grating couplers milled in Si_3N_4 rib waveguides with a focused ion beam*, Opt. Express **13**, 8618 (2005).

[99] J. Schrauwen, D. V. Thourhout, and R. Baets, *Focused-ion-beam fabricated vertical ber couplers on silicon-on-insulator waveguides*, Appl. Phys. Lett. **89**, 141102 (2006).

[100] R. de Waele, *Controlling light with resonant plasmonic nanostructures*, PhD thesis, FOM Institute for Atomic and Molecular Physics (AMOLF), Utrecht University, 2009.

[101] M. Hegner, P. Wagner, and G. Semenza, *Ultralarge atomically at template-stripped Au surfaces for scanning probe microscopy*, Surf. Sci. **291**, 39 (1993).

[102] U. Höpfner, H. Hehl, and L. Brehmer, *Preparation of ordered thin gold lms*, Applied Surface Science **152**, 259 (1999).

[103] P. Nagpal, N. C. Lindquist, S.-H. Oh, and D. J. Norris, *Ultrasmooth patterned metals for plasmonics and metamaterials*, Science **325**, 594 (2009).

[104] P. Wagner, M. Hegner, H.-J. Guentherodt, and G. Semenza, *Formation and in situ modi cation of monolayers chemisorbed on ultra at template-stripped gold surfaces*, Langmuir **11**, 3867 (1995).

[105] E. Betzig and J. K. Trautman, *Near- eld optics: microscopy, spectroscopy, and surface modi cation beyond the diffraction limit*, Science **257**, 189 (1992).

[106] A. F. Koenderink, M. Kafesaki, B. C. Buchler, and V. Sandoghdar, *Controlling the resonance of a photonic crystal microcavity by a near- eld probe*, Phys. Rev. Lett. **95**, 153904 (2005).

[107] F. J. García de Abajo, *Optical excitations in electron microscopy*, Rev. Mod. Phys. **82**, 209 (2010).

[108] E. A. Stern, *Transition radiation from metal lms*, Phys. Rev. Lett. **8**, 7 (1962).

[109] M. Kuttge, E. J. R. Vesseur, A. F. Koenderink, H. J. Lezec, H. A. Atwater, F. J. G. de Abajo, and A. Polman, *Local density of states, spectrum, and far- eld interference of surface plasmon polaritons probed by cathodoluminescence*, Phys. Rev. B **79**, 113405 (2009).

[110] R. H. Ritchie, *Plasma losses by fast electrons in thin lms*, Phys. Rev. **106**, 874 (1957).

[111] Y.-Y. Teng and E. A. Stern, *Plasma radiation from metal grating surfaces*, Phys. Rev. Lett. **19**, 511 (1967).

[112] D. Heitmann, *Radiative decay of surface plasmons excited by fast electrons on periodically modulated silver surfaces*, J. Phys. C: Solid State Phys. **10**, 397 (1977).

[113] J. T. van Wijngaarden, E. Verhagen, A. Polman, C. E. Ross, H. J. Lezec, and H. A. Atwater, *Direct imaging of propagation and damping of near-resonance surface plasmon polaritons using cathodoluminescence spectroscopy*, Appl. Phys. Lett. **88**, 221111 (2006).

[114] M. Bashevoy, F. Jonsson, A. Krasavin, N. Zheludev, Y. Chen, and M. Stockman, *Generation of traveling surface plasmon waves by free-electron impact*, Nano Lett. **6**, 1113 (2006).

[115] N. Yamamoto, K. Araya, and F. J. García de Abajo, *Photon emission from silver particles induced by a high-energy electron beam*, Phys. Rev. B **64**, 205419 (2001).

[116] W. Drachsel, M. Adelt, N. Nilius, and H. J. Freund, *Cathodoluminescence of small silver particles on Al_2O_3/NiAl (110)*, J. Electron Spectrosc. Relat. Phenom. **122**, 239 (2002).

[117] C. E. Hofmann, E. J. R. Vesseur, L. A. Sweatlock, H. J. Lezec, F. J. García de Abajo,

A. Polman, and H. A. Atwater, *Plasmonic modes of annular nanoresonators imaged by spectrally resolved cathodoluminescence*, Nano Lett. **7**, 3612 (2007).

[118] P. Chaturvedi, K. H. Hsu, A. Kumar, K. H. Fung, J. C. Mabon, and N. X. Fang, *Imaging of plasmonic modes of silver nanoparticles using high-resolution cathodoluminescence spectroscopy*, ACS Nano **3**, 2965 (2009).

[119] M. Kuttge, F. J. García de Abajo, and A. Polman, *Ultrasmall mode volume plasmonic nanodisk resonators*, Nano Lett. **10**, 1537 (2010).

[120] X. L. Zhu, Y. Ma, J. S. Zhang, J. Xu, X. F. Wu, Y. Zhang, X. B. Han, Q. Fu, Z. M. Liao, L. Chen, and D. P. Yu, *Con ned three-dimensional plasmon modes inside a ring-shaped nanocavity on a silver lm imaged by cathodoluminescence microscopy*, Phys. Rev. Lett. **105**, 127402 (2010).

[121] G. Laurent, N. Felidj, J. Aubard, G. Levi, J. R. Krenn, A. Hohenau, G. Schider, A. Leitner, and F. R. Aussenegg, *Evidence of multipolar excitations in surface enhanced Raman scattering*, Phys. Rev. B **71**, 045430 (2005).

[122] K. Imura, T. Nagahara, and H. Okamoto, *Near- eld optical imaging of plasmon modes in gold nanorods*, J. Chem. Phys. **122**, 154701 (2005).

[123] C. Girard and A. Dereux, *Optical spectroscopy of a surface at the nanometer scale: a theoretical study in real space*, Phys. Rev. B **49**, 11344 (1994).

[124] J. Nelayah, M. Kociak, O. Stephan, F. J. García de Abajo, M. Tence, L. Henrard, D. Taverna, I. Pastoriza-Santos, L. M. Liz-Marzán, and C. Colliex, *Mapping surface plasmons on a single metallic nanoparticle*, Nature Phys. **3**, 348 (2007).

[125] M. Bosman, V. J. Keast, M. Watanabe, A. I. Maaroof, and M. B. Cortie, *Mapping surface plasmons at the nanometre scale with an electron beam*, Nanotechnology **18**, 165505 (2007).

[126] H. J. Lezec, A. Degiron, E. Devaux, R. A. Linke, L. Martin-Moreno, F. J. Garcia-Vidal, and T. W. Ebbesen, *Beaming light from a subwavelength aperture*, Science **297**, 820 (2002).

[127] C. A. Volkert and A. M. Minor, *Focused ion beam microscopy and micromachining*, MRS Bull. **32**, 389 (2007).

[128] F. J. García de Abajo and A. Howie, *Relativistic electron energy loss and electron-induced photon emission in inhomogeneous dielectrics*, Phys. Rev. Lett. **80**, 5180 (1998).

[129] F. J. García de Abajo, *Relativistic energy loss and induced photon emission in the interaction of a dielectric sphere with an external electron beam*, Phys. Rev. B **59**, 3095 (1999).

[130] N. Yamamoto, M. Nakano, and T. Suzuki, *Light emission by surface plasmons on nanostructures of metal surfaces induced by high-energy electron beams*, Surf. Interface Anal. **38**, 1725 (2006).

[131] M. Bosman, M. Watanabe, D. Alexander, and V. Keast, *Mapping chemical and bonding information using multivariate analysis of electron energy-loss spectrum images*, Ultramicroscopy **106**, 1024 (2006).

[132] E. R. Malinowski, *Factor analysis in chemistry*, Wiley, 1991.

[133] N. Yamamoto, H. Sugiyama, and A. Toda, *Cherenkov and transition radiation from thin plate crystals detected in the transmission electron microscope*, Proc. R. Soc. A **452**, 2279 (1996).

[134] J.-C. Weeber, J. R. Krenn, A. Dereux, B. Lamprecht, Y. Lacroute, and J. P. Goudonnet, *Near- eld observation of surface plasmon polariton propagation on thin metal stripes*, Phys. Rev. B **64**, 045411 (2001).

[135] D. J. Bergman and M. I. Stockman, *Surface plasmon ampli cation by stimulated emission of radiation: quantum generation of coherent surface plasmons in nanosystems*,

Phys. Rev. Lett. **90**, 027402 (2003).
[136] J. Jackson, *Classical electrodynamics*, Wiley, New York, 1999.
[137] T. A. Kelf, Y. Sugawara, J. J. Baumberg, M. Abdelsalam, and P. N. Bartlett, *Plasmonic band gaps and trapped plasmons on nanostructured metal surfaces*, Phys. Rev. Lett. **95**, 116802 (2005).
[138] B. Min, E. Ostby, V. Sorger, E. Ulin-Avila, L. Yang, X. Zhang, and K. Vahala, *High-Q surface-plasmon-polariton whispering-gallery microcavity*, Nature **457**, 455 (2008).
[139] K. C. Vernon, D. K. Gramotnev, and D. F. P. Pile, *Channel plasmon-polariton modes in V grooves lled with dielectric*, J. Appl. Phys. **103**, 034304 (2008).
[140] F. J. García de Abajo and A. Howie, *Retarded eld calculation of electron energy loss in inhomogeneous dielectrics*, Phys. Rev. B **65**, 115418 (2002).
[141] Y. Alaverdyan, B. Sepúlveda, L. Eurenius, E. Olsson, and M. Käll, *Optical antennas based on coupled nanoholes in thin metal lms*, Nature Phys. **3**, 884 (2007).
[142] K. Drexhage, *In uence of a dielectric interface on uorescence decay time*, J. Lumin. **1,2**, 693 (1970).
[143] E. Purcell, *Spontaneous emission probabilities at radio frequencies*, Phys. Rev. **69**, 681 (1946).
[144] M. L. Gorodetsky, A. A. Savchenkov, and V. S. Ilchenko, *Ultimate Q of optical microsphere resonators*, Opt. Lett. **21**, 453 (1996).
[145] D. W. Vernooy, V. S. Ilchenko, H. Mabuchi, E. W. Streed, and H. J. Kimble, *High-Q measurements of fused-silica microspheres in the near infrared*, Opt. Lett. **23**, 247 (1998).
[146] J. M. Gérard, B. Sermage, B. Gayral, B. Legrand, E. Costard, and V. Thierry-Mieg, *Enhanced spontaneous emission by quantum boxes in a monolithic optical microcavity*, Phys. Rev. Lett. **81**, 1110 (1998).
[147] M. Pelton, J. Vukovic, G. S. Solomon, A. Scherer, and Y. Yamamoto, *Three-dimensionally con ned modes in micropost microcavities: quality factors and Purcell factors*, IEEE J. Quantum. Electron. **38**, 170 (2002).
[148] D. K. Armani, T. J. Kippenberg, S. M. Spillane, and K. J. Vahala, *Ultra-high-Q toroid microcavity on a chip*, Nature **421**, 925 (2003).
[149] B. Gayral, J. M. Gérard, A. Lemaître, C. Dupuis, L. Manin, and J. L. Pelouard, *High-Q wet-etched GaAs microdisks containing InAs quantum boxes*, Appl. Phys. Lett. **75**, 1908 (1999).
[150] D. Englund, D. Fattal, E. Waks, G. Solomon, B. Zhang, T. Nakaoka, Y. Arakawa, Y. Yamamoto, and J. Vucković, *Controlling the spontaneous emission rate of single quantum dots in a two-dimensional photonic crystal*, Phys. Rev. Lett. **95**, 013904 (2005).
[151] P. Velha, E. Picard, T. Charvolin, E. Hadji, J. Rodier, P. Lalanne, and D. Peyrade, *Ultra-High Q/V Fabry-Perot microcavity on SOI substrate*, Opt. Express **15**, 16090 (2007).
[152] H. Altug, D. Englund, and J. Vuckovic, *Ultrafast photonic crystal nanocavity laser*, Nature Phys. **2**, 484 (2006).
[153] S. Noda, M. Fujita, and T. Asano, *Spontaneous-emission control by photonic crystals and nanocavities*, Nature Phot. **1**, 449 (2007).
[154] A. Hryciw, Y. C. Jun, and M. L. Brongersma, *Plasmon-enhanced emission from optically-doped MOS light sources*, Opt. Express **17**, 185 (2009).
[155] Y. Gong and J. Vucković, *Design of plasmon cavities for solid-state cavity quantum electrodynamics applications*, Appl. Phys. Lett. **90**, 033113 (2007).
[156] M. Kuttge, E. J. R. Vesseur, and A. Polman, *Fabry–Pérot resonators for surface plasmon*

polaritons probed by cathodoluminescence, Appl. Phys. Lett. **94**, 183104 (2009).

[157] P. B. Johnson and R. W. Christy, *Optical constants of the noble metals*, Phys. Rev. B **6**, 4370 (1972).

[158] R. de Waele, unpublished.

[159] R. J. Walters, R. V. A. van Loon, I. Brunets, J. Schmitz, and A. Polman, *A silicon-based electrical source of surface plasmon polaritons*, Nature Mater. **9**, 21 (2010).

[160] S. I. Bozhevolnyi, *Effective-index modeling of channel plasmon polaritons*, Opt. Express **14**, 9467 (2006).

[161] R. Ruppin, *Electromagnetic energy density in a dispersive and absorptive material*, Phys. Lett. A **299**, 309 (2002).

[162] R. R. Chance, A. Prock, and R. Silbey, *Molecular uorescence and energy transfer near interfaces*, Adv. Chem. Phys. **37**, 1 (1978).

[163] J. Kalkman, H. Gersen, L. Kuipers, and A. Polman, *Excitation of surface plasmons at a SiO_2/Ag interface by silicon quantum dots: experiment and theory*, Phys. Rev. B **73**, 075317 (2006), `http://www.amolf.nl/download/dipolecalc/`.

[164] T. J. Kippenberg, A. L. Tchebotareva, J. Kalkman, A. Polman, and K. J. Vahala, *Purcell-factor-enhanced scattering from Si nanocrystals in an optical microcavity*, Phys. Rev. Lett. **103**, 027406 (2009).

[165] P. Bharadwaj, B. Deutsch, and L. Novotny, *Optical antennas*, Adv. Opt. Photon. **1**, 438 (2009).

[166] G. Vecchi, V. Giannini, and J. G. Rivas, *Shaping the uorescent emission by lattice resonances in plasmonic crystals of nanoantennas*, Phys. Rev. Lett. **102**, 146807 (2009).

[167] H. Mertens, *Controlling plasmon-enhanced luminescence*, PhD thesis, FOM Institute for Atomic and Molecular Physics (AMOLF), Utrecht University, 2007.

[168] J. Krenn, G. Schider, W. Rechberger, B. Lamprecht, A. Leitner, and F. Aussenegg, *Design of multipolar plasmon excitations in silver nanoparticles*, Appl. Phys. Lett. **77**, 3379 (2000).

[169] L. Novotny, *Effective wavelength scaling for optical antennas*, Phys. Rev. Lett. **98**, 266802 (2007).

[170] P. Mühlschlegel, H. J. Eisler, O. J. F. Martin, B. Hecht, and D. W. Pohl, *Resonant optical antennas*, Science **308**, 1607 (2005).

[171] O. L. Muskens, V. Giannini, J. A. Sánchez-Gil, and J. G. Rivas, *Optical scattering resonances of single and coupled dimer plasmonic nanoantennas*, Opt. Express **15**, 17736 (2007).

[172] P. Ghenuche, S. Cherukulappurath, T. H. Taminiau, N. F. van Hulst, and R. Quidant, *Spectroscopic mode mapping of resonant plasmon nanoantennas*, Phys. Rev. Lett. **101**, 116805 (2008).

[173] M.-W. Chu, V. Myroshnychenko, C. H. Chen, J.-P. Deng, C.-Y. Mou, and F. J. García de Abajo, *Probing bright and dark surface-plasmon modes in individual and coupled noble metal nanoparticles using an electron beam*, Nano Lett. **9**, 399 (2009).

[174] J.-S. Huang, J. Kern, P. Geisler, P. Weinmann, M. Kamp, A. Forchel, P. Biagioni, and B. Hecht, *Mode imaging and selection in strongly coupled nanoantennas*, Nano Lett. **10**, 2105 (2010).

[175] J. J. Penninkhof, *Tunable plasmon resonances in anisotropic metal nanostructures*, PhD thesis, FOM Institute for Atomic and Molecular Physics (AMOLF), Utrecht University, 2006.

[176] S. Bidault, F. J. García de Abajo, and A. Polman, *Plasmon-based nanolenses assembled on a well-de ned DNA template*, J. Am. Chem. Soc. **130**, 2750 (2008).

[177] U. Fano, *Effects of con guration interaction on intensities and phase shifts*, Phys. Rev. **124**, 1866 (1961).

[178] B. Luk yanchuk, N. I. Zheludev, S. A. Maier, N. J. Halas, P. Nordlander, H. Giessen, and C. T. Chong, *The Fano resonance in plasmonic nanostructures and metamaterials*, Nature Mater. **9**, 707 (2010).

[179] E. R. Encina and E. A. Coronado, *Plasmonic nanoantennas: angular scattering properties of multipole resonances in noble metal nanorods*, J. Phys. Chem. C **112**, 9586 (2008).

[180] O. Schmidt, M. Bauer, C. Wiemann, R. Porath, M. Scharte, O. Andreyev, G. Schönhense, and M. Aeschlimann, *Time-resolved two photon photoemission electron microscopy*, Appl. Phys. B: Lasers Opt. **74**, 223 (2002).

[181] M. Bauer, C. Wiemann, J. Lange, D. Bayer, M. Rohmer, and M. Aeschlimann, *Phase propagation of localized surface plasmons probed by time-resolved photoemission electron microscopy*, Appl. Phys. A: Mater. Sci. Process. **88**, 473 (2007).

[182] A. Gloskovskii, D. A. Valdaitsev, M. Cinchetti, S. A. Nepijko, J. Lange, M. Aeschlimann, M. Bauer, M. Klimenkov, L. V. Viduta, P. M. Tomchuk, and G. Schönhense, *Electron emission from lms of Ag and Au nanoparticles excited by a femtosecond pump-probe laser*, Phys. Rev. B **77**, 195427 (2008).

[183] M. Silveirinha and N. Engheta, *Tunneling of electromagnetic energy through subwavelength channels and bends using ϵ-near-zero materials*, Phys. Rev. Lett. **97**, 157403 (2006).

[184] B. Edwards, A. Alù, M. E. Young, M. Silveirinha, and N. Engheta, *Experimental veri cation of epsilon-near-zero metamaterial coupling and energy squeezing using a microwave waveguide*, Phys. Rev. Lett. **100**, 033903 (2008).

[185] A. Alù and N. Engheta, *Light squeezing through arbitrarily shaped plasmonic channels and sharp bends*, Phys. Rev. B **78**, 035440 (2008).

[186] M. T. Hill, M. Marell, E. S. P. Leong, B. Smalbrugge, Y. Zhu, M. Sun, P. J. van Veldhoven, E. J. Geluk, F. Karouta, Y.-S. Oei, R. Nötzel, C.-Z. Ning, and M. K. Smit, *Lasing in metal-insulator-metal sub-wavelength plasmonic waveguides*, Opt. Express **17**, 11107 (2009).

[187] R. F. Oulton, V. J. Sorger, T. Zentgraf, R.-M. Ma, C. Gladden, L. Dai, G. Bartal, and X. Zhang, *Plasmon lasers at deep subwavelength scale*, Nature **461**, 629 (2009).

[188] F. Baida, D. Van Labeke, G. Granet, A. Moreau, and A. Belkhir, *Origin of the super-enhanced light transmission through a 2-D metallic annular aperture array: a study of photonic bands*, Appl. Phys. B: Lasers Opt. **79**, 1 (2004).

[189] S. M. Orbons and A. Roberts, *Resonance and extraordinary transmission in annular aperture arrays*, Opt. Express **14**, 12623 (2006).

[190] M. I. Haftel, C. Schlockermann, and G. Blumberg, *Enhanced transmission with coaxial nanoapertures: role of cylindrical surface plasmons*, Phys. Rev. B **74**, 235405 (2006).

[191] M. Kuttge, W. Cai, F. J. García de Abajo, and A. Polman, *Dispersion of metal-insulator-metal plasmon polaritons probed by cathodoluminescence imaging spectroscopy*, Phys. Rev. B **80**, 033409 (2009).

[192] K. A. Willets and R. P. Van Duyne, *Localized surface plasmon resonance spectroscopy and sensing*, Annu. Rev. Phys. Chem. **58**, 267 (2007).

[193] B. Sepúlveda, P. C. Angelomé, L. M. Lechuga, and L. M. Liz-Marzán, *LSPR-based nanobiosensors*, Nano Today **4**, 244 (2009).

[194] R. J. Walters, personal communication.

[195] C. L. Nehl, H. Liao, and J. H. Hafner, *Optical properties of star-shaped gold nanoparticles*, Nano Lett. **6**, 683 (2006).

[196] J. N. Anker, W. P. Hall, O. Lyandres, N. C. Shah, J. Zhao, and R. P. Van Duyne, *Biosensing with plasmonic nanosensors*, Nature Mater. **7**, 442 (2008).

[197] R. Ameling, L. Langguth, M. Hentschel, M. Mesch, P. V. Braun, and H. Giessen, *Cavity-enhanced localized plasmon resonance sensing*, Appl. Phys. Lett. **97**, 253116 (2010).

[198] R.-M. Ma, R. F. Oulton, V. J. Sorger, G. Bartal, and X. Zhang, *Room-temperature sub-diffraction-limited plasmon laser by total internal re ection*, Nature Mater. **10**, 110 (2011).

[199] T. Virgili, D. G. Lidzey, D. D. C. Bradley, G. Cerullo, S. Stagira, and S. D. Silvestri, *An ultrafast spectroscopy study of stimulated emission in poly(9,9-dioctyl uorene) lms and microcavities*, Appl. Phys. Lett. **74**, 2767 (1999).

[200] U. Scherf, S. Riechel, U. Lemmer, and R. F. Mahrt, *Conjugated polymers: lasing and stimulated emission*, Curr. Opin. Solid State Mater. Sci. **5**, 143 (2001).

[201] G. Heliotis, D. D. C. Bradley, G. A. Turnbull, and I. D. W. Samuel, *Light ampli cation and gain in poly uorene waveguides*, Appl. Phys. Lett. **81**, 415 (2002).

[202] D. O Carroll, I. Lieberwirth, and G. Redmond, *Microcavity effects and optically pumped lasing in single conjugated polymer nanowires*, Nature Nano. **2**, 180 (2007).

[203] M. Suchanska, *Ion-induced photon emission of metals*, Prog. Surf. Sci. **54**, 165 (1997).

[204] M. E. Hoenk and K. J. Vahala, *Cathodoluminescence system for a scanning electron microscope using an optical ber for light collection*, Rev. Sci. Instrum. **60**, 226 (1989).

[205] C. Lu, M. Dorian, M. Tabei, and A. Elsea, *End point detection in ion milling processes by sputter-induced optical emission spectroscopy*, J. Vac. Sci. Technol. A **2**, 481 (1984).

[206] B. W. Ward, M. Ward, D. Edwards, and N. P. Economou, *Focused ion beam induced optical emission spectroscopy*, J. Vac. Sci. Technol. B **6**, 2100 (1988).

[207] X. Bendaña, A. Polman, and F. J. García de Abajo, *Single-photon generation by electron beams*, Nano Lett. (2010), accepted.

[208] Knill, *A scheme for ef cient quantum computation with linear optics*, Nature **409**, 46 (2001).

[209] P. Kok, W. J. Munro, K. Nemoto, T. C. Ralph, J. P. Dowling, and G. J. Milburn, *Linear optical quantum computing with photonic qubits*, Rev. Mod. Phys. **79**, 135 (2007).

[210] S. J. Smith and E. M. Purcell, *Visible Light from Localized Surface Charges Moving across a Grating*, Phys. Rev. **92**, 1069 (1953).

Summary

Light can be guided along the surface of a metal in the form of surface plasmon polaritons (SPPs). SPPs are oscillations in the free electron plasma density at optical frequencies that propagate over the surface as waves. These waves are characterized by a special dispersion, enabling short wavelengths, tight confinement and the manipulation of light at the nanoscale. Plasmonic nanoantennas are resonators for surface plasmons that provide coupling of the far field to a nanoscale volume with interesting applications both in receiving and transmitting mode. The use of these antennas in future devices relies on strong control over the resonant plasmonic field distribution at the nanoscale.

In this thesis we present how the dispersion and confinement of resonances in plasmonic nanoantennas are resolved at the nanoscale, and how the dispersion and confinement are further engineered by tuning the metal geometry.

Fabrication of nanostructures is done using focused-ion-beam milling (FIB) in metallic surfaces. We demonstrate that patterning in single-crystal substrates allows us to precisely control the geometry in which plasmons are confined.

The nanoscale properties of the resonant plasmonic fields are resolved using a new technique developed in this thesis: angle- and polarization controlled cathodoluminescence (CL) imaging spectroscopy. With this technique, a tightly focused electron beam excites the plasmonic nanoantennas and the emitted CL spectrum carries the signature of the resonant modes. This allows us to probe the optical antenna properties with deep subwavelength resolution.

Chapter 2 presents experimental results on nanoantennas consisting of 500–1200-nm-long polycrystalline Au nanowires. The spatially-resolved CL emission reveals nodal patterns along the axis of the nanowires, which are attributed to standing plasmon waves. Multiple resonances were found with a different number of nodes. The measurement thus directly allows us to observe the plasmon wavelengths which we use to derive the dispersion relation of plasmons guided by the nanowire.

In chapter 3 we present a ridge-shaped nanoantenna with a length of 590 nm fabricated using FIB milling on a single-crystal Au substrate. The ridge is very smooth and demonstrates a level of control over the fabrication impossible with

polycrystalline metals. CL imaging spectroscopy is used to excite and image surface plasmons on the ridge. Principal component analysis reveals distinct plasmonic modes, which proves confinement of surface plasmon oscillations to the ridge. The data are confirmed by boundary-element-method (BEM) calculations of the plasmon field distribution on the ridge, which show that a propagating surface plasmon is confined to the top of the ridge, with a mode diameter <100 nm.

Chapter 4 presents a decomposition of the resonant modes in plasmonic whispering gallery cavities. Cavities consisting of a circular groove were fabricated using FIB milling of a single-crystal Au substrate. CL spectra emitted by these ring-shaped cavities show a distinct number of resonant peaks with a strong dependence on the cavity geometry. The measurements are compared to BEM calculations of the emission spectrum. We find an excellent agreement between theory and experiment. The calculations show that the different resonant peaks can be attributed to resonances with increasing azimuthal or radial order: the resonances are due to circulating plasmons that are confined to the groove. The smallest cavity fits only one wavelength in its circumference.

Chapter 5 presents a theoretical study of the plasmonic whispering gallery resonances, showing that small ring cavities enhance spontaneous emission over a broad spectral band. We calculate the quality factor Q and mode volume V for resonators with different groove shapes and ring radii. Quality factors range from 10–50 depending on geometry; mode volumes vary by a factor 30. The smallest mode volume was found to be $0.00073\,\lambda_0^3$ for a ring based on a 100-nm-deep, 10-nm-wide groove. Purcell factors well above 2000 are found in the energy range from E = 1.0–1.8 eV depending on the cavity geometry. For a given cavity, the Purcell enhancement is observed over a broad (50–100 meV) spectral range.

The antenna properties of the plasmonic whispering gallery cavities, both in receiving and transmitting mode, are further experimentally studied in chapter 6 using four complementary techniques. We show that far-field excitation selectively excites dipolar resonances leading to a Fano line shape in the scattering spectrum. In contrast, excitation by an electron beam allows to selectively excite modes with dipolar or quadrupolar symmetry. The orientation of the multipolar resonance is chosen by accurate positioning of the electron beam. We detect the corresponding angular emission distribution in the far field. Measurements of the fluorescence of dye molecules incorporated in the ring cavity shows reshaping of the fluorescence spectrum due to coupling of optically excited dye molecules to the cavity resonances. Finally, far-field excitation of the cavity resonances gives rise to photoelectron emission due to high field confinement in the groove of the ring resonator. Imaging the photoelectron emission provides one with an additional method to directly resolve the nanoscale dipolar field distribution.

Chapter 7 presents a plasmon resonator based on a metal-insulator-metal waveguide fabricated using a sequence of steps including FIB milling. In this waveguide we achieve an effective index of refraction equal to 0 by engineering the dispersion. Modes of the waveguides were excited using a 30 keV electron beam penetrating through the layer stack. From spatial maps of the emitted radiation we

directly observe the spatial mode profiles and we determine the dispersion relation of plasmon modes for a range of waveguide widths. At the cutoff frequency, the emission pattern corresponds to that of a line dipole antenna demonstrating the entire waveguide is in phase ($n = 0$). A strongly enhanced density of optical states is directly observed at cutoff from the enhanced CL intensity.

Chapter 8 reports on several new applications of the metal nanostructures and experimental techniques that were studied in this thesis. Based on the plasmonic whispering gallery cavities of chapters 4–6 we present a sensitive ultra-small localized surface plasmon sensor that exploits the nanoscale field confinement for high-density integrated sensing. Next, we show that the same cavity could serve as the first surface plasmon ring laser with high potential for device integration. Inspired by FIB-fabrication, we present a template stripping technique for the large-scale replication of ion-milled structures and an in-situ monitor of ionoluminescence and cathodoluminescence that enables better control over the FIB milling process. Finally, we present a novel design for a single-photon source for use in quantum optical communication that is inspired by a combination of FIB milling and electron beam excitation of plasmonic nanostructures.

Samenvatting

Licht kan langs een metaaloppervlak geleid worden in de vorm van oppervlakteplasmonpolaritonen, kortweg plasmonen. Plasmonen zijn oscillaties in de dichtheid van de vrije elektronen in het metaal die zich als golven voortplanten over het oppervlak. Deze golven worden gekarakteriseerd door een bijzondere dispersie die samengaat met korte golflengten en het samenpersen van licht. Deze eigenschappen stellen ons in staat om met plasmonen licht te manipuleren op de nanoschaal.

Plasmonen die in drie dimensies worden opgesloten geven aanleiding tot staande golven, oftewel resonanties. Plasmonische resonatoren worden vaak nanoantennes genoemd omdat deze metaalstructuren licht uit het verre veld kunnen koppelen aan een zeer klein lokaal volume. Deze koppeling leidt mogelijk tot interessante toepassingen waarbij de antenne zowel als zender als als ontvanger gebruikt kan worden. Deze toepassingen vereisen een hoge mate van controle over de resonante plasmonische velden op zeer kleine lengteschaal.

In dit proefschrift brengen we de staande golven van licht op plasmonische nanoantennes in beeld en we bepalen hiermee de dispersie van het licht. We sturen daarnaast de dispersie en de opsluiting verder door het kiezen van geschikte metaalstructuren.

Voor de fabricage van nanostructuren hebben we gebruik gemaakt van een gefocusseerde ionenbundel (FIB). We demonstreren dat monokristallijne metalen een uitermate geschikt substraat vormen voor het nauwkeurig definiëren van de geometrie waarin plasmonen worden opgesloten.

De microscopische eigenschappen van de resonante plasmonvelden bepalen we met een nieuwe techniek die we in dit proefschrift presenteren: plaats-, hoek- en polarisatieopgeloste kathodeluminescentiespectroscopie. Deze techniek gebruikt een gefocusseerde elektronenbundel om plasmonische nanoantennes aan te slaan; de vervolgens uitgezonden kathodeluminescentie (CL) bevat spectrale kenmerken van de resonanties op de nanoschaal. Hiermee kunnen de eigenschappen van de antenneresonanties worden gemeten met een oplossend vermogen ver beneden de golflengte van licht.

In hoofdstuk 2 laten we experimentele resultaten zien van polykristallijne gouden nanodraden met een lengte van 500 tot 1200 nm. Plaatsopgeloste CL

vertoont knopen-en-buiken-patronen langs de as van de nanodraden. Dit patroon wordt veroorzaakt door staande plasmongolven; we vinden verscheidene van zulke resonanties met een verschillend aantal knopen. Uit de metingen bepalen we rechtstreeks de golflengten van de plasmonen, waaruit de dispersierelatie van nanodraad-plasmonen kan worden afgeleid.

In hoofdstuk 3 introduceren we een nanoantenne die bestaat uit een langwerpige verhoging (lengte: 590 nm) op een monokristallijn goudoppervlak, gefabriceerd met FIB. De verhoging heeft een glad oppervlak en laat een fabricagenauwkeurigheid zien die met polykristallijne materialen niet behaald kan worden. Plasmonen op de verhoging worden aangeslagen en ruimtelijk opgelost met CL-spectroscopie. Met een factoranalysetechniek rafelen we de data uiteen tot een beperkt aantal plasmonresonanties, waarmee we aantonen dat plasmonen op de verhoging opgesloten zitten. Berekeningen van de veldverdeling met de grenselementenmethode (BEM) laten zien dat er inderdaad een plasmon aan de structuur gebonden is; het plasmonveld strekt zich lateraal over minder dan 100 nm uit.

In hoofdstuk 4 worden de verschillende resonanties van een plasmonringresonator uiteengerafeld. De resonatoren, bestaande uit een ronde groef, zijn in een monokristallijn goudoppervlak geëtst met FIB. De resonatoren zenden een CL-spectrum uit met een aantal afzonderlijke pieken die sterk afhangen van de resonatorgeometrie. Vergelijking van de metingen met BEM-berekeningen laat een uitstekende overeenkomst zien tussen theorie en experiment. Uit de berekeningen kan worden opgemaakt dat de verschillende resonanties toebehoren aan verschillende azimuthale en radiële ordes: de resonanties worden veroorzaakt door rondlopende plasmonen die aan de groef gebonden zijn. In de kleinste resonator past slechts één golflengte in de omtrek.

Hoofdstuk 5 bevat een theoretische studie van deze plasmonische ringresonanties, die laat zien dat kleine ringresonatoren spontane emissie kunnen vergroten over een brede spectrale band. We berekenen de kwaliteitsfactor Q en het mode volume V voor resonatoren met verschillende groefvormen en straal. De waarde van Q varieert tussen de 10 en 50 afhankelijk van de geometrie; mode volumes lopen een factor 30 uiteen. Het kleinste mode volume $0.00073\,\lambda_0^3$ vonden we voor een ring gebaseerd op een 100 nm diepe, 10 nm brede groef. Afhankelijk van de precieze geometrie bereikt de Purcell factor waarden van >2000 bij energieën van 1.0–1.8 eV. Voor een gegeven resonator treedt de verhoogde spontane emissie op over een breedbandig (50–100 meV) spectraal bereik.

Hoofdstuk 6 laat zien hoe de ringresonator zich gedraagt als een antenne die zowel ontvangt als zendt. We doen dit met behulp van vier experimentele technieken. We laten zien dat het aanslaan van de antenne vanuit het verre veld slechts die resonanties aanslaat die een dipoolmoment in het substraatvlak hebben. Het spectrum van het verstrooide licht heeft een Fano-piek rond de golflengte van deze dipoolresonantie. Wanneer de antenne wordt aangeslagen door een elektronenbundel, kunnen ook hogere-orde resonanties aangeslagen worden, afhankelijk van waar de bundel op de antenne gepositioneerd wordt. De bijbehorende hoekver-

deling van de antenne-emissie meten we in het verre veld. Fluorescentiemetingen laten zien dat het emissiespectrum van moleculen in de groef sterk wordt beïnvloed door koppeling aan de ringresonanties. Tot slot zien we dat de hoge elektrische-veldsterkte in antennes die vanuit het verre veld worden aangeslagen aanleiding geeft tot fotoelektron-emissie. De afbeelding van deze elektronen vormt een alternatieve manier om de lokale veldverdeling te bepalen.

In hoofstuk 7 kijken we naar plasmonresonatoren die zijn gebaseerd op een multilaags structuur van zilver, SiO_x en weer zilver, gefabriceerd met onder andere FIB. In deze golfgeleiders kunnen we door de dispersie te controleren een effectieve brekingsindex van 0 bereiken. Plasmonen in de golfgeleiders kunnen worden aangeslagen door een elektronenbundel die door de lagenstructuur heen priemt. Plaatsopgeloste CL-metingen geven ons de profielen van de resonanties, waaruit we de dispersierelatie van plasmonen bepalen. Dit doen we voor golfgeleiders met verschillende breedte. Op de golflengte waarbij een plasmon wordt afgekapt als gevolg van de beperkte breedte, oscilleert de hele golfgeleider in fase ($n = 0$). We meten voor deze golfgeleiders het emissiepatroon van een lijndipool; een verhoogde CL-intensiteit duidt daarnaast op een verhoogde toestandsdichtheid.

Hoofdstuk 8 beschrijft een aantal nieuwe toepassingen van de metalen nanostructuren en experimentele technieken die zijn gebruikt in dit proefschrift. Op basis van de ringresonatoren uit hoofdstukken 4–6 presenteren we een gevoelige ultra-kleine plasmonsensor die de samenpersing van licht gebruikt om zeer dicht opeengepakte sensoren mogelijk te maken. Vervolgens laten we zien dat dezelfde resonator zou kunnen dienen als de eerste plasmonische ringlaser. Geïnspireerd op FIB-fabricage laten we zien dat FIB gebruikt kan worden voor het maken van een mal voor het repliceren van metaalstructuren. Daarnaast laten we zien dat de detectie van licht dat geproduceerd wordt tijdens FIB-etsen kan fungeren als extra monitor tijdens fabricage. Tot slot presenteren we een nieuw ontwerp voor een bron van enkele fotonen die gebruikt kan worden in quantum-optische communicatie, geïnspireerd op een combinatie van FIB en de excitatie van plasmonstructuren met een elektronenbundel.

List of publications

This thesis is based on the following publications:

- *Direct observation of plasmonic modes in Au nanowires using high-resolution cathodoluminescence spectroscopy*, E. J. R. Vesseur, R. de Waele, M. Kuttge, and A. Polman, Nano Lett. **7**, 2843 (2007). **(Chapter 2)**
- *Surface plasmon polariton modes in a single-crystal Au nanoresonator fabricated using focused-ion-beam milling*, E. J. R. Vesseur, R. de Waele, H. J. Lezec, H. A. Atwater, F. J. García de Abajo, and A. Polman, Appl. Phys. Lett. **92**, 83110 (2008). **(Chapter 3)**
- *Modal decomposition of surface-plasmon whispering gallery resonators*, E. J. R. Vesseur, F. J. García de Abajo, and A. Polman, Nano Lett. **9**, 3147 (2009). **(Chapter 4)**
- *Broadband Purcell enhancement in plasmonic ring cavities*, E. J. R. Vesseur, F. J. García de Abajo, and A. Polman, Phys. Rev. B **82**, 165419 (2010). **(Chapter 5)**
- *Plasmonic whispering gallery cavities as optical nanoantennas*, E. J. R. Vesseur, and A. Polman, in preparation. **(Chapter 6)**
- *A metal-insulator-metal waveguide at cutoff as effective $n = 0$ material*, E. J. R. Vesseur, T. Coenen, H. Caglayan, N. Engheta and A. Polman, in preparation. **(Chapter 7)**

Patent application:

- *Single-photon source*, A. Polman, E.J.R. Vesseur, T. Coenen, F.J. García de Abajo, European Patent Application 10186046.8 (2010) **(Section 8.6)**

Other publications by the author:

- *Plasmonic modes in annular nanoresonators studied by spectrally resolved cathodoluminescence*, C. E. Hofmann, E. J. R. Vesseur, L. A. Sweatlock, H. J. Lezec, F. J. García de Abajo, A. Polman, and H. A. Atwater, Nano Lett. **7**, 3612 (2007).

- *Loss mechanisms of surface plasmon polaritons on gold probed by cathodoluminescence imaging spectroscopy*, M. Kuttge, E. J. R. Vesseur, J. Verhoeven, H. J. Lezec, H. A. Atwater, and A. Polman, Appl. Phys. Lett. **93**, 113110 (2008).

- *Local density of states, spectrum, and far- eld interference of surface plasmon polaritons probed by cathodoluminescence*, M. Kuttge, E. J. R. Vesseur, A. F. Koenderink, H. J. Lezec, H. A. Atwater, F. J. García de Abajo, and A. Polman, Phys. Rev. B **79**, 113405 (2009).

- *Fabry-Pérot resonators for surface plasmon polaritons probed by cathodoluminescence*, M. Kuttge, E. J. R. Vesseur, and A. Polman, Appl. Phys. Lett. **94**, 183104 (2009).

- *Degenerate dark and bright resonances in ultra-thin plasmonic strip antennas*, E. S. Barnard, T. Coenen, E. J. R. Vesseur, R. A. Pala, A. Polman, and M. L. Brongersma, in preparation.

- *Directional emission from plasmonic Yagi-Uda antennas probed by angle-resolved cathodoluminescence spectroscopy*, T. Coenen, E. J. R. Vesseur, A. Polman, and A. F. Koenderink, in preparation.

Dankwoord

Velen hebben mij geholpen om dit proefschrift te maken tot wat het is.

Allereerst wil ik mijn promotor Albert Polman bedanken. Albert, ik heb het als een voorrecht ervaren om met je te kunnen werken. Ik denk dat het zeldzaam is om in de natuurkunde iemand te vinden met zoveel sociaal gevoel en zo n groot vermogen om de juiste woorden te zeggen. Promoveren in jouw groep was een geweldige en zeer leerzame ervaring door je voortdurende streven naar impact en je positieve instelling. Dankje voor het creëren van zoveel kansen om mijn werk te presenteren.

Een vliegende start op Amolf had ik mede dankzij René de Waele. René, ik vond het mooi om te werken met iemand die over alles zo n sterke mening had als jij. We kregen het experiment aan de praat waar we tot op de dag van vandaag de vruchten van plukken. Aan dit experiment heb ik daarna nog heel prettig samengewerkt met Martin Kuttge en later met Toon Coenen. Toon, je versterking op de CL-opstelling was zeer welkom en zorgde voor grote vooruitgang; resultaten volgden al snel getuige een aantal figuren in dit proefschrift en heel mooie papers die je in de planning hebt staan. Steeds van onschatbare waarde bij al deze experimenten was Hans Zeijlemaker. Hans, ik heb met heel veel plezier met je samengewerkt. Ik vond het geweldig om de fascinatie voor de experimentele resultaten en natuurverschijnselen in het algemeen met je te delen.

Being once the youngest and now the oldest group member, I enjoyed working with a few generations of Ph.D. students, postdocs and master students. A big part of what I learned is thanks to you! Hans Mertens, Femius Koenderink, Sébastien Bidault, Rob van Loon, Kylie Catchpole, Marc Verschuuren, Erwin Kroekenstoel, Maarten Hebbink, Claire van Lare, Pierpaolo Spinelli, Rutger Thijssen, James Parsons, Ruben Maas, Jorik van de Groep, Hinke Schokker and David Schoen, thank you all for a very nice time. Ewold Verhagen and Robb Walters, you guys were great co-boat owners but thanks also for asking the right scientific questions and sharing your expertise.

One reason I wanted to do a Ph.D. at Amolf was the close collaboration within the nanophotonics department. The weekly colloquium, supposed to be a conference training, was ten times tougher than any conference I have been to, but

a great opportunity to learn and maybe the best way to receive feedback that was honest and to-the-point. Thanks for those who nourish this culture and constantly try to keep everyone involved. Within the department, many were my office mates, companions at conferences or even housemates. I would like to acknowledge Jaime Gómez Rivas and Ad Lagendijk for letting me use their equipment and hosting me in their groups. Yichen Zhang, thank you for all your help setting up the measurements. Ramy El-Dardiry, hartelijk dank voor je hulp bij de metingen maar vooral voor het zijn van een geweldige kamergenoot. The final months of my life at Amolf were well spent in office 2.51, also with Yichen, Paolo Scalia, Grzegorz Grzela and a short but memorable appearance of James Parsons. Not only was this a good place to finish a thesis, we also had a few good laughs. Thanks also to my fellow PV members for a lot of fun while organizing Amolf events.

Voor een (jonge) onderzoeker is Amolf echt een gespreid bedje. Dat is voor een heel groot gedeelte te danken aan mensen in de ondersteuning die niet alleen vaardig en kundig zijn, maar ook meedenken op een manier die mij na meer dan vier jaar nog steeds kan verrassen. Zonder uitputtend te zijn wil ik in ieder geval Chris Rétif, Iliya Cerjak, Wim Brouwer en Gijs Vollenbroek bedanken, maar op alle afdelingen zitten mensen die zich er hard voor inzetten om Amolf de geoliede machine te laten zijn die het is.

Outside of Amolf I owe great thanks to Harry Atwater and his group, who made the summer of 2006 an unforgettable experience by kindly hosting me at Caltech. Thank you Henri Lezec, Carrie Hofmann and Luke Sweatlock for helping me start up and making this project a success. A special collaboration was with Javier García de Abajo. Javier, thank you for teaching us so much about CL, helping us understand the experimental results, introducing us to your code and providing assistance over Skype. You are a great person to work with. The almost 24/7 collaboration with Ed Barnard from Mark Brongersma s group was intense, very enjoyable and a great success. Many thanks to Martin Aeschlimann and his group for our collaboration that has lead to some of the newest results in this thesis. Nader Engheta and Humeyra Caglayan, thank you so much for the collaboration that resulted in the last experimental chapter that for me felt as the icing on the cake. Ik zou graag de mensen bij het LISA-cluster bedanken voor de snelle en professionele hulp bij het doen van berekeningen.

Van buiten de wetenschap kon ik rekenen op ondersteuning van altijd belangstellende vrienden, die ik niet allemaal op kan noemen. De regelmatige etentjes in Utrecht met Licht 2001, niet voor niets leverancier van de paranimfen, zal ik nooit vergeten. De DenkTank was een verfrissend intermezzo tussen het promoveren door en staat nog steeds garant voor koffie op zaterdag en mooie activiteiten. De Ceintuurbaan was een heel aangename thuishaven in de laatste maanden dat ik aan mijn promotie heb gewerkt.

Tot slot wil ik mijn ouders en zusjes bedanken. Door een vanzelfsprekende interesse voor hoe dingen werken, en door mij er vriendelijk aan te herinneren dat ik vroeger uitvinder wilde worden, hebben jullie wellicht de allergrootste rol gespeeld in het totstandkomen van dit proefschrift.

About the author

Ernst Jan Ruben Vesseur was born in Rotterdam, The Netherlands, on December 11, 1981. After obtaining his high school diploma at the Gymnasium Celeanum in Zwolle in 1999, he studied experimental physics at Utrecht University. He obtained his master's degree in 2007 with a project performed at the FOM Institute for Atomic and Molecular Physics (AMOLF) in Amsterdam, supervised by prof. dr. Albert Polman. Part of this project was carried out in the group of prof. Harry Atwater at the California Institute of Technology in Pasadena, CA. He continued his research at AMOLF as a Ph.D. student, the results of which constitute this thesis.

Besides his scientific work, Ernst Jan was active in other fields. In 2001 he rowed in the freshman lightweight crew of student boat club Orca and later spent a year as Orca's secretaris. In 2003 he founded the IT company INFI b.v. together with three co-founders. During his Ph.D., he took part in De Nationale Denktank, a three-month fulltime project with a multidisciplinary team of 21 students that dealt with stimulation of energy conservation by Dutch consumers.

In his free time, Ernst Jan enjoys cycling, skiing and hang gliding.

The work described in this thesis was performed at the FOM Institute AMOLF, Science Park 104, 1098 XG Amsterdam, The Netherlands.